

# Molecular Engineering of Electrode Surfaces for Electrocatalysis

Présentée le 15 octobre 2020

à la Faculté des sciences de base  
Laboratoire de science à l'échelle nanométrique  
Programme doctoral en science et génie des matériaux

pour l'obtention du grade de Docteur ès Sciences

par

**Patrick Eduard ALEXA**

Acceptée sur proposition du jury

Prof. A. Fontcuberta i Morral, présidente du jury  
Prof. K. Kern, directeur de thèse  
Dr S. Stepanow, rapporteur  
Prof. K. Tschulik, rapporteuse  
Prof. A. Radenovic, rapporteuse



Success is not defined by results,  
but rather by your perseverance to pick yourself up again.

— P. Alexa





# List of Publications

During the course of this Ph.D., the following articles were published:

- [1] D. Hötger, P. Abufager, C. Morchutt, P. Alexa, D. Grumelli, J. Dreiser, S. Stepanow, P. Gambardella, H. F. Busnengo, M. Etzkorn, R. Gutzler, and K. Klaus, “On-surface transmetalation of metalloporphyrins,” *Nanoscale*, vol. 10, no. 45, pp. 21116–21122, 2018
- [2] P. Alexa, C. Oligschleger, P. Gröger, C. Morchutt, V. Vyas, B. V. Lotsch, J. C. Schön, R. Gutzler, and K. Kern, “Short-range structural correlations in amorphous 2D polymers,” *ChemPhysChem*, vol. 20, no. 18, pp. 2340–2347, 2019
- [3] P. Alexa, J. M. Lombardi, P. Abufager, H. F. Busnengo, D. Grumelli, V. S. Vyas, F. Haase, B. V. Lotsch, R. Gutzler, and K. Kern, “Enhancing hydrogen evolution activity of Au (111) in alkaline media through molecular engineering of a 2D polymer,” *Angewandte Chemie International Edition*, vol. 59, no. 22, pp. 8411–8415, 2020



# Abstract

Electrocatalysts play an important part on the route towards environmental friendly energy sources. They support modern technologies like fuel cells in order to move further away from the utilization of fossil fuels and the resulting CO<sub>2</sub> emission into our atmosphere. The main principle of such energy conversion technologies is to store chemical energy within chemical bonds and to release it as electric energy to fulfill the energy demand of today's society. However, energy conversion chemistry in such technologies requires catalysts in order to be effective by providing an alternative reaction pathway that lowers activation energies and maximizes the energy output. Providing suitable catalyst surfaces requires a fundamental knowledge of the interaction of reactants and reaction intermediates with the catalyst surfaces. This concern is addressed in this thesis by fabricating specifically tailored molecular components on metal surfaces, which act as organic/inorganic hybrid electrodes for various energy conversion reactions in electrocatalysis.

Characterizing the electrode surface is crucial in order to identify active sites of the catalyst. The molecular structure is investigated by surface sensitive techniques, such as scanning tunneling microscopy (STM) and X-ray photoelectron spectroscopy (XPS) in combination with a home-build transfer system, which enables electrode fabrication in ultra-high vacuum (UHV) and electrocatalytic experiments in a liquid environment.

A detailed characterization of organic polymer components on electrode surfaces is obtained by combining experimental data with molecular dynamic (MD) simulations. The morphology of polymer networks can be successfully mimicked and depending on the chemical composition and the structure, spatial correlations on short length scales are reported.

Hybrid electrodes with organic polymer co-catalysts reveal an increased catalytic activity for the hydrogen evolution reaction (HER) by providing suitable docking sites that act as catalytic active sites. Reactants and reaction intermediates are stabilized via hydrogen bonding, which results in a higher catalytic turnover. The specific designed structure of the organic co-catalyst helps to identify a fraction of the reaction mechanism and highlights the importance of molecular components in electrocatalysis.

The utilization of organic units on electrocatalysts provides also an excellent opportunity in order to use single metal atoms as catalysts. Cobalt atoms within structurally different macro cycles are tailored and tested as electrocatalysts for the oxygen reduction reaction (ORR). Engineering large  $\pi$ -systems has no significant impact on the ORR activity, while the distance between active sites (cobalt atoms) and the underlying electrode are crucial for enhancing the catalytic activity.

## Abstract

---

A significant factor in using molecular components in electrocatalysis is the stability of the organics. Using electrografting allows to design organic/inorganic hybrid electrodes with covalent bonds between the molecular component and the metal substrate. Attaching empty porphyrin molecules to substrates introduces a powerful technique in molecular engineering, since empty porphyrin cycles can be metallized with various metal centers that can act as electrocatalysts for different electrochemical reactions.

In summary, this thesis provides multiple engineering aspects, which are useful in designing molecular components on metal electrodes for energy conversion chemistry. Such hybrid catalyst surfaces are capable of improving the catalytic activity and allow to study the mechanism of catalytic reactions. Implementing organic components provides new routes for tailoring novel materials, which deliver new insight into the complex field of electrocatalysis.

**Keywords:** electrocatalysis, scanning tunneling microscopy, hydrogen evolution reaction, oxygen reduction reaction, 2D polymer, amorphous.

# Kurzfassung

Elektrokatalysatoren spielen eine wichtige Rolle auf dem Weg zu umweltfreundlichen Energiequellen. Sie unterstützen moderne Technologien wie Brennstoffzellen, um sich weiter von der Nutzung fossiler Brennstoffe und der daraus resultierenden CO<sub>2</sub>-Emission in unsere Atmosphäre zu entfernen. Das Prinzip dieser Technologien beruht auf Energieumwandlung. Dabei wird Energie in chemischen Bindungen gespeichert und anschließend in der Form von elektrischer Energie freigegeben. Auf diese Weise kann der Energiebedarf der heutigen Gesellschaft gedeckt werden. Um die Energieumwandlung innerhalb dieser Technologien effizient zu gestalten sind Katalysatoren erforderlich. Diese ermöglichen einen alternativen Reaktionsweg durch Senken der Aktivierungsenergie und Maximierung des Energiegewinns. Die Herstellung geeigneter Katalysatoroberflächen erfordert grundlegende Kenntnisse über die Wechselwirkung von Edukten und Reaktionszwischenprodukten mit der Oberfläche des Katalysators. Diese Thematik wird im Rahmen dieser Dissertation durch die Herstellung spezifisch entworfener molekularer Komponenten auf Metalloberflächen behandelt. Diese fungieren als organisch/anorganische Hybridelektroden und werden für verschiedene elektrochemische Reaktionen eingesetzt, die von hoher Bedeutung für die Energieumwandlung sind.

Die Charakterisierung der Elektrodenoberfläche ist entscheidend, um die aktiven Zentren des Katalysators zu identifizieren. Die Molekülstruktur wird durch oberflächensensitive Techniken wie der Rastertunnelmikroskopie (STM) und der Röntgenphotoelektronenspektroskopie (XPS) untersucht. Diese werden mit einem selbstgebauten Transfersystem kombiniert, welches die Herstellung der Elektroden im Ultrahochvakuum (UHV) sowie die Durchführung elektrokatalytischer Experimente in einer flüssigen Umgebung ermöglicht.

Die Kombination experimenteller Daten mit molekulardynamischen (MD) Simulationen ermöglicht eine detaillierte Charakterisierung organischer Polymerstrukturen auf Elektrodenoberflächen. Die Struktur von Polymernetzwerken kann erfolgreich durch theoretische Berechnungen nachgeahmt werden. Abhängig von der chemischen Zusammensetzung und strukturellen Eigenschaften treten räumliche Korrelationen auf kurzen Längenskalen auf.

Hybridelektroden mit Co-Katalysatoren aus organischen Polymeren zeigen eine erhöhte katalytische Aktivität für die Wasserstoffentwicklung, indem sie geeignete Andockstellen bereitstellen, die als katalytisch aktive Zentren wirken. Edukte und Reaktionszwischenprodukte werden über Wasserstoffbrücken stabilisiert, was zu einem höheren katalytischen Umsatz führt. Die spezifisch entworfene Struktur des organischen Co-Katalysators hilft bei der Untersuchung des Reaktionsmechanismus und unterstreicht die Bedeutung molekularer Komponenten bei

der Elektrokatalyse.

Die Verwendung organischer Einheiten innerhalb der Elektrokatalyse bietet auch eine hervorragende Möglichkeit, einzelne Metallatome als Katalysatoren zu verwenden. Kobaltatome in strukturell unterschiedlichen organischen Makrozyklen werden als Elektrokatalysatoren für die Sauerstoffreduktionsreaktion (ORR) getestet. Die Entwicklung großer  $\pi$ -Systeme hat keinen signifikanten Einfluss auf die ORR-Aktivität, während der Abstand zwischen aktiven Zentren (Kobaltatomen) und der darunter liegenden Elektrode für die Verbesserung der katalytischen Aktivität entscheidend ist.

Ein bedeutender Faktor bei der Verwendung von molekularen Komponenten in der Elektrokatalyse ist die Stabilität der organischen Stoffe. Die Verwendung von Elektroreduktion ermöglicht das Design organisch/anorganischer Hybridelektroden mit kovalenter Bindung zwischen der molekularen Komponente und dem Metallsubstrat. Derartige Verbindungen können leere Porphyrinmoleküle an Substrate binden und bieten eine leistungsstarke Herstellungsmethode innerhalb der Molekulartechnik. Die leeren Porphyrinmoleküle können mit diversen Metallzentren gefüllt werden und als Elektrokatalysatoren für verschiedene elektrochemische Reaktionen eingesetzt werden.

Zusammenfassend bietet diese Dissertation mehrere Ansätze, die beim Entwurf molekularer Komponenten auf Metallelektroden für die Elektrokatalyse nützlich sind. Oberflächen solcher Hybridkatalysatoren können die katalytische Aktivität verbessern und ermöglichen die Untersuchung von katalytischen Reaktionsmechanismen. Die Beteiligung organischer Komponenten ermöglicht die Entwicklung neuartiger Materialien, die bisher unzugängliche Einblicke in das komplexe Gebiet der Elektrokatalyse gestatten.

**Stichwörter:** Elektrokatalyse, Rastertunnelmikroskopie, Wasserstoffentwicklung, Sauerstoffreduktion, 2D Polymer, amorph.

# Résumé

Les électrocatalyseurs jouent un rôle important sur la voie vers des sources d'énergie respectueuses de l'environnement. Ils soutiennent les technologies modernes comme les piles à combustible afin de s'éloigner davantage de l'utilisation de combustibles fossiles et par conséquent de l'émission de  $\text{CO}_2$  qui en résulte dans notre atmosphère. Le principe fondamental de ces technologies de conversion d'énergie est de stocker l'énergie chimique dans des liaisons chimiques et de la libérer sous forme d'énergie électrique pour répondre à la demande énergétique de la société d'aujourd'hui. Cependant, la chimie de conversion d'énergie dans de telles technologies nécessite des catalyseurs pour être efficace en fournissant une voie de réaction alternative qui réduit les énergies d'activation et maximise le résultat de la production d'énergie.

Fournir des surfaces de catalyseur appropriées nécessite une connaissance fondamentale de l'interaction des réactifs et des intermédiaires de réaction avec les surfaces de catalyseur. Cette problématique est abordée dans cette thèse en fabriquant des composants moléculaires spécifiquement adaptés sur des surfaces métalliques, qui agissent comme des électrodes hybrides organiques/inorganiques pour diverses réactions de conversion d'énergie en électrocatalyse. La caractérisation de la surface de l'électrode est cruciale pour identifier les sites actifs du catalyseur. La structure moléculaire est étudiée par des techniques sensibles à la surface, telles que la microscopie scanner à effet tunnel (STM) et la spectroscopie photoélectron à rayons X (XPS) en combinaison avec un système de transfert maison, qui permet la fabrication d'électrodes dans un vide ultra-poussé (UHV) ainsi que des expérimentations électrocatalytiques dans un environnement liquide.

Une caractérisation détaillée des composants polymères organiques sur les surfaces d'électrodes est obtenue en combinant des données expérimentales avec des simulations de dynamique moléculaire (MD). La morphologie des réseaux de polymères peut être imitée avec succès et en fonction de la composition chimique et de la structure, des corrélations spatiales sur des échelles de longueur courte sont signalées.

Des électrodes hybrides avec des co-catalyseurs polymères organiques révèlent une activité catalytique accrue pour la réaction de dégagement d'hydrogène (HER) en fournissant des sites d'amarrage appropriés agissant comme des sites catalytiques actifs. Les réactifs et les réactions intermédiaires sont stabilisés par liaison hydrogène, ce qui entraîne un « turnover » catalytique plus élevé. La structure spécifiquement conçue du co-catalyseur organique aide à identifier une fraction du mécanisme de réaction et met en évidence l'importance des composants moléculaires dans l'électrocatalyse.

## Résumé

---

L'utilisation d'unités organiques sur des électro-catalyseurs fournit également une excellente opportunité pour utiliser des atomes métalliques uniques comme catalyseurs. Les atomes de cobalt au sein de macro-cycles structurellement différents sont conçus et testés comme électrocatalyseurs pour la réaction de réduction de l'oxygène (ORR). L'ingénierie de grands  $\pi$ -systèmes n'a pas d'impact significatif sur l'activité ORR, tandis que la distance entre les sites actifs (atomes de cobalt) et l'électrode sous-jacente est cruciale pour améliorer l'activité catalytique.

Un facteur important dans l'utilisation de composants moléculaires en électrocatalyse est la stabilité des matières organiques. L'utilisation de l'électrogreffage permet de concevoir des électrodes hybrides organiques / inorganiques avec des liaisons covalentes entre le composant moléculaire et le substrat métallique. La fixation de molécules de porphyrine vides à des substrats instaure une technique puissante en génie moléculaire, car les cycles de porphyrine vides peuvent être métallisés avec divers centres métalliques agissant comme électrocatalyseurs pour différentes réactions électrochimiques.

En résumé, cette thèse fournit de multiples aspects d'ingénierie, qui sont utiles dans la conception de composants moléculaires sur des électrodes métalliques pour la chimie de conversion d'énergie. De telles surfaces de catalyseurs hybrides sont capables d'améliorer l'activité catalytique et permettent d'étudier le mécanisme des réactions catalytiques. La mise en œuvre de composants organiques offre de nouvelles voies pour personnaliser de nouveaux matériaux, qui offrent de nouvelles perspectives dans le domaine complexe de l'électrocatalyse.

**Mots clés :** électrocatalyse, microscopie à effet tunnel, réaction de l'évolution d'hydrogène, réaction de réduction d'oxygène, polymère 2D, amorphe.



# Contents

<b>Abstract (English/Deutsch/Français)</b>	<b>iii</b>
<b>List of Figures</b>	<b>xi</b>
<b>List of Tables</b>	<b>xiii</b>
<b>Introduction</b>	<b>1</b>
<b>1 Methods</b>	<b>5</b>
1.1 Fundamentals in Electrochemistry and Electrocatalysis . . . . .	6
1.1.1 The Electrochemical Cell . . . . .	6
1.1.2 The Double Layer Model . . . . .	7
1.1.3 Electrode Reactions . . . . .	9
1.1.4 Important Electrochemical Reactions - HER and ORR . . . . .	12
1.1.5 Correlation between Binding Energy and Activity - The Volcano Plot . . . . .	14
1.2 UHV-Methods . . . . .	15
1.2.1 Scanning Tunneling Microscopy . . . . .	15
1.2.2 X-ray Photoelectron Spectroscopy . . . . .	20
1.3 Combination of Vacuum and Electrocatalysis . . . . .	22
1.3.1 Experimental Apparatus . . . . .	22
1.3.2 Transfer into the Electrochemical Cell . . . . .	23
1.3.3 Sample Preparation . . . . .	25
1.3.4 Electrochemical Experiments . . . . .	26
<b>2 Structural Short-Range Correlations in Organic Polymer Networks</b>	<b>27</b>
2.1 Experimental and Theoretical Methods . . . . .	28
2.2 Results on the Catalyst Structure . . . . .	30
2.2.1 Experimental Results . . . . .	31
2.2.2 Theoretical Results . . . . .	33
2.3 Discussion on Structural Short-Range Correlations . . . . .	36
2.4 Conclusion . . . . .	41
<b>3 Enhancing HER through Molecular Engineering</b>	<b>43</b>
3.1 Preparation of the Electrode Surfaces . . . . .	44
3.2 HER with Hybrid Electrodes . . . . .	45

## Contents

---

3.3	Long-term Stability of Hybrid Electrocatalysts . . . . .	52
3.4	HER Mechanism on Hybrid Electrodes . . . . .	53
3.4.1	Water Adsorption on Hybrid Catalysts . . . . .	54
3.4.2	Hydrogen Abstraction of Water Molecules on Hybrid Catalysts . . . . .	55
3.4.3	Correlation between Electrochemical Activity and Binding Energy . . . . .	56
3.5	Quantifying the Catalytic Activity in Organic co-Catalysts . . . . .	59
3.6	Hybrid Electrodes beyond HER . . . . .	61
3.7	Conclusion . . . . .	62
<b>4</b>	<b>Performance of Phthalocyanines as ORR-Catalysts</b>	<b>65</b>
4.1	Preparation of the Electrode Surfaces . . . . .	65
4.2	Characterization by STM and XPS . . . . .	66
4.3	ORR with Hybrid Electrodes . . . . .	68
4.4	Summary . . . . .	70
<b>5</b>	<b>Improving the Stability of Metal-Organic Hybrid Catalysts</b>	<b>71</b>
5.1	Fabrication of Hybrid Electrodes by Electrografting . . . . .	72
5.2	Fabrication of Electrode Surfaces in UHV . . . . .	74
5.3	ORR with Hybrid Electrodes . . . . .	75
5.4	Future Perspective . . . . .	76
5.5	Summary . . . . .	76
<b>6</b>	<b>Conclusion</b>	<b>79</b>
<b>7</b>	<b>Outlook</b>	<b>83</b>
	<b>Acknowledgements</b>	<b>87</b>
	<b>Bibliography</b>	<b>89</b>
	<b>Curriculum Vitae</b>	<b>103</b>

# List of Figures

1.1	Schematic model of the double layer . . . . .	8
1.2	Influence of the potential relative to the equilibrium potential . . . . .	11
1.3	Influence of a catalyst on the total net current density . . . . .	11
1.4	Volcano plot . . . . .	14
1.5	Bardeen tunneling theory: One dimensional case . . . . .	17
1.6	Energy diagram of a tip-sample junction . . . . .	18
1.7	Porphyrin molecules on a gold substrate . . . . .	19
1.8	Relation between energy levels of sample and spectrometer . . . . .	21
1.9	Chemical shift of the N 1s core levels in XPS spectra . . . . .	22
1.10	Schematic overview of the applied analytic techniques . . . . .	24
1.11	Schematic illustration of the electrochemical cell . . . . .	25
2.1	Ullmann-like coupling pathway and molecular dynamics model . . . . .	28
2.2	Scheme of a $\alpha\beta\gamma$ triplet . . . . .	29
2.3	P-N <sub>0</sub> network with hexagonal and schematic $\alpha\beta\gamma$ triplet . . . . .	31
2.4	Pore size distribution in the organic polymers P-N <sub>0</sub> and P-N <sub>3</sub> . . . . .	32
2.5	Short-range order by $\alpha\beta\gamma$ triplet distribution . . . . .	33
2.6	Calculated amorphous network in variable periodic simulation cell . . . . .	34
2.7	Time evolution of ring- and $\alpha\beta\gamma$ distribution . . . . .	35
2.8	Potential energy per atom as a function of time for P-N <sub>0</sub> and P-N <sub>3</sub> . . . . .	36
2.9	Experimental and simulated histograms of the ring size distribution of P-N <sub>0</sub> and P-N <sub>3</sub> . . . . .	37
2.10	Experimental and theoretical distribution of $\alpha\beta\gamma$ triplets . . . . .	38
2.11	Top and side view of different $\alpha\beta\gamma$ triplets . . . . .	39
3.1	Overview of the fabricated 2D polymer . . . . .	44
3.2	Double-layer capacitance measurement . . . . .	45
3.3	Electrochemical active surface area . . . . .	46
3.4	Cyclic voltammograms for hybrid electrodes in 0.1 M Ar saturated NaOH solution prior to hydrogen evolution . . . . .	47
3.5	HER on hybrid electrodes in 0.1 M Ar saturated NaOH solution recorded with 0.05 V s <sup>-1</sup> . . . . .	48
3.6	Characterization of the P-N <sub>0</sub> co-catalyst by STM and XPS before and after HER .	49

## List of Figures

---

3.7	Characterization of the P–N <sub>3</sub> co-catalyst by STM and XPS before and after HER .	50
3.8	Characterization of the P–N <sub>6</sub> co-catalyst by STM and XPS before and after HER .	51
3.9	Stability measurement of the P–N <sub>3</sub> co-catalyst on Au(111) . . . . .	52
3.10	Adsorption sites on Au(111) . . . . .	54
3.11	Water adsorption site of the organic co-catalysts . . . . .	55
3.12	Hydrogen abstraction of water . . . . .	55
3.13	Energy diagram of water and hydrogen adsorption for Au(111) and investigated hybrid electrodes . . . . .	57
3.14	Quasi-volcano plot . . . . .	58
3.15	Antibonding states of water . . . . .	59
3.16	Oxygen reduction with cobalt support on hybrid electrode . . . . .	61
4.1	Schematic overview of the used Phthalocyanines . . . . .	66
4.2	STM of cobalt phthalocyanines on Au(111) . . . . .	67
4.3	XPS spectra of cobalt phthalocyanine . . . . .	68
4.4	ORR with cobalt phthalocyanine catalysts . . . . .	69
4.5	Influence of TIPS groups during electrocatalysis . . . . .	70
5.1	Porphyrin configuration on the electrode surface . . . . .	72
5.2	Dediazonation reaction . . . . .	72
5.3	Characterization of hybrid electrodes fabricated by electrografting . . . . .	73
5.4	STM image of a porphyrin decorated Au(111) surface . . . . .	74
5.5	Oxygen reduction with porphyrin decorated Au(111) electrodes . . . . .	75
5.6	Future plan for fabricating monolayers by electrografting . . . . .	76
7.1	Metal-organic polymer as catalyst for CO <sub>2</sub> reduction . . . . .	84
7.2	Electrografted hybrid electrodes for CO <sub>2</sub> reduction . . . . .	85
7.3	Comparison of conventional and flow cell set up in combination with gas chro- matography . . . . .	85

## List of Tables

1.1	Experimental details on organic molecule deposition . . . . .	26
3.1	Binding energies for water and hydrogen . . . . .	54
3.2	Apparent hydrogen binding energy of the investigated electrodes . . . . .	56
3.3	Turnover frequencies of investigated electrodes . . . . .	60



# Introduction

Climate change in combination with the closely related subject of global energy demand, are highly discussed topics in science and society. With the growing population on our planet and the resulting increase in energy consumption, the requirement for more energy sources is undeniable. Currently, the majority of our energy originates from fossil fuels such as coal, oil and gas [4]. In 2013 the global energy demand scored 18 TW, of which 80% was produced by fossil resources [4], which goes alongside with the emission of CO<sub>2</sub> on a tremendously large scale. The high CO<sub>2</sub> concentration that we have to face inside the atmosphere can be directly connected to the combustion of fossil fuels [5, 6, 7, 8], which contributes to overall global warming and natural disasters like tsunamis, hurricanes and desertification. Avoiding such catastrophes and minimizing global warming by CO<sub>2</sub> emission has a high priority in today's society. A diverse energy generation is key to reducing the emission of CO<sub>2</sub> and on the other hand satisfies the global energy demand without destroying our environment [7, 8]. As a result, a rethinking process has emerged in politics, science and technology design to create diverse and alternative energy sources by reducing the contribution of fossil fuels and implement renewable energy supply, which can be provided by solar, wind and hydroelectric power.

In this context, electrochemical reactions such as the oxygen reduction reaction (ORR) and the hydrogen evolution reaction (HER) are experiencing increased efforts to make water a viable energy feedstock. A closed-loop energy production cycle involves water splitting by electrolysis, which converts electrical energy into chemical energy in order to store it in the form of hydrogen gas. Following the energy loop within the water cycle, hydrogen is oxidized by oxygen in fuel cells and the stored chemical energy becomes available as electricity [9, 10, 11]. Oxygen reduction is also a foundation of technologies for renewable energy conversion like rechargeable metal-air batteries [12]. Such technologies become particularly appealing in the view of alternative solar energy. As photovoltaic energy production fluctuates as function of sun exposure and surplus energy needs to be stored effectively for times of low or even absent sun light. The mentioned technologies like metal-air batteries and the water-splitting reaction are prominent alternatives, since they do not depend on external factors like sun light or wind power availability.

The limiting factor in these electrochemical reactions is mostly sluggish reaction kinetics. This translates into large overpotentials, which is reflected in high required activation energies to drive the reactions. An efficient performance of electrochemical reactions like hydrogen

evolution and oxygen reduction requires the support of catalysts, which offer an alternative reaction pathway by lowering energy barriers and maximizing the energy output. The best efficiency delivers platinum for HER and ORR [13, 14, 15, 16]. However the access to platinum is very limited, which results in very high prices and makes large scale energy production that relies on platinum catalysts rather impossible. Thus, the great challenge is to create catalysts with improved performance and to reduce the implementation of expensive noble metals, in order to make environmental friendly energy sources competitive to fossil fuels.

Material science is the driving force behind developing novel materials for energy application. A promising approach is to modify the surfaces of cheap substrates with nanoparticles [17, 18, 19] or molecular components [20, 21]. Reducing the size of catalysts from nano- to subnano size and even to single-metal atoms leads to an increase of the catalytic activity [22]. This originates from the increased surface area for smaller particles, but is also due to changing electronic structure as a function of particle size. Single metal cations can be supported by an organic structure like porphyrins or phthalocyanines [23, 24]. One advantage in using these molecules is their planar structure which leads to favorable adsorption on metal surfaces and the exposure of the metal center to the reactants. As a replacement for precious metal catalysts, metallo-porphyrins have been shown to be active for a variety of different electrocatalytic reactions like oxygen reduction [25], oxygen evolution [20], or CO<sub>2</sub> reduction [26]. Another method of making single metal atoms accessible for catalysis is based on supramolecular chemistry [27]. Metal-organic coordination networks (MOCNs) can be fabricated in UHV and consist of organic ligands, which self-assemble with metal atoms to supramolecular structures. Such systems can be used as model systems in order to investigate catalytic reactions and specify the active center on the molecular or the atomic scale [28, 29].

Metal-free electrocatalysts have recently attracted much attention as a cheap and abundant alternative to catalysts based on scarce metal [30, 31]. In particular for oxygen reduction, heteroatom-doped carbon structures show high activities as catalysts. The elements nitrogen, boron, and sulfur are used to tweak the electronic structure such that interactions with reactants and intermediates become favorable for electrocatalysis [32, 33, 34, 35]. Another recent study used boron-doped graphene as effective catalyst for nitrogen reduction. The boron heteroatoms improve nitrogen adsorption and decrease energy barriers during the nitrogen reduction reaction [36]. Investigations on hydrogen evolution were successful by using covalent organic frameworks (COFs) with varying nitrogen amount as photocatalysts to promote hydrogen production from water [37]. The photocatalytic experiments were performed in the presence of platinum as co-catalyst and the generated hydrogen was measured. The COF with the highest amount of nitrogen excelled as best catalyst in this study. Decreasing the amount of nitrogen in the COF reduces the catalytic activity and less hydrogen is produced. Other studies report about increased HER activities caused by nitrogen doped graphene with encapsulated transition metal alloys [38]. The higher catalytic activity in nanoporous graphene could directly connected with nitrogen dopants, since defects within the graphene lattice was rather inactive to hydrogen evolution [39]. Hence, nitrogen has a great impact on hydrogen evolution as catalyst. These works clearly demonstrate the usefulness of covalent carbon



structures with heteroatoms for different photo- and electrocatalytic reactions.

The design of suitable electrode surfaces, which deliver useful insight into catalytic processes can only be achieved by the combination of several analytic techniques. In particular, insight at the atomic scale proves to be of high value in providing structure-property relationships. For this reason scanning tunneling microscopy (STM) was chosen to characterize electrode surfaces throughout this thesis. In the past, several STM investigations have been performed on metal surfaces decorated with organic structures, like porphyrins and phthalocyanines [40, 41, 42, 43, 44, 45, 46]. Such molecules form complex structures on metal surfaces by weak interactions like van der Waals forces, hydrogen bonding or metal complexation [47]. A promising alternative is to fabricate organic nanostructures by covalent coupling, which can be thermally induced or by using reactive precursor molecules [48, 49, 50, 51].

Decorating metal surfaces with organic components and using these devices as electrocatalysts is a promising combination of UHV and electrochemistry in order to obtain further insight into the mechanisms of catalytic reactions. In addition, UHV preparation allows to utilize X-ray photoelectron spectroscopy (XPS), which can characterize the chemical composition of electrode surfaces. Combining UHV with electrochemistry in a single experimental set-up requires an UHV-to-ambient transfer system [21], which is the foundation of the experiments performed in this thesis.

A detailed introduction to the transfer system is given in **chapter 1**, together with the fundamental concepts of electrochemistry, including the double layer model and reactions that occur at electrode surfaces. Furthermore the electrochemical reactions, which are studied in this work are presented. The chapter involves also a brief introduction to the techniques that were used in UHV throughout this thesis, which includes STM and XPS. **Chapter 2** presents the results on short-range correlations in organic components, which are analyzed statistically and with the support of molecular dynamics simulations. The focus of **chapter 3** lies on fabricated hybrid electrodes that contain of Au(111) electrodes decorated with organic polymer co-catalysts. Such designed hybrid electrodes successfully catalyze the HER and deliver insight into the mechanism on the molecular scale. **Chapter 4** presents electrocatalysis of the ORR, with metallized phthalocyanines of different structure and shows the influence by changing the distance of substrate and catalytic active center. **Chapter 5** addresses the stability and introduces design principles in order to increase the lifetime of metal organic hybrid catalysts, which can be achieved by fabricating covalent bonds between metal substrate and organic components. The thesis is summarized by a final conclusion and by presenting future perspectives in molecular engineering of electrocatalyst surfaces.



# 1 Methods

The experiments of this thesis demanded a variety of different analytic techniques: Spectroscopic and scanning probe techniques were involved as well as an electrochemical set-up. The combination of all the used techniques and the theoretical background is introduced in this chapter.

Section 1.1 introduces the fundamentals of electrochemistry and electrocatalysis by presenting common models of the solid-liquid interface, which is referred to as electrochemical double layer. In addition the section addresses the different reactions that occur at electrode surfaces, since those mechanisms have to be optimized in order to increase the activity of important electrochemical reactions like the hydrogen evolution reaction (HER) or the oxygen reduction reaction (ORR).

The electrode surfaces that are discussed throughout this thesis were fabricated in ultra-high vacuum (UHV) to guarantee clean handling of the prepared samples. Characterization techniques were scanning tunneling microscopy (STM) and X-ray photoelectron spectroscopy (XPS). STM was chosen as real space imaging technique for visualizing the surface of the fabricated electrode surface prior and after electrocatalysis. XPS was added in order to deliver insight into the chemical composition of the electrode surfaces.

Section 1.3 presents the experimental apparatus that has been used in this thesis. The combination of UHV and ambient conditions during electrochemical experiments is explained in detail. The set-up ensures that the fabricated samples are either in UHV or in an inert argon atmosphere. Additionally, the electrochemical cell is introduced that was used for the experiments together with the technical details for the sample preparation and the electrochemical experiments.

### 1.1 Fundamentals in Electrochemistry and Electrocatalysis

The first electrochemical experiments were performed by Luigi Galvani at the end of the 18<sup>th</sup> century, who accidentally created a circuit with two metal electrodes and animal soft tissue, such as nerves and muscles, which he referred to as animal electricity [52]. Alessandro Volta elaborated on this concept and built the voltaic pile, which is known as the first electrical battery [53]. The invention of Volta opened the door for a series of new electrochemical concepts: The work of Michael Faraday on electricity and electrolysis [54] is a prominent example. Other important discoveries have been found by Wilhelm Ostwald [55], who formulated the concept of catalysis, for which he was rewarded with the Noble Prize in Chemistry in 1909. The basic concept of catalysis describes the enhancement of the reaction rate by an additional substance (catalysts), which is not consumed during the reaction. The catalyst provides an alternative pathway with low activation energy for the conversion of reactants to products. Nowadays, the research field of catalysis is divided into different branches: Examples are photocatalysis, which uses the energy of light in order to promote electron transfer [56], or electrocatalysis, which was introduced by its name in 1934 by Kobosev and Monblanova [57] and is driven by an electrically induced potential difference.

In electrocatalysis the electrode usually contains the catalyst material (heterogeneous catalysis) and the mechanism is dominated by adsorption of reactants and reaction intermediates on the electrode surface. The role of the electrocatalyst is to obtain a high current density close to the equilibrium potential. This reduces the overpotential (activation energy) that is needed in order to drive an electrochemical reaction. This is realized by designing catalyst surfaces, which optimize adsorption conditions on the catalyst surface. Important criteria are the electrode material and the amount of active surface sites in contact with the electrolyte, which can be realized by increasing the surface roughness. However no matter how well a catalyst is performing, it always involves three major steps: Adsorption of the reactants on the catalyst surface, electron transfer and desorption of the products. The following sections present the fundamental concepts and processes on the catalyst surface in more detail which are based on Ref. [58, 59, 60, 61].

#### 1.1.1 The Electrochemical Cell

Catalytic experiments are performed in an electrochemical cell, which are usually equipped with three electrodes: The working electrode, the counter electrode and the reference electrode. The working electrode is usually the material that is studied by the electrochemical experiment. The main requirement is an equidistant space between the working and the counter electrode to assure a homogeneous mass transfer between both electrodes. The working electrode that has been used throughout this thesis is Au(111), since gold has a large potential window and is not affected by corrosion within the applied experimental conditions. The counter electrode provides current of equal magnitude and opposite sign to the working electrode. If an oxidation is running at the working electrode, a reduction will appear at the counter electrode

and vice versa. The counter electrode requires an easy electron transfer and the chemistry may not interfere with the reactions at the working electrode. This is in particular important for long-term experiments, because otherwise pH changes can appear and change the nature of the electrolyte solution. For that reason a platinum wire has been chosen as counter electrode for the experiments performed in this thesis. The reference electrode is introduced to an electrochemical cell to guarantee the comparability of measured data. Such electrodes need a constant potential in every experiment. This is easily achievable within a three-electrode set-up, as the potentiostat applies only small currents through the reference electrode. The used reference electrode for the experiments in this thesis is a Ag/AgCl electrode. The last important component of an electrochemical cell is the electrolyte solution. Usually it is a salt, acid or base dissolved in water, which is an adequate solvent, due to its high solubility and dielectric constant. The main function of the electrolyte is to provide electrical conductivity with a low resistance between the electrodes.

Since the electrochemical/catalytic reactions occur at the interface of working electrode and electrolyte solution, it is important to understand the basic mechanisms that occur at the solid/liquid interface. The following sections describe the interface of electrode and electrolyte solution in more detail, including the basic model of the interface and reactions that occur.

### 1.1.2 The Double Layer Model

Changing the potential at an electrode directly affects its charge and creates a potential gradient between the electrode surface and the electrolyte solution. Ions of opposite charge within the solution will migrate towards the electrode in order to compensate the charge at the electrode surface. The charged electrode with the compensating ions can be regarded as capacitor and is referred to as electrochemical double layer.

The model of the electrochemical double layer has been improved over the years in order to provide a precise description. First assumptions have been made by Helmholtz, who described the double layer as a charged electrode, which is balanced with a monolayer of ions of opposite charge. The model assumes a quite rigid layer of ions, which is closely related to the plate of a real capacitor and named inner Helmholtz plane. Since the ions are in a liquid environment, it is likely that they are solvated and absorb on the electrode surface with a complete or partial solvation shell. This moves the Helmholtz plane further away from the electrode surface and is defined as outer Helmholtz plane. The Gouy-Chapman model describes the ions within the double layer with the ability to move smoothly through the electrolyte solution instead of remaining in a fixed rigid monolayer. Both models of Helmholtz and Gouy-Chapman are extreme views and a realistic model provided by Stern combines both models: Most of the electrode charge is balance within a compact Helmholtz layer (ions with and without hydration shell) and the Gouy-Chapman diffusive layer compensates remnant charge. Figure 1.1 shows a schematic illustration of the Stern double layer model with an exemplarily positively charged electrode. The white curve represents the potential gradient as

a function of the distance to the electrode surface. To compensate the positive potential of the electrode, anions within a hydration shell adsorb on the surface and build the outer Helmholtz plane. Especially anions can adsorb specifically on the electrode without interjacent hydrated water molecules, since they are capable to form chemical bonds with metals (inner Helmholtz plane). Such phenomena are less common with cations adsorbing on an electrode with a negative applied potential. The region between the electrode surface and the outer Helmholtz plane represents the compact layer and exhibits a linear potential gradient. The ions within the diffusion layer are less rigid and can migrate smoothly through the electrolyte and the corresponding potential gradient reveals an exponential behaviour.

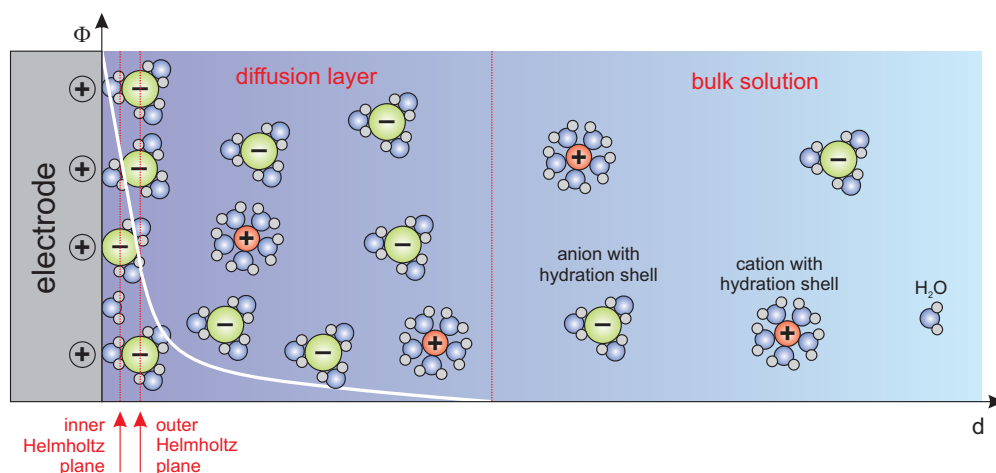


Figure 1.1 – Schematic illustration of the Stern double layer model that combines the Helmholtz and the Gouy-Chapman model: The electrochemical double layer at a positive charged electrode involves a compact layer with adsorbed anions (inner Helmholtz plane) and solvated anions (outer Helmholtz plane), followed by the diffusion layer with smoothly moving ions. The white graph represents the potential gradient within the double layer region: The electrode potential decreases linearly within the compact layer and decays exponentially until the solution potential is reached.

If the potential of the electrode is changed, the ions within the double layer will always re-organize on the surface and create a double layer charging current. Starting theoretically from an electrode surface with zero charge, a potential change  $\Delta E$  will cause the migration of ions in the solution. The created transient current has to flow through a circuit that involves the resistance of the electrolyte solution  $R_s$  and the capacitance of the double layer  $C_{DL}$ . The calculation of the double layer charging current is given by equation 1.1 and decays exponentially with time. It is important to mention that such double layer charging currents are usually not the center of electrochemical studies and occur additionally to currents that result by an electrochemical reaction

$$I = \frac{\Delta E}{R_s} \exp \left\{ -\frac{t}{R_s C_{DL}} \right\}. \quad (1.1)$$

### 1.1.3 Electrode Reactions

Electrode reactions are a class of chemical reactions that involve charge transfer at the interface of a conducting solid and a liquid solution. Usually electrons are the transferred charge within a redox reaction. Equation 1.2 represents a general electrochemical reaction with  $O$  being the oxidized species that transforms into the reduced species  $R$ . Prior to the electron transfer, the oxidized reactant is dissolved in the electrolyte solution  $O_{\text{solution}}$  and needs to be transported towards the electrode surface  $O_{\text{electrode}}$ . After adsorbing on the surface, electrons are transferred from the electrode to the reactant, reducing  $O_{\text{electrode}}$  into the product  $R_{\text{electrode}}$ , which is transported back into the bulk solution ( $R_{\text{solution}}$ ). The complete process is summarized in equation 1.2



The two processes occurring during equation 1.2 are mass transport and electron transport. Supplying sufficient reactant and the removal of product material from the electrode surface belong to the regime of mass transport, which can be distinguished in three different categories: Convection, which is the movement caused by an external mechanical field and diffusion, which is driven by concentration gradients. Migration originates by an electrostatic field and affects predominantly the ions of the electrolyte and is of minor importance. All experiments that will be presented throughout this thesis rely on diffusion as mass transport mechanism.

The most important step during an electrochemical reaction according to equation 1.2 is the transfer of electrons ( $O + ne^- \rightarrow R$ ). If the reaction is in equilibrium, the reaction rates of oxidized and reduced species ( $O$  and  $R$ ) are equal and the total net current is zero. The potential of the electrode depends on the redox couple  $O/R$ , their concentration and the corresponding formal potential  $E_e^0$ , which is the equilibrium potential under standard conditions. The equilibrium potential at different temperature  $T$  and pH values can be calculated by the Nernst equation according to equation 1.3, with  $R$  representing the gas constant and  $F$  the Faraday constant. The number of electrons involved in the redox reaction is implemented by the factor  $n$ , while  $c_O$  and  $c_R$  give the concentrations of the oxidized and reduced species in the solution at the equilibrium

$$E_e = E_e^0 + \frac{2.3RT}{nF} \log \frac{c_O}{c_R}. \quad (1.3)$$

Applying a potential shifts  $E_e$  to a new equilibrium: A potential  $E + \Delta E$  will fulfill the Nernst equation with an increasing ratio of  $c_O/c_R$  and R species will be converted into O species. A negative potential change  $E - \Delta E$  will result in the conversion of O species into R species and will reduce the  $c_O/c_R$  ratio.

However the Nernst equation and its concept presented above is only a thermodynamic explanation and accounts for equilibrium conditions. For a kinetic characterization, the reaction rate  $k$  or the current density  $j$  of the  $O \rightleftharpoons R$  conversion at any potential have to be considered. Investigations on the reaction rate show a relation in the general form of equation 1.4 for the rate of oxidation and equation 1.5 for the rate of reduction

$$k_a = k_a^0 \exp \left\{ \frac{\alpha_a n F E}{RT} \right\}, \quad (1.4)$$

$$k_c = k_c^0 \exp \left\{ -\frac{\alpha_c n F E}{RT} \right\}. \quad (1.5)$$

The factors  $\alpha_a$  and  $\alpha_c$  are the anodic and cathodic transfer coefficients and have values close to 0.5 for simple electron transfer reactions. In such cases  $\alpha_a + \alpha_c = 1$  is valid. The reaction rates  $k_a$  and  $k_c$  can be transferred into current densities by the multiplication with  $nF$  and provide the current density as a function of the electrode potential. However, the potential scale in such characterizations is arbitrary and depends strongly on the experimental set-up, especially on the choice of reference electrode.

For delivering a more precise characterization, the concept of overpotential is introduced, which is the deviation of the applied potential  $E$  from the equilibrium potential  $E_e$  for a O/R redox couple (eqn. 1.6)

$$\eta = E - E_e. \quad (1.6)$$

By using the overpotential, the scale is determined by the chemistry of the redox couple. Since the current density equals zero at the equilibrium potential, the overpotential can be seen as driving force for oxidation or reduction. By substituting the arbitrary potential  $E$  with the overpotential  $\eta$ , equation 1.7 can be derived, which is known as the Butler-Volmer equation, which has a major importance in the discussion of kinetics in electrochemistry

$$j = j_0 \left( \exp \left\{ \frac{\alpha_a n F \eta}{RT} \right\} - \exp \left\{ -\frac{(1 - \alpha_a) n F \eta}{RT} \right\} \right). \quad (1.7)$$

The Butler-Volmer equation shows how the positive/negative potential change relative to the equilibrium potential affects the partial anodic/cathodic net current density. Figure 1.2 shows the same context graphically: While the overpotential is equal to the equilibrium potential, the partial anodic and cathodic current densities are equal, which results in a total net current of zero. A positive overpotential increases the partial anodic current and decreases the partial cathodic current compared to the current at the equilibrium potential and results in a total anodic net current. The situation for a cathodic net current behaves analogously: A total cathodic net current arises due to a negative overpotential, which shifts the partial



anodic current to lower values and the partial cathodic current to higher values relative to the equilibrium potential.

Potential	Partial Current Densities	Measured Current Density
Equilibrium potential $E_o$	$j_c \leftarrow \rightarrow j_a$	zero
Positive to $E_o$	$\xrightarrow{\quad} j_a$ $j_c \leftarrow$	anodic
Negative to $E_o$	$j_c \leftarrow$ $\xrightarrow{\quad} j_a$	cathodic

Figure 1.2 – Influence of the potential relative to the equilibrium potential on the partial anodic and cathodic partial current densities and the measured total net current density (adapted with permission from Ref. [58]).

By introducing a catalyst to an electrochemical reaction the overpotential is decreased in order to drive the electron transfer for reaching a particular current density. Such a case is schematically illustrated in figure 1.3: The blue graph represents an arbitrary electrochemical reaction and the purple graph includes the support by a catalyst. Due to the definitions presented in this section, both graphs reveal no net current at  $\eta = 0$ . To reach a particular current density  $j_x$ , the reaction without an catalyst (blue graph) requires the overpotential  $\eta_1$ . By introducing a catalyst (purple graph), the necessary overpotential is decreased to  $\eta_2$  for reaching the same current density  $j_x$ .

Generally, an electrochemical reaction requires two types of processes that were introduced in this section: Mass transport and electron transfer. A special case appears, if the reactant is an adsorbed species on the electrode surface. In such cases, mass transport is not involved and cannot affect electron transfer. Assuming that a redox couple is bound at the surface and oxidation/reduction occurs, a current will be measured until reactants on the surface are oxidized/reduced. If the potential is swept faster, the current must also increase proportionally in order to keep the charge constant. The peak current density of adsorbed redox couples

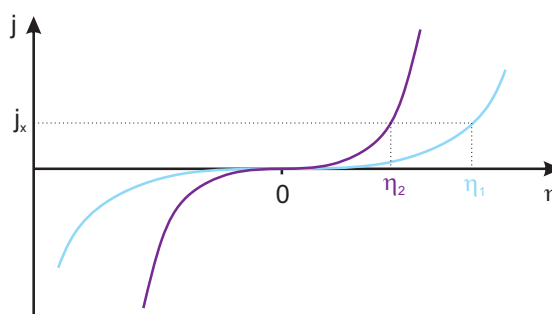


Figure 1.3 – Schematic illustration of the current density as a function of the overpotential  $\eta$ : The required overpotential of an arbitrary reaction (blue graph) is decreased by introducing a catalyst (purple graph):  $\eta_1 \rightarrow \eta_2$ .

on electrode surfaces is described by equation 1.8, with  $n$  being the number of transferred electrons in the reaction,  $F$  the Faraday constant,  $R$  the gas constant,  $T$  the temperature,  $\nu$  the scan rate and  $\Gamma$  the excess of electroactive species

$$j_p = \frac{n^2 F^2 \nu \Gamma}{4RT}. \quad (1.8)$$

In the setup of a single experiment, the factor  $\frac{n^2 F^2 \Gamma}{4RT}$  can be regarded as a constant and the peak current  $j_p$  depends only on the scan rate  $\nu$ . In consequence the relation  $j_p \propto \nu$  has to be investigated.

### 1.1.4 Important Electrochemical Reactions - HER and ORR

Nowadays fuel cells and electrolyzers are important technologies in the discussion about environmental friendly energy sources. Fuel cells combine hydrogen as fuel and oxygen as oxidant in order to provide sustainable electric power, heat and water [61]. Electrolyzers on the other hand split water into the elemental components and provide the necessary hydrogen fuel.

Hydrogen evolution is the reduction reaction of water splitting. In acidic media two hydrogen protons are combined to a hydrogen molecule by adding two electrons (eqn. 1.9), while in alkaline media water molecules act as reactants (eqn: 1.10)



Much research has been done in order to find suitable parameters to improve the HER activity. However, for many catalysts, the precise catalytically active sites are not well understood, which is particularly addressed in chapter 3 of this thesis. Today, two general reaction pathways are accepted due to hydrogen evolution. Both require a discharge reaction and form an adsorbed hydrogen atom on a metal surface, know as the *Volmer reaction* (eqn: 1.11) [62]. The abbreviation M in the following reactions represent a bonding site on the catalyst surface. Since all experiment that will be presented throughout this thesis have been performed at pH = 13, the following reactions are written in their alkaline form [63]



In the *Volmer-Tafel mechanism* protons are discharged and adsorb on the metal surface in a

## 1.1. Fundamentals in Electrochemistry and Electrocatalysis

first step according to equation 1.11. The formation of hydrogen molecules follows the *Tafel reaction* [64], which combines two hydrogen atoms that are adsorbed on the metal surface. The corresponding mechanism is given by equation 1.12



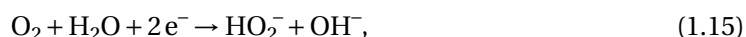
The second reaction pathway is known as the *Volmer-Heyrovsky mechanism*, which also starts with an adsorbed hydrogen atom on the metal surface according to the *Volmer reaction*. Other than in the *Tafel reaction*, the adsorbed hydrogen atom combines with a hydrogen proton from the electrolyte solution and an electron from the metal catalyst. This mechanism is known as the *Heyrovsky reaction* [65] and follows equation 1.13



The second reaction studied in this thesis is the reduction of oxygen, which occurs for example in fuel cells. Other than hydrogen evolution, the ORR requires four electrons instead of two, which increases the complexity of the reaction. With four electrons involved, the ORR can be reduced in a single step to water ( $\text{OH}^-$  in alkaline media), according to equation 1.14 [66]



The second reaction pathway occurs via a  $2+2\text{e}^-$  process: Two electrons are required to reduce oxygen to  $\text{H}_2\text{O}_2$  ( $\text{HO}_2^-$  in alkaline media) as an intermediate product (eqn. 1.15). Two additional electrons are necessary to reduce  $\text{H}_2\text{O}_2$  to water as the final product ( $\text{OH}^-$  in alkaline media), which is given by equation 1.16 [66]



In fuel cells oxygen reduction in a single step ( $4\text{e}^-$  mechanism via eqn. 1.14) is preferred, since it delivers higher energy values. The intermediate product  $\text{H}_2\text{O}_2$  in the  $2+2\text{e}^-$  mechanism can decompose on the catalyst surface according to equation 1.17, which limits the total energy output



Both half cell reactions (HER and ORR) require large overpotentials in alkaline electrolytes, which demands the utilization of stable catalysts for driving such electrochemical reactions efficiently. The best catalyst for both reactions is platinum [13, 15, 16, 61], a rare and expensive noble metal, which makes it worthwhile to substitute it by more abundant catalysts with similar activity. Throughout this thesis, metal electrodes have been combined with organic polymer co-catalysts in order to increase the overall catalytic activity and to provide further insight into the reaction mechanism on the molecular level.

### 1.1.5 Correlation between Binding Energy and Activity - The Volcano Plot

The correlation between the electrolytic hydrogen evolution and the M–H bond strength has been recognized for many years [67, 68]. It is based on the concept of the French chemist Paul Sabatier, who explained a high catalytic activity in heterogeneous catalysis with an optimal interaction value of reactants or reaction intermediates with the catalyst surface [69]. If the interaction is too weak, the intermediate does not bind to the catalyst, however if it is too strong the intermediate remains on the catalyst surface and blocks the catalytic active site.

Figure 1.4 illustrates an example of a volcano plot that contains the catalytic activity as a function of the Gibbs free adsorption energy of hydrogen on various transition metals. Electrodes that are made of platinum, palladium or rhenium show the highest catalytic activity and are almost located at the top of the volcano plot. Metal electrodes like gold and silver have a lower HER activity. By increasing the binding energy of hydrogen on such metals, the activity can be increased and these metals would move towards the top of the volcano plot. Metals like niobium and molybdenum reveal a similar catalytic activity to gold and silver. However the reason lies within hydrogen binding energies that are slightly too high. To improve the ability

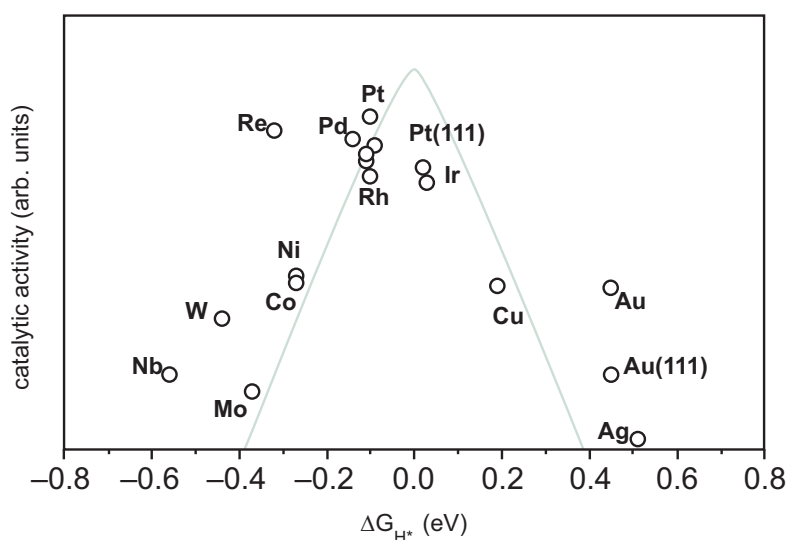


Figure 1.4 – Catalytic activity of HER versus the hydrogen binding energy, showing that intermediate binding energies result in a high catalytic activity (adapted with permission from Ref. [70]).

as HER catalysts of such metals, the hydrogen binding energy needs to be decreased, in order to move them closer to platinum and the top of the volcano plot.

The framework of the volcano plot that has been provided by Sabatier has also been demonstrated by density functional theory (DFT): It has been shown that the Gibbs free hydrogen binding energy depends predominantly on the hydrogen chemisorption energy. In addition, platinum was identified as the best catalyst for hydrogen evolution, due to its thermoneutrality, which means that the intermediate adsorbed state of hydrogen on platinum reveals almost no energy difference with respect to the energy states of reactants and products [71]. This phenomenon is missing in other HER catalysts like nickel, gold or molybdenum, which is the reason for their lower catalytic activity compared to platinum.

Recent studies include the binding energy of water, in order to achieve a more general description of the hydrogen binding energy. Since water represents the most abundant molecule in aqueous electrolytes, the catalyst surface is considered to be fully covered by water molecules. The Gibbs free energy of water adsorption is included to the calculation of the Gibbs free energy of the apparent hydrogen adsorption ( $\Delta G_{H,app}^0$ ), according to equation 1.18 [72]

$$\Delta G_{H,app}^0 = \Delta G_H^0 - \Delta G_{H_2O}^0. \quad (1.18)$$

The inclusion of water molecules allows to account for electrolytes with different pH values, since it is known that the pH affects the catalytic activity [73, 74, 75, 76]. It can be concluded from calculations that water has a weaker adsorption behavior in alkaline media compared to acidic electrolytes [72]. Consequently  $\Delta G_H^0$  is lower in alkaline electrolytes, which results in higher  $\Delta G_{H,app}^0$  values and hence lowers the catalytic activity by shifting the electrode material to higher binding energies in the volcano plot.

## 1.2 UHV-Methods

Ultra-high vacuum (UHV) condition was chosen in order to ensure a very clean environment during sample preparation and characterization. Molecular structures on metal substrates were fabricated by molecular beam epitaxy and scanning tunneling microscopy as major technique to visualize the real space topography of the electrode surfaces. X-ray photo electron spectroscopy (XPS) was used to determine the chemical composition of sample surfaces.

### 1.2.1 Scanning Tunneling Microscopy

The scanning tunneling microscope was invented in 1982 by Gerd Binnig and Heinrich Rohrer [77, 78]. It is a real space imaging technique, which enables the visualization and manipulation of particles on the atomic scale by scanning a conducting sample surface with a conducting tip (e.g. W or Pt/Ir). Only four years later Binnig and Rohrer were honored with the Noble Price

in Physics for their work, which they shared with Ernst Ruska.

The main principle of STM relies on quantum tunneling, which enables electrons to travel through an insulating gap, between two electrodes. The Bardeen theory explains the metal-insulator-metal tunnel junction by considering two separate electrodes [79]. Equation 1.19 describes the wave function of two electrodes A and B that satisfy the Schrödinger equation of a free electrode.  $U_A$  and  $U_B$  represent the potential function of each electrode and  $\Psi$  is the wave function of the stationary states

$$i\hbar \frac{\partial \Psi}{\partial t} = \left[ -\frac{\hbar^2}{2m} \frac{\partial^2}{\partial z^2} + U_{A,B} \right] \Psi. \quad (1.19)$$

The wave functions of both electrodes A and B will decay into the vacuum barrier. However, if the distance  $z$  between the two electrodes is reduced, the combined system implements both potential functions  $U_A$  and  $U_B$  according to equation 1.20. A corresponding scheme is visualized in figure 1.5 (a)

$$i\hbar \frac{\partial \Psi}{\partial t} = \left[ -\frac{\hbar^2}{2m} \frac{\partial^2}{\partial z^2} + U_A + U_B \right] \Psi. \quad (1.20)$$

By approaching the potentials of electrode A and B provides a probability of electrons from electrode A to appear in the states of electrode B, which can be described by equation 1.21, with the wave function  $\psi_\mu$  and the energy states  $E_\mu$  of electrons in electrode A.  $\psi_\nu$  and  $E_\nu$  represent the wave function and the energy of electrons in electrode B

$$\Psi = \psi_\mu e^{-iE_\mu t/\hbar} + \sum_{\nu=1}^{\infty} c_\nu(t) \psi_\nu e^{-iE_\nu t/\hbar}. \quad (1.21)$$

For deriving the tunnel current between two electrodes A and B, a tunneling matrix element  $M_{\mu\nu}$  is defined (eqn. 1.22), with the two sets of wave functions being approximately orthogonal:  $\int \psi_\mu^* \psi_\nu d^3r \approx 0$ :

$$M_{\mu\nu} = \int_{z>z_0} \psi_\mu U_B \psi_\nu^* d^3r. \quad (1.22)$$

Equations 1.20 and 1.21 with the tunneling matrix element  $M_{\mu\nu}$  are used to derive the probability  $p_{\mu\nu}(t)$  of the  $\nu$ -th state to appear in electrode B at a particular time  $t$  (eqn. 1.23)

$$p_{\mu\nu}(t) = |M_{\mu\nu}|^2 \frac{4 \sin^2[(E_\mu - E_\nu)t/2\hbar]}{(E_\mu - E_\nu)^2}. \quad (1.23)$$

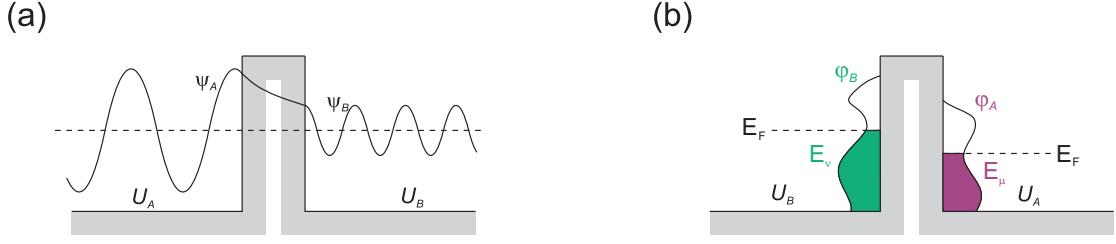


Figure 1.5 – Bardeen tunneling theory for the one dimensional case: (a) Wave function can penetrate a potential barrier due to quantum tunneling; (b) Small distance between the electrodes allows electrons of electrode B can tunnel into the empty states of electrode A.

If  $E_\mu = E_v$  the factor  $\frac{4\sin^2[(E_\mu - E_v)t/2\hbar]}{(E_\mu - E_v)^2}$  in equation 1.23 will reach its maximum, which describes the condition of elastic tunneling. Including this requirement, the tunneling current depends on the number of states in electrode B that can tunnel into states of electrode A, which is ultimately described by the density of states  $\varphi_B(E)$  at the energy  $E$ . This is summarized in equation 1.24, which gives the probability of electrons from B-states to appear with the energy  $E_\mu$  in the states of electrode A. This case is graphically illustrated in figure 1.5 (b)

$$p_{\mu\nu}(t) = \frac{2\pi}{\hbar} |M_{\mu\nu}|^2 \varphi_B(E_\mu) t. \quad (1.24)$$

Deriving an equation for the tunneling current from equation 1.24 requires the elementary charge  $e$  and the density of states of both electrodes at the Fermi level ( $\varphi_A(E_F)$  and  $\varphi_B(E_F)$ ). An energy difference  $\Delta E = eV$  between the Fermi level of each electrode can be induced by applying a bias voltage  $V$ . Combining these requirements with equation 1.24 delivers the tunneling current, which is given by equation 1.25

$$I = \frac{2\pi e^2}{\hbar} |M_{\mu\nu}|^2 \varphi_B(E_F) \varphi_A(E_F) V. \quad (1.25)$$

In the gap region, the wave functions of both electrodes decay according to  $\psi_{\mu,\nu} = \psi_{\mu,\nu}(0) e^{-\kappa z}$ , with  $\kappa$  being the decay constant and  $z$  the distance between the two electrodes A and B. It has been shown that the tunneling matrix element  $M_{\mu,\nu}$  depends on the decay factor of the wave function  $M_{\mu,\nu} \propto e^{-\kappa z}$ , which is explained in detail in Ref. [79]. In the set-up of an scanning tunneling microscope the two electrodes described in the Bardeen model correspond to the STM tip and the sample. In a simple approximation, the density of states of the tip can be regarded as a constant, since they do not change throughout an STM experiment. In consequence, the tunneling current does only depend on the local density of states ( $\varphi_{LDOS}$ ) of the sample, the applied bias voltage  $V$  and the distance  $z$  between tip and sample. Combining these simplifications, the tunneling current can be rewritten in a simplified version

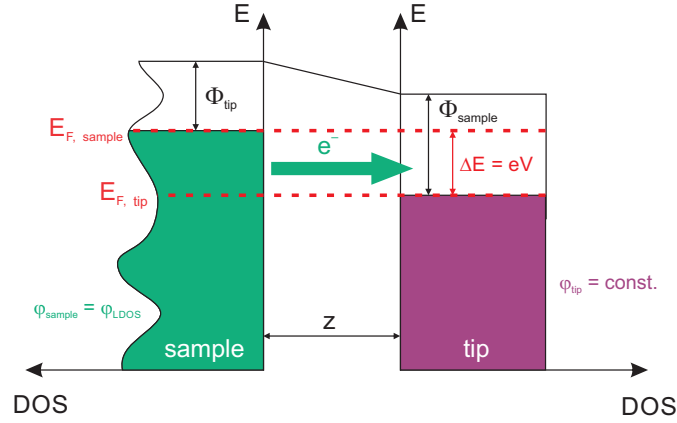


Figure 1.6 – Energy diagram of a tip-sample junction with the work functions of tip  $\Phi_{tip}$  and sample  $\Phi_{sample}$ : Fermi level of the sample  $E_{f, sample}$  is higher than the Fermi level of the tip  $E_{f, tip}$ , which results in the tunneling of electrons from the occupied states in sample into the unoccupied states within the tip.

according to equation 1.26

$$I \propto V \phi_{LDOS} e^{-\kappa z}. \quad (1.26)$$

The STM tunneling junction is graphically shown in figure 1.6: Electrode B is represented by the sample with its local density of states (LDOS). Electrode A is represented by the STM tip and the corresponding density of states are constant. The Fermi levels of sample and tip are shifted by an energy interval  $\Delta E$  with respect to each other by applying a bias voltage  $V$ . In consequence, electrons can tunnel from the occupied sample states into the empty states of the tip.

In order to create an overall image of the sample surface, the STM tip needs to probe the surface on the atomic scale. To achieve the controlled movement on the sub-nanometer scale, piezo elements are used. By applying an electric field to the piezo ceramics, mechanical stress occurs that results in contraction or elongation of the piezo (inverse piezoelectric effect)[80]. Implementing three piezo elements allows a controlled movement of the STM tip in three dimensions and to scan the sample surface. The x and y piezo ensure lateral scanning, while the z piezo controls the height of the tip. Alternatively, a pietolectric tube can be used, which is able to scan in x, y and z directions.

During scanning the tunneling current is recorded and compared with a reference value. If the recorded current is higher than the reference value, a voltage is applied to the z-piezo by a feedback loop and the tip withdraws from the surface. If the tunnel current is lower than the set point, the z-piezo will expand in order to hold the reference current. The measured tunneling currents are transferred to a color-scale image for visualizing the topography of the sample. Bright areas represent areas of high topography, while dark areas correspond to depressions



within the sample morphology. It is important to be mentioned that the interpretation of STM images is not always straight forward and effects in STM images are not always related to the topography which results from the convolution of the topography with the LDOS of the sample at the Fermi level.

This phenomenon can be explained by figure 1.7, which illustrates a Au(111) surface covered with a monolayer of porphyrin molecules (Fe-Tetrapyrridyl-porphyrin). The insert in the top right corner exhibits a single molecule with an overlay of the corresponding chemical structure. The bright contrast in the center of the molecules represents an interplay of topography and the LDOS of the iron center inside the molecule adsorbed on the Au(111) surface. Visualizing such local effects makes STM a very powerful technique. It is chosen to image the surface of the samples investigated in this thesis, since it can grant insight into the catalyst surface and is capable of identifying the catalytic active sites with utmost precision.

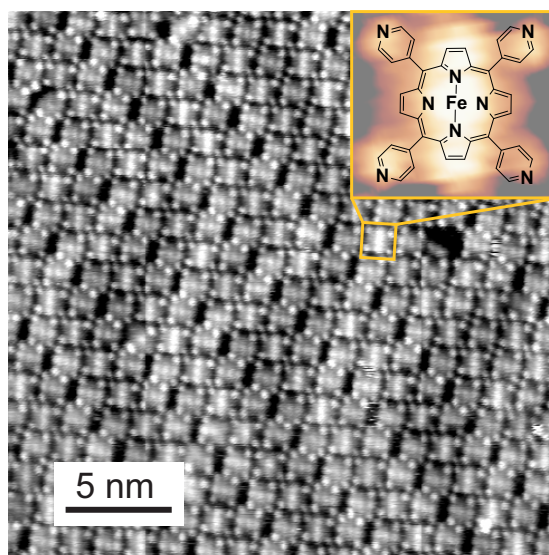


Figure 1.7 – High resolution STM topograph ( $U = -1.3$  V,  $I = 120$  pA) of Fe porphyrin molecules covering the surface of a Au(111) crystal recorded at room temperature: Sub-molecular resolution is obtained within the molecules showing the different components of the porphyrin molecules; Insert show a single molecule with an overlay of the chemical structure.

In addition to image recording it is possible to perform Scanning Tunneling Spectroscopy (STS), which delivers further insight into the density of states of the investigated sample. This can be realized due to the proportional relation between the tunneling conductance  $\partial I / \partial V$  and the LDOS. By performing STS on molecules the highest occupied as well as the lowest unoccupied molecular orbitals (HOMO and LUMO) can be detected, which has been performed in Ref. [1] on iron and cobalt porphyrins. In the upcoming studies that are discussed in this thesis, tunneling spectroscopy is not further utilized.

### 1.2.2 X-ray Photoelectron Spectroscopy

This section presents the fundamentals of X-ray photoelectron spectroscopy (XPS), which is a quantitative spectroscopic technique to determine the elemental composition on surfaces. Other than STM, which is a localized technique and operates on the atomic scale, XPS provides an averaged signal of several square millimeters. XPS has its origin in 1887, when Heinrich Hertz discovered the photoelectric effect [81]. The explanation was given 18 years later by Albert Einstein, who introduced the wave-particle duality of electromagnetic radiation and described light as quantized particles known as photons [82]. In consequence, illuminating any material with electromagnetic radiation results in the emission of electrons. For this discovery Einstein was honored with the Noble Prize in Physics in 1921. The electromagnetic radiation used in XPS are X-rays, which usually originate from Al  $K_\alpha$  (1487 eV) or Mg  $K_\alpha$  (1253.6 eV). In ultra-violet photoelectron spectroscopy (UPS) X-ray radiation is replaced by ultra-violet light that operates at energies between 10 and 100 eV. Some experiments require a higher resolution in order to obtain further knowledge of the XPS spectra. Therefore, synchrotron radiation is used, since it has a higher intensity, which is basically a higher amount of photons per area. For this work the application of Mg  $K_\alpha$  radiation was sufficient and was used in all XPS experiments throughout the entire thesis.

Figure 1.8 shows the schematic relation between the sample and the spectrometer. Electrons of the sample are emitted by electromagnetic radiation with the energy  $h\nu$  (orange arrow in fig. 1.8) and are detected by the spectrometer with a kinetic energy  $E_{kin,sp}$ , which can be calculated by equation 1.27, with  $|E_B|$  representing the binding energy of the emitted electrons

$$E_{kin,sp} = h\nu - \Phi_{sp} - |E_B|. \quad (1.27)$$

It is important to mention that the electrons have the work function  $\Phi_s$  and leave the sample surface with the kinetic energy  $E_{kin,s}$ . However they are detected in the spectrometer with the kinetic energy  $E_{kin,sp}$ . Therefore it is important that the Fermi levels of sample and spectrometer are aligned, which results in  $E_{kin,sp} + \Phi_{sp} = E_{kin,s} + \Phi_s$ . Technically this is realized by an electrical contact between sample and spectrometer. In consequence the binding energy  $E_B$  of the electrons can be determined by the kinetic energy  $E_{kin}$  that is measured by the spectrometer (red arrow in fig. 1.8).

In addition to the elemental composition, XPS allows to determine oxidation and binding states. The binding energy is directly influenced by the core, which means electrons are attracted by the protons within the core. Ionizing an element or changing the bonding partner directly affects the electrons in the atomic shell, represented by the partial charge of the atom. This will change the binding energy per electron and will result in a chemical shift to higher binding energies, if the negative charge in the shell is reduced. The binding energy will be lower, if the negative charge within the atomic shell is increased. Figure 1.9 shows an example for the chemical shift of the 1s core level of nitrogen. The spectra shows the signal of pyridinc

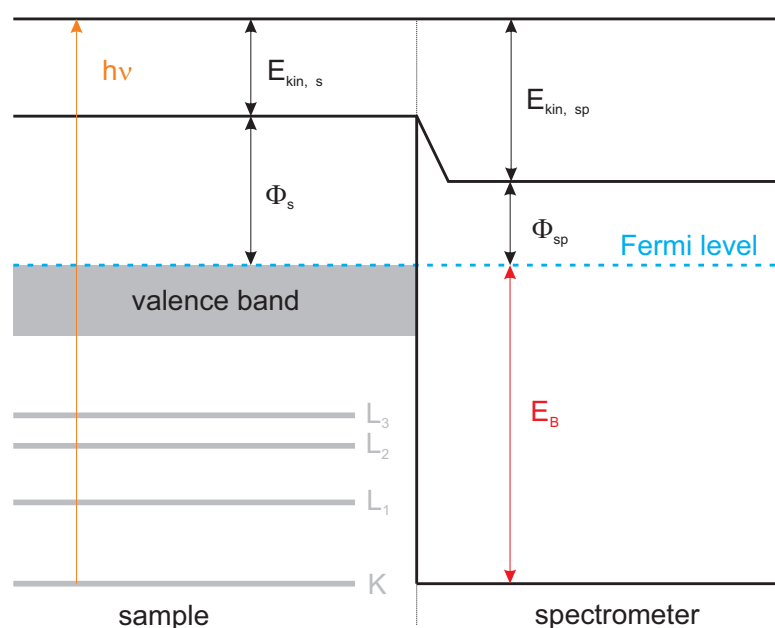


Figure 1.8 – Relation between energy levels of a sample and the spectrometer: One electron is excited by electromagnetic radiation with the energy  $h\nu$  from the K shell and has the kinetic energy  $E_{kin,s}$  after overcoming the work function  $\Phi_s$ ; By aligning the Fermi levels of sample and spectrometer the binding energy  $E_B$  of the excited electron can be determined with the kinetic energy  $E_{kin,sp}$  measured by the spectrometer.

nitrogen around 398 eV and the signal of quaternary nitrogen around 400.8 eV. Additionally the theoretical position of pyrrolic nitrogen is added at 400 eV [83] by a grey dashed line. Comparing these chemical groups, pyridinic nitrogen has the lowest binding energy. The partial charge is lower than in pyrrolic nitrogen, since only two coordination neighbors are available. Pyrrolic nitrogen has three binding partners, which affects the partial charge and therefore core electrons have a higher binding energy. Quaternary nitrogen appears in the oxidized state and is positively charged, which results in less electrons in the atomic shell. In conclusion electrons in quaternary nitrogen experience an even higher binding energy.

It has to be mentioned that the classification of pyridinic and pyrrolic nitrogen is not always straight forward in literature. Pyridinic nitrogen refers to the molecule pyridin, which is a benzene ring with one carbon atom replaced by nitrogen. Therefore pyridinic nitrogen has two carbon neighbors that are  $sp^2$  hybrids. Due to the molecule pyrimidin, it is usually assumed that pyridinic nitrogen is situated in a six-membered ring. It is not defined, if a nitrogen atom in a five membered ring with two  $sp^2$  hybrid neighbors can also be referred as pyridinic [84]. The term "pyrrolic nitrogen" relies on the pyrrol molecule, a five membered carbon ring with nitrogen replacing one carbon atom. In addition, a hydrogen atom is bond to nitrogen. Consequently, pyrrolic nitrogen describes a nitrogen atom in a five membered ring with two  $sp^2$  carbon atoms as neighbors and one bond to a hydrogen atom. The question if a nitrogen atom bond to hydrogen in a six membered ring can also be named "pyrrolic" remains open. Since it is known that the coordination number of nitrogen has the major effect rather than

the local geometry (ring size), the long-range order will be neglected during the discussion of XPS spectra in this thesis. Nitrogen with two  $sp^2$  carbon atoms as neighbors will be referred to as "pyrimidinic". Analogously, nitrogen with two  $sp^2$  coordinated carbon atoms and one hydrogen atom will be referred to as "pyrrolic".

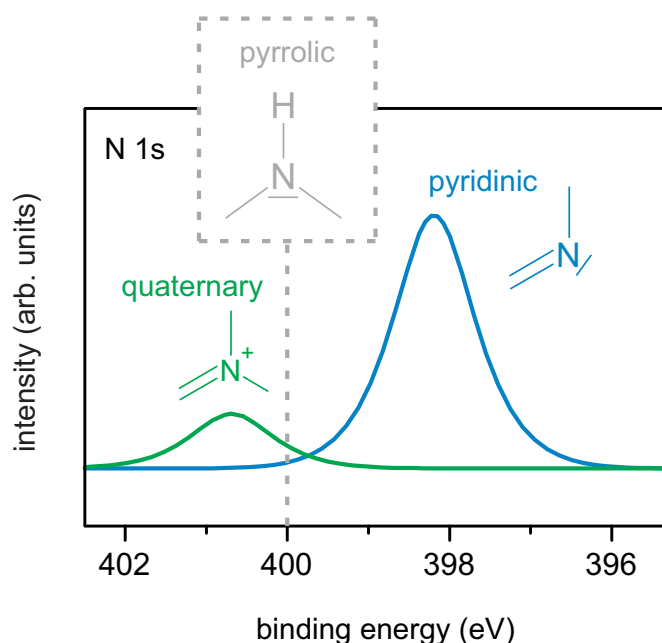


Figure 1.9 – Chemical shift of the N 1s core levels: The chemical shift arises due to different coordination of nitrogen: Pyridinic nitrogen with two coordinated carbon atoms has the lowest binding energy; Pyrrolic nitrogen with three coordinated neighbors has a larger binding energy, while quaternary nitrogen, which is in the oxidized state has the highest binding energy in this spectrum.

## 1.3 Combination of Vacuum and Electrocatalysis

### 1.3.1 Experimental Apparatus

In this section, the experimental apparatus will be presented. It involves several vacuum chambers for sample preparation and STM, an electrochemical set-up and an X-ray photoelectron spectroscope. Figure 1.10 shows an schematic overview of the applied experimental techniques throughout this thesis. The preparation chamber is equipped with several turbo pumps and an ion getter pump in order to operate at  $8 \times 10^{-10}$  mbar. An ion gun enables to sputter metal substrates with noble gas ions (fig. 1.10 a). To smooth the metal surface after sputtering, the crystal was annealed by electron bombardment with high-voltage applied to the sample. The deposition of organic molecules is performed by an four pocket molecular beam evaporator (Dodecon Nanotechnology GmbH) and is schematically added in figure 1.10 b. Quartz crucibles are assembled inside the evaporator and act as Knudsen cell, which implies a small opening of the sublimation cell. The small opening maintains the equilibrium pressure inside the crucible [85]. A single beam metal evaporator (Omicron electronics GmbH)

is added to the preparation chamber in order to sublime metals (fig. 1.10 c).

Following figure 1.10 (No. 2) the topography of the fabricated samples is characterized by a home-build STM. Like the preparation chamber, the vacuum chamber where the STM is located, is equipped with several turbo pumps and an ion getter pump to maintain a pressure of  $1 \times 10^{-10}$  mbar. STM tips are prepared by electrochemical etching of tungsten wire (MaTeck GmbH) in a 2 M NaOH solution (solid NaOH 99 %, Merck KGaA). Tips are introduced into the vacuum after electrochemical preparation in order to minimize oxidation and mounted in a STM head with linear z-piezo (attocube systems AG). Imaging the topography of the sample is performed at room temperature. The bias voltage is applied to the STM tip and the sample is positioned in a base plate with four metal strings to minimize mechanical vibration.

For combining the sample fabricated in UHV with the electrochemical cell at ambient pressure, a third chamber is needed, which acts as transfer chamber (fig. 1.10 No. 3). The base pressure of the transfer chamber is  $8 \times 10^{-8}$  mbar. The sample is transferred from the STM chamber to the transfer chamber and mounted to the local manipulator by using a wobble stick. When every valve to the transfer chamber is closed, it is subsequently flooded with argon gas (purity 5.0) until a pressure of 1 bar is reached. The electrochemical cell is mounted at the bottom of the transfer chamber (fig. 1.10 No. 4) and also flooded with argon gas in order to minimize the contamination of the transfer chamber with atmospheric air. As soon as ambient pressure in the transfer chamber is reached, the gate valve between chamber and electrochemical cell is opened. The sample in the manipulator can be moved downwards and the arrangements for the electrochemical experiments can start, which are described in the upcoming section, when the electrochemical cell is described in detail.

A vacuum suitcase (ferrovac GmbH) is used, if the sample needs to be transferred to a different vacuum set-up, such as the X-ray photoelectron microscope (fig. 1.10 No. 5). XPS measurements were performed with an analysis chamber with a hemispherical SPECS PHOIBOS 150 energy electron analyzer with an energy resolution of approximately 15 meV with a base pressure of  $5 \times 10^{-10}$  mbar. The axis of the analyzer is orthogonal to the sample surface and the X-ray beam has an inclination of approximately  $45^\circ$  to the sample surface. XPS experiments were performed with non-monochromatic  $\text{Mg K}\alpha$  source with a photon energy of  $h\nu = 1253,6$  eV. The spot size of the X-ray beam is approximately  $1 \text{ mm}^2$ . All XPS experiments were carried out at room temperature (300 K).

#### 1.3.2 Transfer into the Electrochemical Cell

The electrochemical cell used in this thesis is a conventional three-electrode set up, with the sample fabricated in UHV acting as working electrode. The cell has four openings to insert the reference and counter electrode, the electrolyte solution and a device for bubbling the electrolyte with gases. For a controlled atmosphere within the electrochemical cell, two teflon taps are attached in order to guarantee a clean environment: One teflon tap is used to evacuate the cell and fill it with inert argon gas, while the second tap is used as gas outlet. The

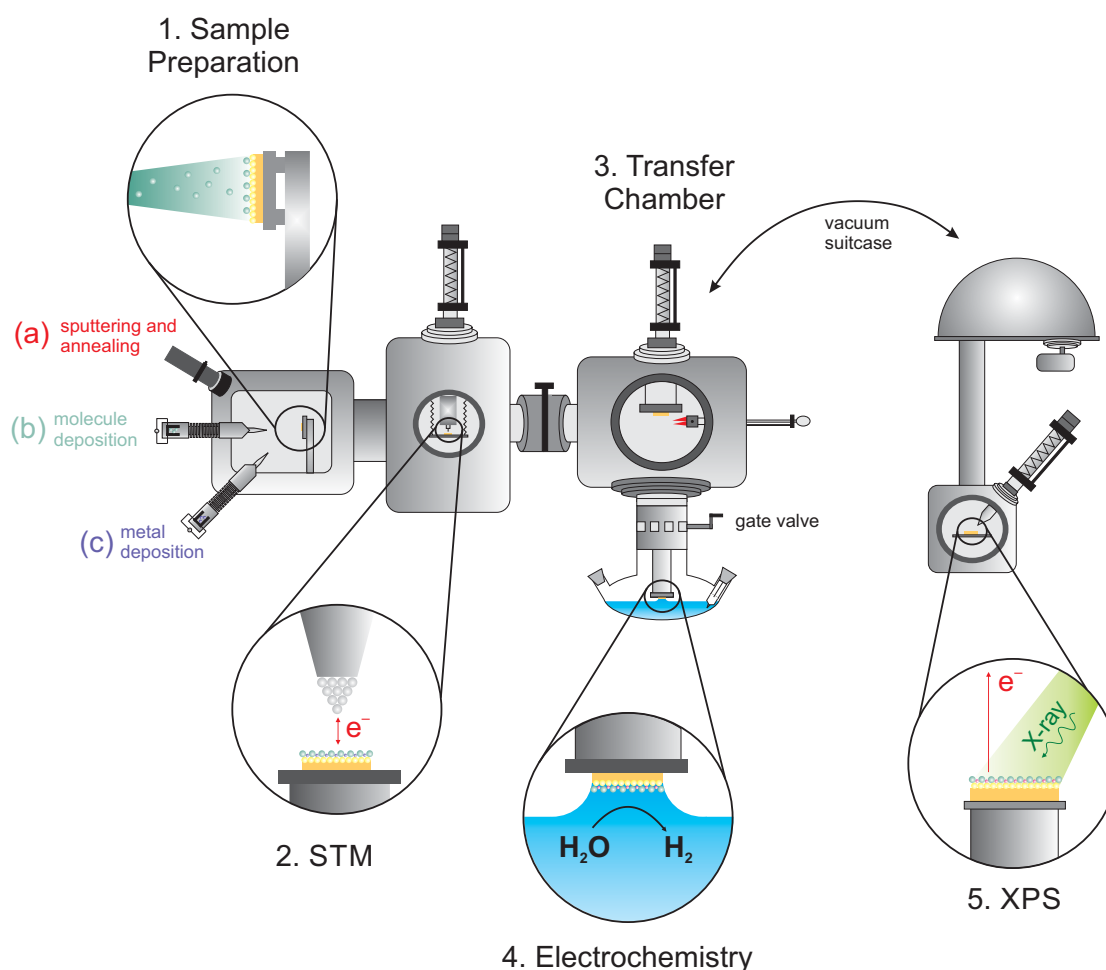


Figure 1.10 – Schematic overview of the applied methods throughout this thesis: Cleaning of the metal substrate by sputtering and annealing (No. 1a) and deposition of organic molecules (No. 1b) or metal deposition (No. 1c); Characterization of the sample topography by STM (No. 2); Transfer chamber (No. 3) in order to ensure a clean environment during transferring the sample to the electrochemical cell (No. 4) for electrocatalytic experiments or to the XPS (No. 5) by a vacuum suitcase.

working electrode is mounted face down inside the cell and electrochemical experiments are performed in the hanging meniscus configuration [86, 87]. Therefore a drop making device is used. The electrochemical cell and the drop maker are filled with the electrolyte solution and the working electrode is positioned closely to the drop maker. By using a syringe, the solution in the drop maker can be precisely ejected and a drop can be formed at the working electrode (fig. 1.11 a). After moving the drop maker in a parking position, the working electrode is moved downwards towards the electrolyte and a meniscus is formed in contact with the electrolyte solution. This procedure enable a localized wetting of the sample surface and ensures that other areas of the sample or the sample holder will not get wet.

After electrochemical measurements a second drop maker is used in order to rinse the surface of the working electrode with milliQ water and to remove electrolyte residue. The final step

is to flush the sample surface with argon air and remove liquids from the surface before the sample is introduced back into vacuum.

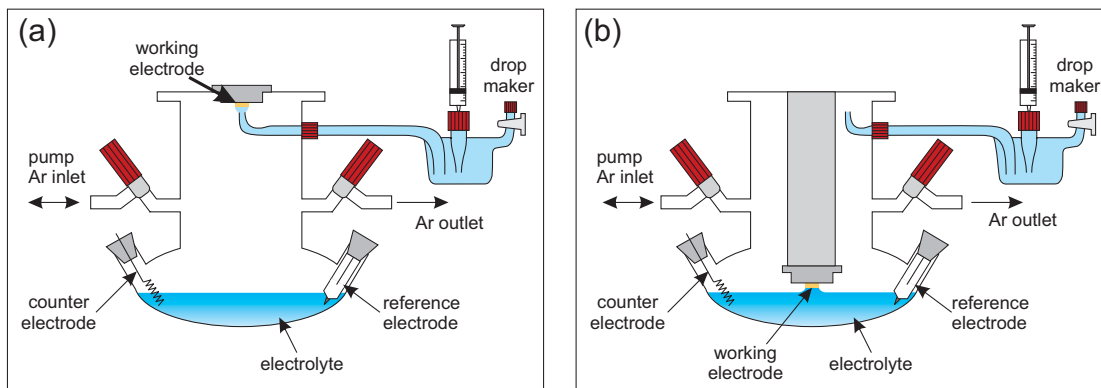


Figure 1.11 – Schematic illustration of the electrochemical cell: Conventional three electrode set-up with reference-, counter- and working electrode; Ar inlet and outlet are regulated by teflon taps; Experiments are performed with a hanging meniscus: (a) Establishing the drop at the working electrode with the drop maker; (b) Moving working electrode downwards and creating the meniscus between sample and electrolyte.

#### 1.3.3 Sample Preparation

All UHV experiments presented in this thesis have been performed on Au(111) single crystals (MaTeck GmbH and Surface Preparation Laboratory B.V.). The crystals exhibit a hat shape form and have an orientational misfit below  $0.1^\circ$ . Sample cleaning was performed by repeating  $\text{Ar}^+$ -sputtering and subsequent annealing by electron bombardment up to 825 K. The sputter beam had an energy of 1 keV and hits the sample surface with an angle of  $45^\circ$ . The measured  $\text{Ar}^+$  flux reached  $10 \mu\text{A}$  during sputtering. During the annealing process the pressure was below  $3 \times 10^{-9}$  mbar (higher during first annealing after an electrochemical experiment). After electrochemistry three sputtering and annealing cycles were sufficient in order to obtain a flat surface with atomically flat terraces around  $100 \text{ nm}^2$ .

Fabrication of covalent organic networks on Au(111) substrates was performed by using an organic molecule evaporator. The used precursor molecules are 2,4,6-tris-(4-bromophenyl)-1,3,5-triazine ( $\text{N}_3$ ) and 2,2',2''-(benzene-1,3,5-triyl)-tris-(5-bromopyrimidine) ( $\text{N}_6$ ). Both molecules were synthesized by the group of Prof. Bettina Lotsch (Max Planck Institute for Solid State Research, Department for Nanochemistry, Stuttgart Germany). The molecule 1,3,5-tris-(4-bromophenyl)-benzene ( $\text{N}_0$ ) is commercially available (Sigma Aldrich). During molecule deposition the Au(111) substrate was heated, in order to initiate polymerization and release molecular bromine according to an Ullmann-like coupling pathway [88, 89, 90, 91, 92]. During the polymerization the precursor molecules  $\text{N}_0$ ,  $\text{N}_3$  and  $\text{N}_6$  build up the polymer structures  $\text{P-N}_0$ ,  $\text{P-N}_3$  and  $\text{P-N}_6$ . Table 1.1 shows the details about molecule deposition including chemical name, sublimation temperature  $T_{\text{Sub}}$ , temperature of the Au(111) crystal  $T_{\text{Au(111)}}$  and the supplier.

Molecule	Chemical Name	$T_{Sub}$	$T_{Au(111)}$	Supplier
N <sub>0</sub>	1,3,5-tris-(4-bromophenyl)-benzene	475 K	560 K	Sigma Aldrich
N <sub>3</sub>	2,4,6-tris-(4-bromophenyl)-1,3,5-triazine	565 K	560 K	synthesized
N <sub>6</sub>	2,2',2''-(benzene-1,3,5-triyl)-tris-(5-bromopyrimidine)	560 K	560	synthesized

Table 1.1 – Experimental details for preparing the organic molecular structures on Au(111) including sublimation temperature  $T_{Sub}$  and temperature of the Au(111) crystal  $T_{Au(111)}$  as well as the abbreviation of the molecule throughout this thesis .

### 1.3.4 Electrochemical Experiments

Electrochemical experiments have been performed with an Autolab PGSTAT302N potentiostat (Metrohm GmbH & Co. KG). The hardware was operated with the implemented Nova 2.1 software. The conventional three electrode set-up includes a Ag/AgCl (3 m KCl) reference electrode and a platinum wire as counter electrode. Electrocatalytic experiments were performed with a 0.1 M NaOH electrolyte. The solution was prepared in the laboratory with NaOH pellets (Sigma Aldrich 99,99 %) and dissolved in milliQ water ( $R = 18,2 \text{ M}\Omega$ ). Prior to HER experiments the electrolyte solution was bubbled with Argon gas (purity: 5.0) for 20 mins. For ORR experiments the electrolyte was enriched with oxygen (purity: 5.0) for 20 mins. Details on the scan rate and the potential window are indicated in the corresponding chapter.



## 2 Structural Short-Range Correlations in Organic Polymer Networks<sup>1</sup>

The study of polymer structures on metal surfaces has been of particular interest for the last decade. Numerous amounts of different structural motifs can be created in UHV [49, 50], by connecting molecular building blocks: Linear chains can be fabricated [93], which can assemble as monolayers and cover entire surfaces [94]. Branched covalent chains form 2D structures, which show different pore sizes [95] and robust polymers can be fabricated by incorporating transition-metal centers [96]. The fabrication of defect-free polymer sheets remains challenging [97] and porous structures often implement defects and grow as amorphous networks [98]. The reason in polymer structures is the covalent bond, which is often irreversible [99]. Once a covalent bond is formed, it cannot be easily broken again in order to clear polymer networks from defects, which restricts the structure from evolving towards the thermodynamic equilibrium.

However, amorphous systems show a number of interesting properties, which makes them worth to study: Amorphous organic solids can produce pinhole-free films, which are in addition smoother than the crystalline counterpart [100]. The band gap of graphene can be opened by adding defects and incorporate in-gap states [101]. Furthermore, the engineering of molecular building units changed the properties of photocatalysts, in order to increase the activity in hydrogen evolution [37].

This chapter describes similar building units that build up two different 2D polymer structures. The used precursor molecules differ in the chemical composition, as one molecule contains nitrogen heteroatoms, while the other one has only carbon and hydrogen atoms in its structure. Polymerization was applied under similar growth conditions for both systems, resulting in different defect densities. Ring sizes and ring size combinations were compiled manually and compared to molecular dynamics (MD) simulations, which are helpful to provide further insight into structural correlations in 2D polymers. The results within this chapter are published in reference [2].

---

<sup>1</sup>This chapter and the presented results are based on ref. [2]

## 2.1 Experimental and Theoretical Methods

The basis for the experimental part for determining the structure of organic polymers on gold is STM in a vacuum chamber at a pressure below  $5 \times 10^{-10}$  mbar. The Au(111) substrate was cleaned by several  $\text{Ar}^+$  sputtering and annealing cycles (825 K). The investigated organic polymers were synthesized by 1,3,5-tris-(4-bromophenyl)-benzene ( $\text{N}_0$ ) and 2,4,6-tris-(4-bromophenyl)-1,3,5-triazine ( $\text{N}_3$ ). The precursor molecules were evaporated from a quartz crucible in UHV and polymerization follows an Ullman-type coupling pathway in which two aryl groups are connected by a covalent bond and release molecular bromine (fig: 2.1 a). During the polymerization the precursor molecules  $\text{N}_0$  and  $\text{N}_3$  build up the polymer networks  $\text{P-N}_0$  and  $\text{P-N}_3$  and the Au(111) crystal was held at 475 K for  $\text{N}_0$  and 565 K for  $\text{N}_3$ .

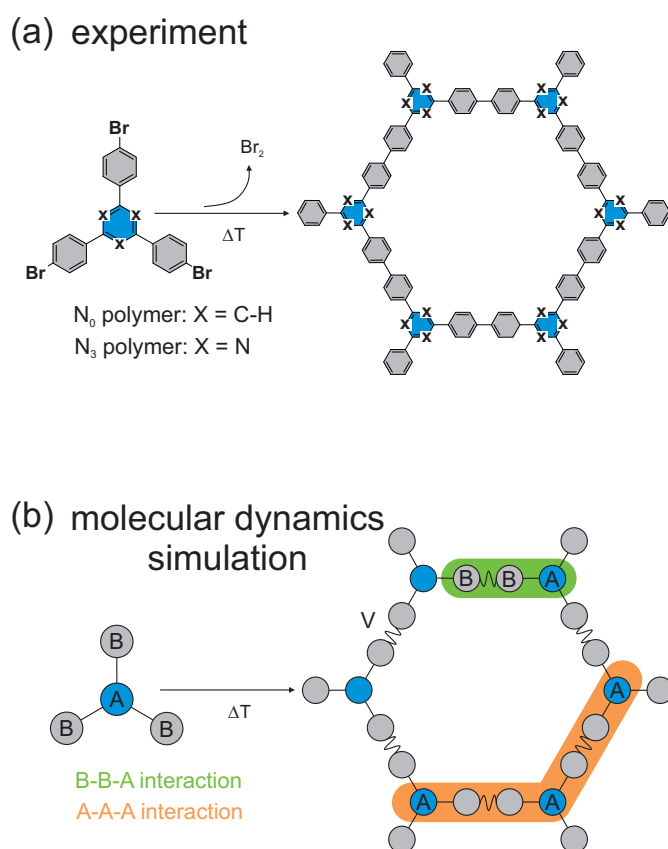


Figure 2.1 – (a) Experimental synthesis following an Ullmann-like coupling pathway (b) Model used during molecular dynamics simulations with the central subunit A, the surrounding trigonal subunits B and the intermolecular potential V.

The experimental statistics was collected by counting ring size combinations manually from large-area overview STM images. Therefore only closed pores were considered for distribution analysis. Pores that imply defects or more than nine precursor molecules were not included in the statistics. To analyze the local short-range environment, clusters are introduced that are called  $\alpha\beta\gamma$  triplets in the following sections. Each triplet has a central vertex that represents one precursor molecule and contributes to three adjacent polygons, due to the three available

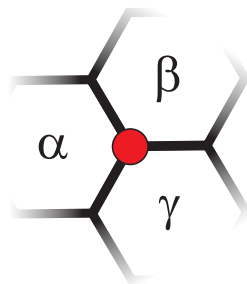


Figure 2.2 – Schematic model of a  $\alpha\beta\gamma$  triplet: The central red point marks the vertex of the triplet and  $\alpha$ ,  $\beta$  and  $\gamma$  represent the size of the pores that share a common vertex.

ligands. In consequence, each vertex describes the structural short-range environment of its neighboring polygons and  $\alpha$ ,  $\beta$  and  $\gamma$  label the size of the adjacent polygons. The sequence within the triplets is not incorporated in this notation and has no effect on the short-range order. Figure 2.2 shows a schematic illustration of a  $\alpha\beta\gamma$  triplet. The red point in the center indicates the central vertex and  $\alpha$ ,  $\beta$  and  $\gamma$  represent the ring size of the pores that surround the vertex in the center. A similar investigation has been recently applied to characterize short-range interactions in 2D silicon oxide [102]. If short-range correlations are ignored an expected distribution of  $\alpha\beta\gamma$  triplets based on a given ring size distribution can be calculated by equation 2.1

$$P(\alpha, \beta, \gamma) = P_\alpha \times P_\beta \times P_\gamma \times f(\alpha, \beta, \gamma). \quad (2.1)$$

In this mean-field like approximation  $f(\alpha, \beta, \gamma)$  represents the multiplicity. It equals one, if the neighboring pores have the same size ( $\alpha\alpha\alpha$ ). The multiplicity equals three, if two pores have the same size ( $\alpha\alpha\beta$ ) and equals six, if all pores have a different size ( $\alpha\beta\gamma$ ). The components  $P_\alpha$ ,  $P_\beta$  and  $P_\gamma$  are the probabilities of an  $\alpha$ -gon,  $\beta$ -gon and  $\gamma$ -gon and are taken from relative distribution of ring size histograms. This mean-field model is valid if pores are randomly distributed in the structure. Deviations from this model will occur, if the pores are not randomly distributed, for example, if a pore of size  $\alpha$  imposes constrain on the size of adjacent pores  $\beta$  and  $\gamma$ . Figuring out if such a correlation exists is the topic of this chapter.

Besides of the calculation of expected structures with no short-range correlation using equation 2.1, the main objective of the simulations in this work is to mimic the experimentally observed ring-size distribution of the P-N<sub>0</sub> and P-N<sub>3</sub> organic polymers. Therefore, molecular dynamics (MD) was used, which includes up to 5750 molecules per periodically repeated simulation cell. All MD simulations were performed by Christina Oligschleger (Hochschule Bonn-Rhein-Sieg, Rheinbach, Germany) and Christian Schön (Max Planck Institute for Solid State Research, Stuttgart, Germany). A simplified model has been created that incorporates all

the important molecular interactions and to describe each precursor molecule as a building block that contains of a central subunit A surrounded by three additional subunits B with trigonal symmetry. The resulting building blocks AB<sub>3</sub> are treated as quasi-rigid and represent the precursor molecules for the experimental synthesis (fig. 2.1 b). Interactions occur only between such AB<sub>3</sub> units and are described by a two- and three-body contribution. The force field between AB<sub>3</sub> building blocks is described by equation 2.2: Two-body conditions are described by a Lennard-Jones potential for short-range interactions and a quasi Coulomb term is added to account for long-range interactions. The last term in equation 2.2 is implemented for three-body interaction and is calculated by a Stillinger-Weber potential. It is used to account for two different interaction types: A-A-A interactions involve three different AB<sub>3</sub> units and each A represents a different center of a building block. The second interaction is described by a B-B-A interaction, where B of an unit interacts with a B-A subunit of another building block. Figure 2.1 (b) shows a schematic A-A-A interaction in orange and a B-B-A interaction in green. The preferred angles for the simulation are 120° for A-A-A and 180° for B-B-A. Deviations from these optimal angles are implemented by the  $b_{ijk}$  energy parameter in the Stillinger-Weber model (eqn. 2.2). Intuitively, the B-B-A interaction describes how strongly two molecules couple to each other and the A-A-A interaction encodes how stiff the angles between two molecules are:

$$V = \sum_{i,j=1}^N \left[ \epsilon_0 \left( \left( \frac{r_0}{r_{ij}} \right)^{12} - 2 \left( \frac{r_0}{r_{ij}} \right)^6 \right) + \frac{q_i q_j}{r_{ij}} \right] + \sum_{i,j,k=1}^N \left[ b_{ijk} \cdot \exp \left( \frac{\lambda_{ij}}{r_{ij} - r_{0,ij}} + \frac{\lambda_{ik}}{r_{ij} - r_{0,ik}} \right) \cdot (\cos(\theta_{ijk}) - \cos(\theta_{0,ijk}))^2 \right]. \quad (2.2)$$

Since the precursor molecules of P-N<sub>0</sub> and P-N<sub>3</sub> differ in their chemical composition, the potential parameters in the MD calculations are adjusted. During the MD runs, the structures are annealed to 2650 K and the MD time step is 2 fs with a total amount of 120000 steps for the complete simulation. A detailed account of the theoretical model can be found in reference [2].

## 2.2 Results on the Catalyst Structure

The upcoming chapter presents the pore size distribution and the local environment of the P-N<sub>0</sub> and P-N<sub>3</sub> network. The experimental section shows the pore size distribution acquired from STM images. In addition  $\alpha\beta\gamma$  clusters are compared with cluster distributions calculated by equation 2.1 in order to show whether a random distribution or short-range correlations are present in the investigated networks. The theoretical section focuses on simulating the observed polymers P-N<sub>0</sub> and P-N<sub>3</sub> and compare them with the structures observed in the experiment.

### 2.2.1 Experimental Results

A typical Au(111) surface covered by organic polymers is shown in figure 2.3. It represents the P-N<sub>0</sub> system, however similar coverages and structural morphologies on Au(111) can be achieved for P-N<sub>3</sub>. The network with its pores and  $\alpha\beta\gamma$  triplets is visualized by STM. The inserts in figure 2.3 show an enlargement of a hexagonal pore with an overlay of the chemical structure (top right corner). The enlargement in the lower right corner shows an  $\alpha\beta\gamma$  triplet that involves exemplarily a pentagon, a hexagon and a heptagon.

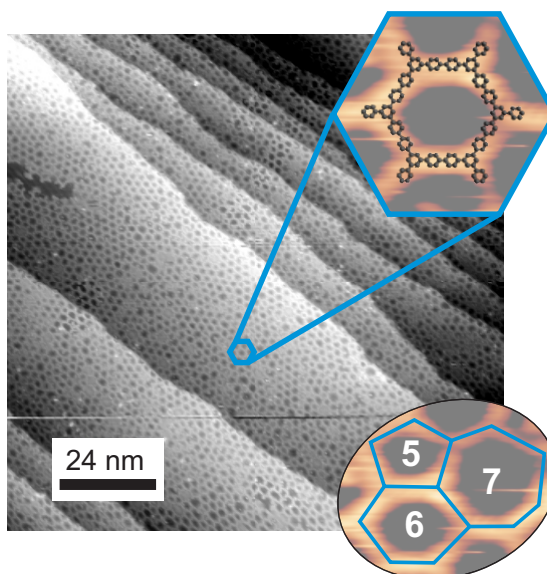


Figure 2.3 – STM topograph of the organic P-N<sub>0</sub> network ( $U = -1.3$  V,  $I = 30$  pA); Inserts: Zoom into a hexagonal pore with superimposed chemical structure and a representation of an  $\alpha\beta\gamma$  cluster involving a pentagon, hexagon and a heptagon.

From a structural perspective, one can expect an optimized structure of only hexagons. Like in graphene the carbon and nitrogen atoms of the investigated polymers have a  $sp^2$  hybridization, which favors the  $120^\circ$  angle between covalent bonds, due to the structure of the molecular orbitals. However, such an ordered structure is not observed and both polymer networks resolve an amorphous 2D structure. Similar results have been observed by other groups who show the disordered structure of P-N<sub>0</sub> by STM [103, 104, 105]. Magnifying both organic structures reveals the amorphous networks in more detail. Most molecules contribute up to three polygons, due to the trigonal symmetry of the precursor molecules. However, molecules can appear that are not bound to other molecules and terminate the molecular chain within the network. This phenomenon is not part of this work and has been investigated in another work [106]. Figure 2.4 (a) and (b) show how STM images were analyzed due to the ring size distribution. The network of P-N<sub>0</sub> is shown in figure 2.4 (a) and the structure of P-N<sub>3</sub> is illustrated in figure 2.4 (b). Both images have an overlay of colored polygons added, to distinguish between different ring sizes. Figure 2.4 (c) shows the ring size histograms for P-N<sub>0</sub> and figure 2.4 (d) shows the histograms for P-N<sub>3</sub>. Although hexagons are the dominant

structure followed by pentagons, the relative amount of pentagons is much lower within the P–N<sub>3</sub> network. Furthermore, four- and nine-membered rings occur only in the P–N<sub>0</sub> structure. They are absent within the P–N<sub>3</sub> system.

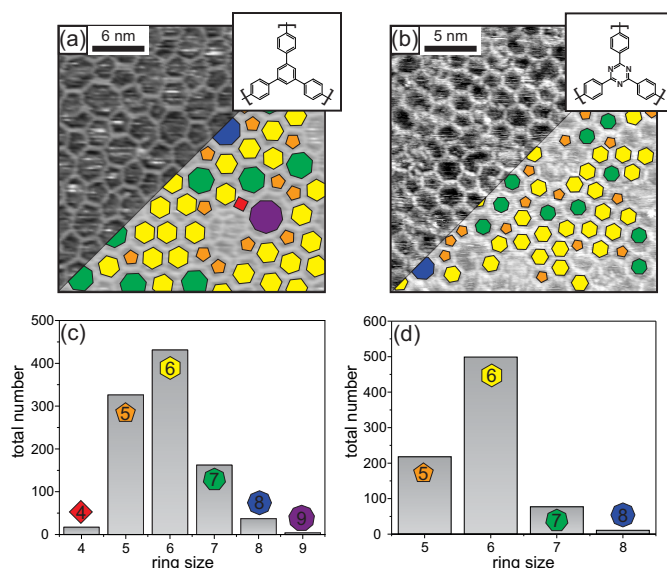


Figure 2.4 – (a) STM topograph of P–N<sub>0</sub> ( $U = -1.0$  V,  $I = 70$  pA) with overlaid colored polygons, (b) STM topograph of P–N<sub>3</sub> ( $U = -1.2$  V,  $I = 20$  pA) with overlaid colored polygons, (c) ring size distribution of P–N<sub>0</sub>, (d) ring size distribution of P–N<sub>3</sub>.

As mentioned above, the analysis of  $\alpha\beta\gamma$  clusters in the structure provides further knowledge about the short-range arrangement of the amorphous organic networks. A detailed explanation of the triplet notation was introduced in the previous section and is used in figure 2.5 to compare experimental triplet histograms with calculated histograms according to equation 2.1. Figure 2.5 (a) shows the  $\alpha\beta\gamma$  triplet distribution that were counted in STM images in dark orange and the expected distribution calculated by equation 2.1 in light orange. Remarkable differences can be observed in the 555 and 566 triplets, which are less existent in the experimental structure than expected by the calculation. Other mismatches can be found in the comparison of 567, 666 and 667 triplets, which appear more frequently in the experimental network than in the calculation of equation 2.1. Figure 2.5 (b) shows the analogue histograms of the P–N<sub>3</sub> system. The experimentally counted  $\alpha\beta\gamma$  clusters are shown in dark blue, while the distribution of modeled triplets are visualized in light blue. The major differences are found in 556, 566 and 666 triplets. The expected values are much higher for 556 and 566 triplets. In contrast, the network recorded in STM revealed a higher abundance of 567 and 666 clusters.

Both networks do not fully correlate with the modeled  $\alpha\beta\gamma$  distribution of equation 2.1, which yields a triplet distribution for a random tessellation with polygons derived from the histograms in figure 2.4 (c) and (d). Therefore, the cluster distribution is not entirely random and seems to exhibit certain correlations within the polymer structures.

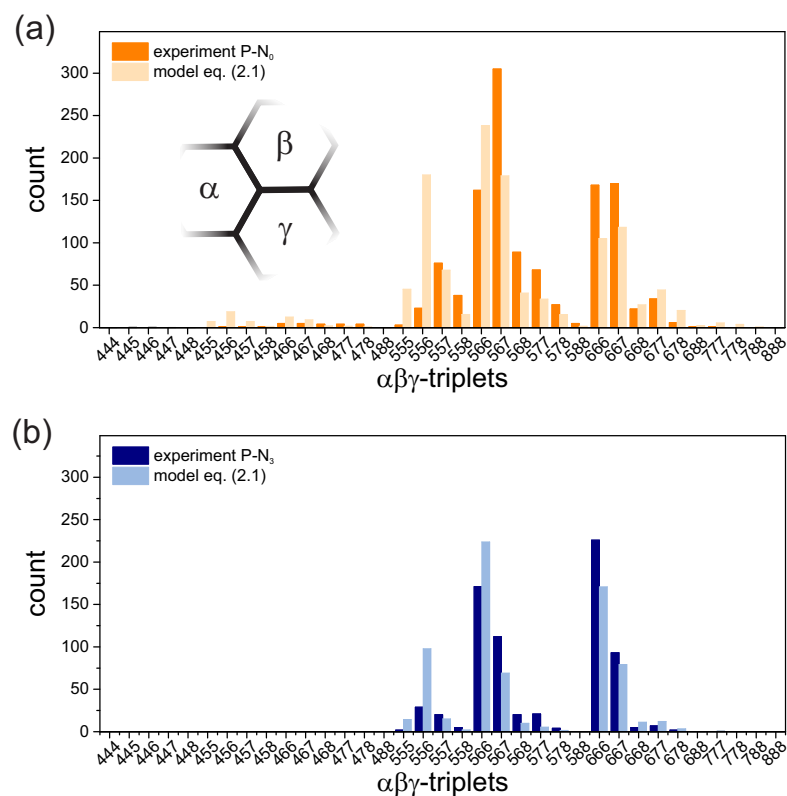


Figure 2.5 – Calculated amorphous network in variable periodic simulation cell after an MD-simulation of 220 ps: (a) Expected distribution (light orange) and experimental distribution (orange) in  $P-N_0$ ; (b) Expected distribution (light blue) and experimental distribution (blue) in  $P-N_3$ .

### 2.2.2 Theoretical Results

To mimic the real organic structure of the polymers, many different MD runs with different potentials have been performed and the ones have been chosen that show the best match in pore size and  $\alpha\beta\gamma$  triplet distribution. Figure 2.6 (a) illustrates an MD simulation of an amorphous network that contains 5750 molecules. The structure was produced in 220 ps during the MD simulation. Similarities to the STM image shown in figure 2.3 are reproduced in the overall homogeneity of the network with missing crystallinity. The MD simulation shows different pore sizes and areas where the structure terminates, which results in many unpolymerized endings inside the structure. Figure 2.6 (b) illustrates an enlargement of the simulated structure, showing that the appearing polygons (like hexagons and pentagons) exhibit a rather irregular shape and do not appear in a perfect symmetrical conformation, which is in good agreement with the experimental STM topographs.

In addition to the structural characteristics, MD simulations deliver an overview of the time evolution of the organic networks: Figure 2.7 shows MD simulations of the ring size distribution and the evolution of  $\alpha\beta\gamma$  triplets as a function of time. The development of the ring size distribution is shown in figure 2.7 (a) for  $P-N_0$  and in figure 2.7 (c) for  $P-N_3$ . The total amount

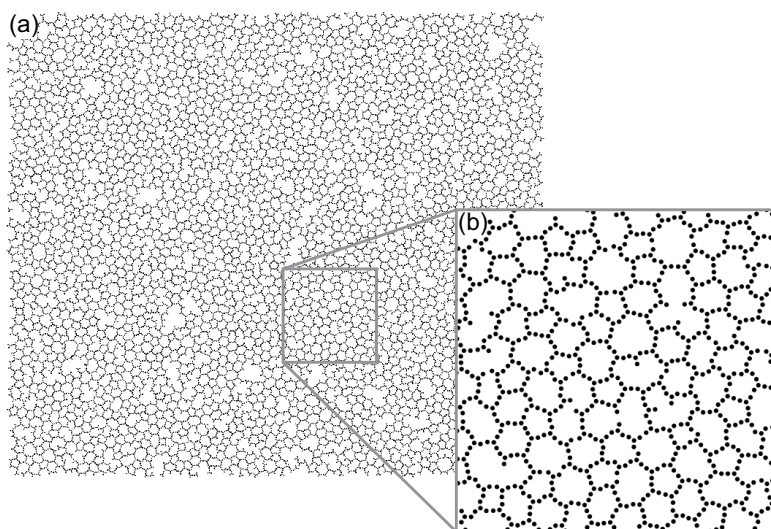


Figure 2.6 – Calculated amorphous network in variable periodic simulation cell after an MD-simulation of 220 ps: (a) Amorphous network of 5750 molecules; (b) Enlargement showing details in pore size distribution and terminated endings within the structure.

of rings increases for both systems over the simulated time period. However, the amount of four and eight-membered rings decreases, while the amount of five, six and seven-membered rings increases with their ratio staying relatively constant during time. The most abundant ring sizes in both systems are five and six-membered ring followed by seven-membered rings. Four and eight-membered rings appear less frequently and are more abundant in the early stage of polymer formation. In the following stages they are replaced by five, six and seven-membered rings. The main difference between the two MD simulations of  $P-N_0$  and  $P-N_3$  is the amount of pentagons. They show a much higher abundance in  $P-N_0$  than in the  $P-N_3$  simulation. Since the amount of seven- and eight membered rings is relatively similar in both systems, the amount of hexagons is slightly higher in  $P-N_3$  than in  $P-N_0$  to compensate the lower amount of pentagons. Another difference between the two investigated structures can be observed in the development of four-membered rings: The early stage of the  $P-N_0$  simulation shows a much higher amount of four-membered rings than the simulation of  $P-N_3$ . Although both structures show a reduction in four-membered rings, they vanish almost entirely in the simulation of the  $P-N_3$  system.

The time evolution of the near-range order is shown by the simulation of  $\alpha\beta\gamma$  triplets at certain time steps. Figure 2.7 (b) represents the histograms of  $P-N_0$  and figure 2.7 (d) shows the histograms of  $P-N_3$ . Both figures show the triplet distribution at 20 ps (grey), 120 ps (orange) and 220 ps (blue). Like the number of rings, the amount of  $\alpha\beta\gamma$  triplets increases over time. There are only little changes between 120 ps and 220 ps. Significant formation processes occur during the first 100 ps. In both systems the 567 triplet appears as dominant configuration during the entire formation process. The  $P-N_0$  simulation shows additionally a high abundance of 566 and 568 clusters alongside of 666 and 667 triplets. In  $P-N_3$ , the amount of 566 clusters is in a similar range than in  $P-N_0$ . However, a remarkable difference can be



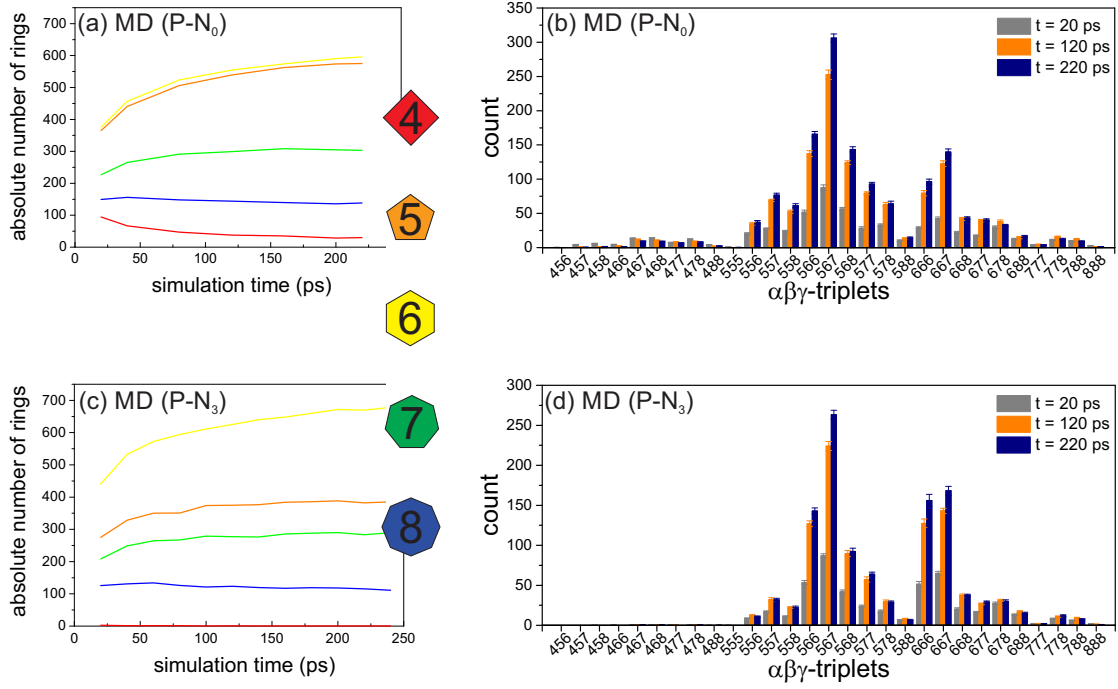


Figure 2.7 – Time evolution of ring formation and triplet distribution (averaged over 15 configurations): (a) Ring size distribution as a function of time for P–N<sub>0</sub>, (b) Distribution of  $\alpha\beta\gamma$  triplets over time for P–N<sub>0</sub>, (c) Ring size distribution as a function of time for P–N<sub>3</sub>, (d) Distribution of  $\alpha\beta\gamma$  triplets over time for P–N<sub>3</sub>.

observed in the number of 666 and 667 clusters, which have a larger abundance in the P–N<sub>3</sub> simulation. The behavior of the 568 cluster is vice versa. Its appearance is less frequently in P–N<sub>3</sub> than in P–N<sub>0</sub>.

In addition to the the time stages of  $\alpha\beta\gamma$  clusters in figure 2.7 (b) and (d), the potential energy as function of the logarithmic time is shown in figure 2.8. After an initial settling time of 20 ps, both systems decrease the potential energy at a constant rate on the logarithmic time scale, which is a typical behavior of amorphous systems [107]. The orange graph in figure 2.8 (a) shows the simulation of P–N<sub>0</sub> and the blue graph in figure 2.8 (b) illustrates the calculation of P–N<sub>3</sub>. The tilted dashed lines in both figures represent an extrapolation of the amorphous systems towards the equilibrium. In addition, the simulation of a perfect hexagonal lattice (black solid curve), which represents the ground state (crystalline structure) is added in both figures. The energy of the crystalline state fluctuates around a constant value, since the energy of the system cannot be further reduced. The horizontal dashed line in both figures represent the average potential energy of the ideal hexagonal lattice. The crossing of horizontal and tilted dashed lines indicates the point, when the polymer systems reach the thermodynamic equilibrium and the all the rings within their structure are rearranged into hexagons. Figure 2.8 (a) and (b) show clearly that neither P–N<sub>0</sub> nor P–N<sub>3</sub> reach the thermodynamic equilibrium during the simulation time and are in a state of marginal ergodicity [108, 109]. The simulation times need to be increased by four to six orders of

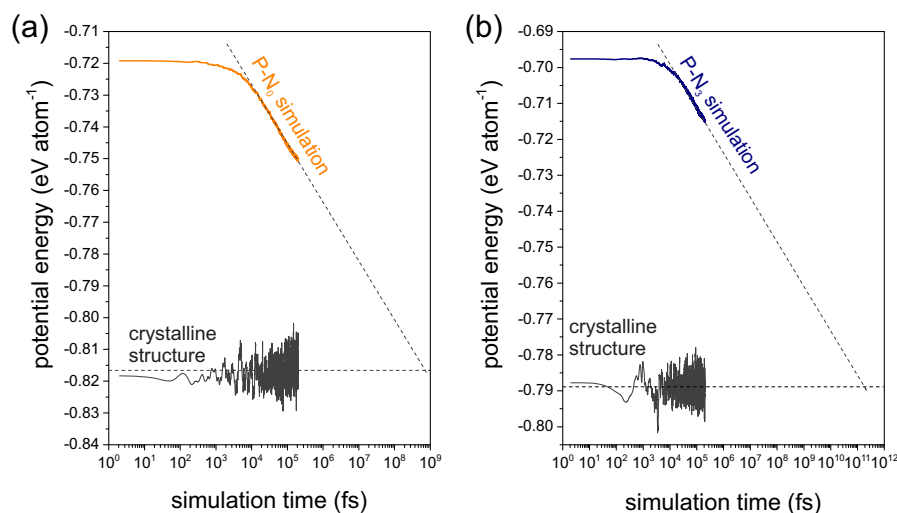


Figure 2.8 – Illustration of the potential energy per atom on a logarithmic time scale in the investigated polymer structures compared with the ground state of the system (hexagonal lattice): (a) Simulation of the P-N<sub>0</sub> system; (b) Simulation of the P-N<sub>3</sub> system.

magnitude in order to reach the ground state during the simulation. Despite of the rather long simulation times that were chosen, the relative ring size and cluster distribution remain far from the thermodynamic equilibrium. However both structures keep evolving and aging process are expected to appear on exponentially slow time scales [110].

## 2.3 Discussion on Structural Short-Range Correlations

The characterization of short-range correlations in organic 2D porous networks requires the combination of experiment and theory. If the potential in MD calculations varies, the resulting simulated structure will have a different pore size distribution. The performed simulations use AB<sub>3</sub> building blocks that were introduced in the previous section (see fig. 2.1 b). The interactions between neighboring AB<sub>3</sub> units are described by A-A-A and B-B-A interactions. MD simulations show that the total amount of rings and their pore size changes with the energy parameter  $b_{ijk}$ , which has interactions of A-A-A and B-B-A implemented. MD simulations show a large amount of rings, which are predominantly pentagons and hexagons, if small values for the A-A-A component in the  $b_{ijk}$  energy parameter are chosen. If the A-A-A interactions are increased, the resulting simulation will reveal a larger abundance of hexagons. Pentagons are represented less frequently in such simulations. It has to be mentioned that B-B-A interactions are also considered in the  $b_{ijk}$  energy parameter, however the overall contribution is dominated by A-A-A interactions. A detailed explanation of the theoretical model is published in reference [2]. Embracing both simulations (small and large A-A-A interactions) and combine them with the ring size statistics in figure 2.4 (c) and (d), the calculation that reveals small A-A-A interactions can be assigned to the P-N<sub>0</sub> network, due to the high amount of pentagons and hexagons. MD simulations with large A-A-A interactions

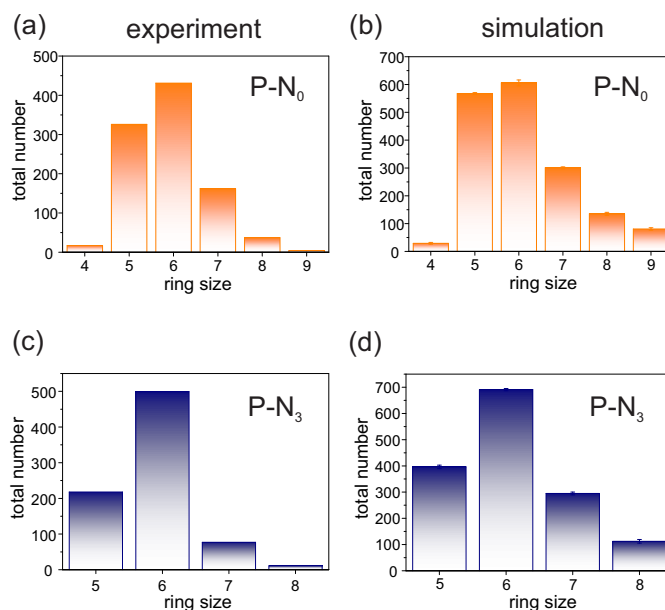


Figure 2.9 – Experimental and simulated histograms of the ring size distribution: (a) Experimental P–N<sub>0</sub> ring size distribution; (b) Simulated P–N<sub>0</sub> ring size distribution; (c) Experimental P–N<sub>3</sub> ring size distribution; (d) Simulated P–N<sub>3</sub> ring size distribution.

are used as a representation of the P–N<sub>3</sub> polymer, since they expose hexagons as dominant ring size configuration.

The ring size statistics of experiment and theory is summarized in figure 2.9 for both investigated systems. Figure 2.9 (a) and (b) show the experimental and simulated ring size distribution of the P–N<sub>0</sub> network. Both histograms reveal hexagons as the dominant ring size and experiment and theory are in good agreement. Slight deviations can be observed regarding five- and nine-membered rings, which are less abundant in the experimental structure than suggested by the simulation. Adjusting the ratio of pentagons and hexagons in the P–N<sub>0</sub> simulation can be performed by increasing the  $b_{ijk}$  energy parameter of A–A–A and B–B–A interactions. Increasing the energy of A–A–A interactions results in a lower abundance of five-membered rings and leads to an equal relative amount of five- and seven-membered rings. If B–B–A interactions are increased, the number of four-membered rings is drastically diminished. The overall best simulation is presented in figure 2.9 (b). For achieving further improvements in the conformity between experiment and simulation, more investigations have to be performed. Figure 2.9 (c) and (d) illustrate the experimental and simulated ring size distribution of the P–N<sub>3</sub> system. Despite of slightly higher amounts of five-, six- and eight-membered rings within the calculated histogram, experimental and simulated ring size distribution accord well with each other. Further changes of the P–N<sub>3</sub> simulation can only be performed by the  $b_{ijk}$  energy parameter of B–B–A interaction, since the A–A–A energy is already set to a high value. However such changes are not advisable, since they result in a drastic decrease in pentagons until they vanish entirely, which is not in agreement with the experimental statistics.

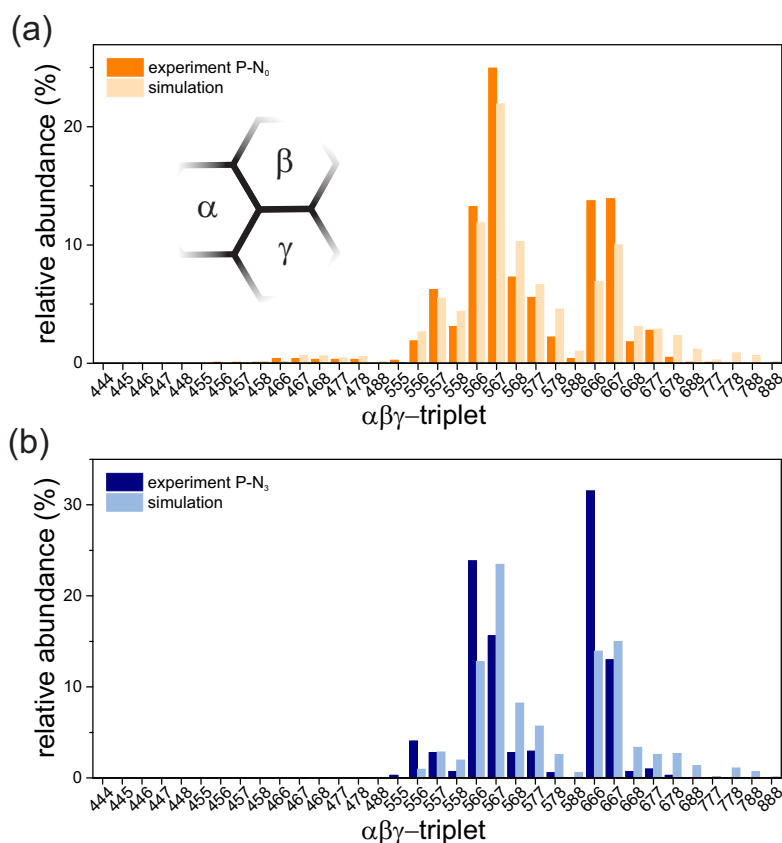


Figure 2.10 – Experimental and theoretical distribution of  $\alpha\beta\gamma$  triplets: (a) Simulated (light orange) and experimental (orange)  $\alpha\beta\gamma$  triplet distribution of  $P-N_0$ ; (b) Simulated (light blue) and experimental (blue)  $\alpha\beta\gamma$  triplet distribution of  $P-N_3$ .

The second applied metric to describe short-range correlations within the investigated polymer networks is the comparison of  $\alpha\beta\gamma$  clusters. Experimental data from figure 2.5 are plotted together with the results of the MD simulations of  $P-N_0$  and  $P-N_3$  in figure 2.10. The histogram in figure 2.10 (a) displays the comparison between experiment and simulation of the  $P-N_0$  network. Differences can be observed in the 666 and 667 triplet, which show a higher appearance in the experimental structure than in the simulation. Apart from such discrepancies experiment and simulation are in good agreement, which can be observed in the large number of 567 triplets or the almost entire absence of 555 clusters. In figure 2.5 (a) the expected and the experimentally observed distribution of  $\alpha\beta\gamma$  clusters revealed a poor conformity for  $P-N_0$ . As mentioned in the previous section 555, 556 and 566 triplets were less abundant in the experimental structure than in the calculation according to equation 2.1. Furthermore triplets like 567, 666 and 667 have a higher number in the real structure than expected. The reason for this phenomenon is the large strain, which is necessary to form 555 clusters in the polymer. To force such a cluster into a planar shape on the surface requires energy for straining bonds and angles. A 666 triplet has a rather flat shape and less energy is needed to enable planarity. Additionally a seven-membered ring can compensate the stress of five-membered rings in the network, which is the reason for the high abundance of 567

## 2.3. Discussion on Structural Short-Range Correlations

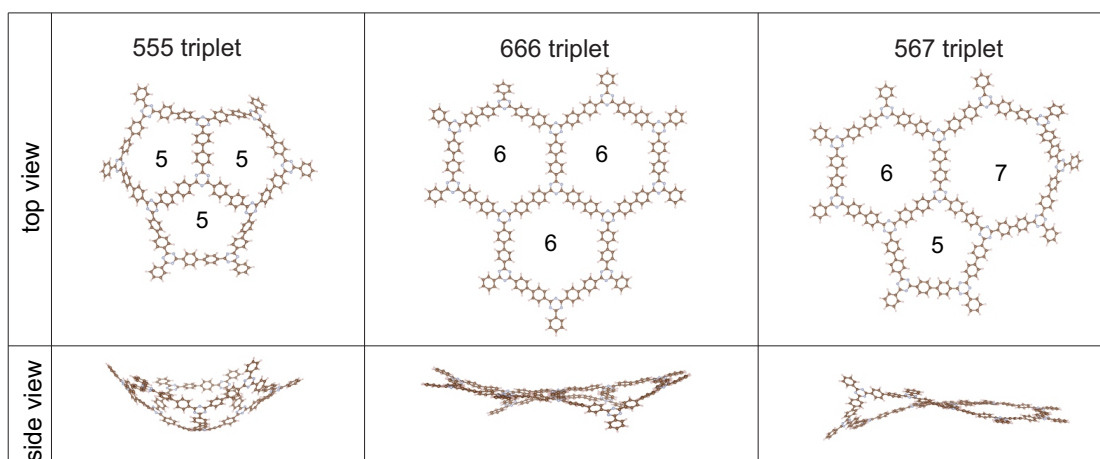


Figure 2.11 – Top and side view of 555, 666 and 567 triplets showing the different levels of planarity within the clusters.

clusters in the experimental network. These arguments are supported by quantum-chemical calculations (Hartree-Fock calculation) and explain the improved similarity of the histograms in figure 2.10 (a). In  $P-N_0$  the calculated formation energy per molecule is lowest for 666 triplets and slightly higher for 567 triplets, which need 15 % more energy. Cluster formation of 555 triplets is even higher and requires 30 % more energy compared to 666 clusters. The reason for the high formation energy in 555 triplets is the large strain within the clusters. Figure 2.11 shows the top view for 555, 666, 567 triplets and their corresponding side view: The connection of three pentagons results in a buckling of the final cluster and the structure has no planar configuration, which is shown in sideview of 555 triplets in figure 2.11. The structural buckling in 666 and 567 clusters is less dominant (666 and 567 triplets in fig. 2.11) and is entirely smoothed by van-der Waals interaction with the gold substrate. Due to the geometry of 555 triplets, flattening is energetically more expensive and thus appears rarely on the investigated samples. The difference between expectation (fig. 2.5) and MD simulation (fig. 2.10) is the result of short-range correlation in the polymer network. This correlation is not encoded in the MD model and the simulation cannot fully replicate the experimental results. Small pores (smaller than six-membered rings) appear in the presence of large pores (larger than six-membered rings) to decrease mechanical stress and ensure a smooth shape of the polymer. Therefore, the ring size distribution in  $P-N_0$  is not random and follows recurrent structural motifs that are accompanied with particular  $\alpha\beta\gamma$  clusters. In order to minimize internal stress inside the polymer certain  $\alpha\beta\gamma$  triplet combinations are energetically more favorable and decrease the stress in the overall polymer network.

Figure 2.10 (b) illustrates  $\alpha\beta\gamma$  triplets in  $P-N_3$ . Although the ring size distribution, which is shown in figure 2.9 (b) matches well between experiment and simulation, the agreement in the distribution of  $\alpha\beta\gamma$  triplets is less good for  $P-N_3$ . The experimental structure reveals a much higher amount of 566 and 666 triplets than the corresponding simulation predicts. The mismatch is also remarkable for the 567, 568 and 577 triplets that have a larger abundance in

the calculated histograms. Especially the large number of 666 clusters leads to the assumption that the experimental network is closer to the hexagonal lattice, which represents the energetic minimum. In consequence, the network recorded in STM is closer to the thermodynamic equilibrium than the simulation.

A possible explanation are the simulation times that are too short for the system to evolve towards the equilibrium. It was shown in the previous section that both investigated systems are far away from the thermodynamic equilibrium (fig. 2.8). Although the potential energy decreases constantly, the time scales are exponentially slow and the P-N<sub>3</sub> simulation requires more time to form a larger number of hexagons within the structure. Simulations are expected to run 4-6 orders of magnitude longer in order to reach the optimal hexagonal lattice, which is presumably the ground state. The development of P-N<sub>3</sub> towards a high number of six-membered rings can be observed in figure 2.10 (c) and (d): The relative number of hexagons increases during time, while the number of smaller rings stays relatively constant or even decreases. Such aging processes decrease the energy by restructuring the amorphous network [110] and evolve it closer to a crystalline structure. Alongside the reordering of pores goes the realignment of  $\alpha\beta\gamma$  clusters (fig. 2.10 d) that evolve towards a distribution of low cluster energy. Consequently, if the simulation time is increased, the P-N<sub>3</sub> simulation will rearrange its structure and show more similarities to the experimental P-N<sub>3</sub> network. However, it is very likely that the thermodynamic minimum will not be reached during the simulation, even at very high simulation times. Additionally, it can be expected that the corresponding experimental structure will continuously change the pore size configuration and evolve closer to the hexagonal lattice. Like the simulation, such investigations require very long time scales, which make experimental studies challenging.

It has to be mentioned that the P-N<sub>3</sub> calculation is significantly different for our applied simulation times and reveals more similarities to the mean-field model provided by equation 2.1. Hardtree-Fock calculations show that certain  $\alpha\beta\gamma$  clusters of P-N<sub>3</sub> require less energy to be implemented in the network compared to P-N<sub>0</sub>. Origin of this phenomenon is the triazine component in the precursor molecules of P-N<sub>3</sub>. It has less hydrogen atoms in its structure than the precursor molecule of P-N<sub>0</sub>, which has benzene as central component (see fig. 2.1 a). Therefore the hydrogen/hydrogen interactions between cyclic neighboring compounds are diminished in P-N<sub>3</sub> and mosaic ring size configurations are more likely to form, since they are not limited by energetic barriers that hinder mosaicity in P-N<sub>0</sub> networks. As a result planarity of the overall P-N<sub>3</sub> network can be enforced with less energy compared to P-N<sub>0</sub>. In consequence structural defects can be implemented in P-N<sub>3</sub> at lower energy costs and will converge the  $\alpha\beta\gamma$  cluster distribution closer to the expected distribution in figure 2.5. This shows that the correlations that have been observed in the P-N<sub>0</sub> network are not present in P-N<sub>3</sub>, due to different energies that are necessary to provide planarity of the overall network, which makes the chemical composition and the design of precursor molecules a critical factor for tuning spatial correlations in polymer networks.

## 2.4 Conclusion

The ring size distribution of two different amorphous polymers P-N<sub>0</sub> and P-N<sub>3</sub> has been investigated in this chapter. Therefore manual analysis of large-area STM images and MD simulations have been used. The particular strength of this work is the combination of pore size distribution analysis with the relative abundance of  $\alpha\beta\gamma$  triplets that describe the local environment of the amorphous glassy polymers. By changing the specific energy parameter ( $b_{ijk}$ ), we can propose design principles that specifically stiffen A-A-A or B-B-A interactions in simulated building units and can account for different ring size distributions. The ring size distribution of the P-N<sub>0</sub> network shows a good agreement between experiment and theory. In addition, the distribution of  $\alpha\beta\gamma$  clusters reveals overall similarities showing that the performed simulations were able to mimic the experimental structures successfully. The results show spatial correlations on short length scales in P-N<sub>0</sub>, determined by energy penalties that arise in random structures and follow a mean-field model. In order to guarantee a planar network certain  $\alpha\beta\gamma$  triplets are favored and require less energy to be implemented in the structure of P-N<sub>0</sub>.

The differences between P-N<sub>0</sub> and P-N<sub>3</sub> are nitrogen atoms within the triazine component of the precursor molecules. Therefore P-N<sub>3</sub> does not show short-range correlations like P-N<sub>0</sub> and the formation of defects can occur at lower energy penalties. Nitrogen atoms substitute C-H within triazine and make the network of P-N<sub>3</sub> less susceptible to steric clashes caused by hydrogen interactions. The result is a polymer network that shows a higher defect tolerance and favors the formation of mosaic structures that tessellate in a random manner on the surface. Moreover this facilitates aging processes of the P-N<sub>3</sub> polymer, which have to be incorporated in future simulations of similar amorphous structures to avoid a remarkable mismatch between experiment and theory.

Although the investigation of the two analyzed polymers was given in this chapter, further studies are necessary to understand the growth kinetics of 2D amorphous polymers entirely. Changing the precursor molecule that acts as repeat unit within such networks is a first step. Implementing bulky functional groups can hinder the growth of certain ring sizes and provide a specific selectivity within pore size distributions. Another aspect that is not considered in this work is the influence of step edges. Metals that act as substrates for molecule deposition are never atomically flat. The role of step edges need to be implemented in experiments and in simulations. At last, it would be of particular interest to study the distribution of pore sizes and  $\alpha\beta\gamma$  triplets over long time scales. Storing prepared samples for extended amounts of time may shift to a distribution that is dominated by hexagons and even crystalline subregion may be observable.





### 3 Enhancing HER through Molecular Engineering<sup>1</sup>

After the introduction of the statistics in organic polymer networks on Au(111) in the previous chapter, these devices are used for electrocatalysis and will be tested for their activity towards the hydrogen evolution reaction (HER). Hydrogen evolution is a half reaction (reduction) of water splitting, which produces molecular hydrogen. This process converts electrical energy to chemical energy, which is stored within the hydrogen gas and becomes accessible in fuel cells. The advantage of such energy-dense fuels is their easy storage and transport capability. On the route towards cheap and efficient electrocatalytic water splitting catalysts, the replacement of platinum group metals as catalysts for the hydrogen evolution half-cell reaction is a primary milestone [4]. Therefore, it is desirable to achieve a deeper understanding of the reaction steps of HER on the nanoscale. The rate limiting step in alkaline media often seems to be the splitting of the HO–H bond during the Volmer step, which precedes in the adsorption of hydrogen. One possible approach is to modify the electrode surface to stabilize water close to the electrode surface by hydrogen bonding [111, 112].

Elaborating on this concept, the following chapter introduces molecular engineering to pattern well-defined electrode surfaces. Gold electrodes are combined with organic polymer co-catalysts, which are tunable in their chemical structure with the aim to increase the HER activity at pH 13. The 2D porous single-layer polymer is structurally similar to organic sheets within 2D covalent organic frameworks (COFs) that have been recently emerged as active photocatalysts for hydrogen production [37, 113, 114]. The light can be efficiently absorbed by the COFs, as a result of suitable band gaps. On single-crystal substrates similar single-layer polymers can be fabricated that cover the entire electrode [49, 115, 116]. Such methods deliver well defined chemical structures with hydrogen bonding sites. The combination of metal substrate and organic polymer co-catalyst results in a hybrid electrode that improves the binding strength of the reactants at the gold surface, which in consequence increases the HER activity. The complete chapter is based on reference [3].

---

<sup>1</sup>This chapter and the presented results are based on ref. [3]

### 3.1 Preparation of the Electrode Surfaces

Prior to the polymer synthesis, the Au(111) crystal was cleaned by several  $\text{Ar}^+$ -sputtering and annealing (825 K) cycles in an UHV preparation chamber with a base pressure  $< 5 \times 10^{-10}$  mbar. The porous 2D polymers were synthesized through sublimation of brominated precursor molecules – 1,3,5-tris-(4-bromophenyl)-benzene ( $\text{N}_0$ ), 2,4,6-tris-(4-bromophenyl)-1,3,5-triazine ( $\text{N}_3$ ), and 2,2',2''-(benzene-1,3,5-triyl)-tris-(5-bromopyrimidine) ( $\text{N}_6$ ) – from a quartz crucible. Polymerization of the precursor molecules follows an Ullmann-like coupling pathway [88, 89, 90, 91, 92], which means the reactants debrominate and form covalent bonds between the aryl-rings building up the polymers  $\text{P-N}_0$ ,  $\text{P-N}_3$ , and  $\text{P-N}_6$ . Sublimation temperatures were 475 K for  $\text{N}_0$  and 515 K for  $\text{N}_3$ , and 515 K for  $\text{N}_6$ , while the Au substrate was held at 565 K. The resulting 2D network exhibits an amorphous network, which has been discussed in detail in the previous chapter. The abbreviation  $\text{N}_0$ ,  $\text{N}_3$ , and  $\text{N}_6$  represent the amount of nitrogen atoms within the precursor molecules, while  $\text{P-N}_0$ ,  $\text{P-N}_3$ , and  $\text{P-N}_6$  indicate the polymer structures. Figure 3.1 (a) shows schematically the polymerization reaction under the release of bromine.  $\text{P-N}_0$  is composed purely of carbon and hydrogen, while  $\text{P-N}_3$  has additionally nitrogen within the triazen rings that are located in the vertices of the network (fig 3.1 (a) position X).  $\text{P-N}_6$  has nitrogen heteroatoms in pyrimidine groups and has three times the amount of nitrogen compared to  $\text{P-N}_3$ . The void pores reveal the underlying bare Au(111) substrate leaving it accessible to the electrolyte. Figure 3.1 (b) shows a STM topograph of the  $\text{P-N}_3$  system and its typical amorphous porous structure. It includes an enlargement of a hexagonal pore that is build up of six  $\text{N}_3$  precursor molecules.

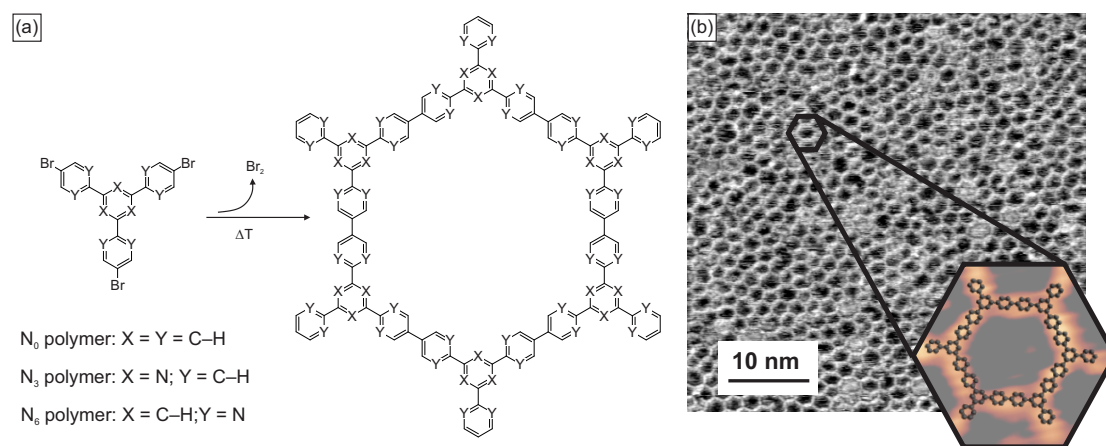


Figure 3.1 – Tuneable 2D polymer for electrocatalytic hydrogen evolution: (a) Schematic illustration of the Ullman-like polymerization reaction of the precursor molecules  $\text{N}_0$  ( $\text{X} = \text{C-H}$ ),  $\text{N}_3$  ( $\text{X} = \text{N}$ ,  $\text{Y} = \text{C-H}$ ) and  $\text{N}_6$  ( $\text{X} = \text{C-H}$ ,  $\text{Y} = \text{N}$ ); (b) STM image ( $U = -1.2$  V,  $I = 30$  pA) of the  $\text{P-N}_3$  polymer as an example of the polymerized structure, including a single pore with a schematic overlay of the chemical structure.

### 3.2 HER with Hybrid Electrodes

Before the hybrid electrodes are tested as electrocatalysts for hydrogen evolution, the surface roughness is examined. A surface with a high roughness factor provides more active sites and larger access to reactants during catalysis, which is embraced in the electrochemical active surface area (ECSA). Determining the ECSA of the hybrid electrodes and blank Au(111) shows, whether the organic polymer affects the surface roughness and changes the ECSA. In the following, the protocol of reference [117] is used to calculate the ECSA of the hybrid electrode with the P-N<sub>3</sub> co-catalyst. It is compared with the ECSA of a blank Au(111) electrode to assure the flatness of hybrid electrodes and to exclude additional roughness caused by organic co-catalysts.

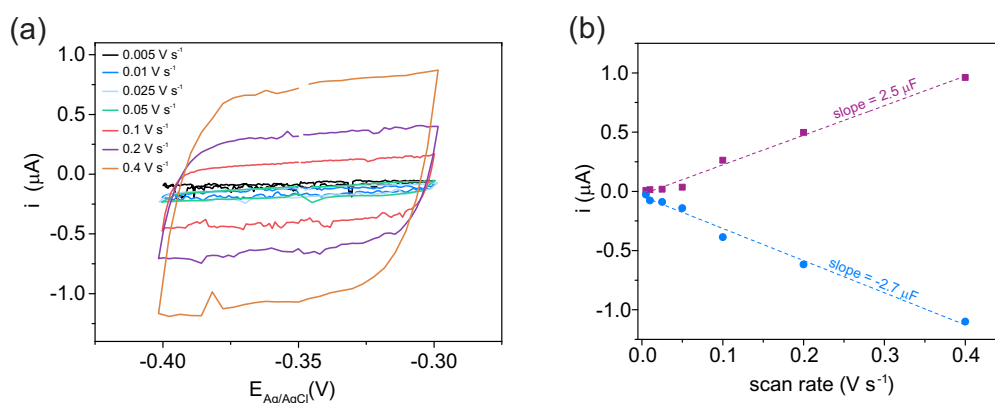


Figure 3.2 – Double-layer capacitance measurement of the P-N<sub>3</sub> hybrid electrode: (a) Voltammetry in non-Faradaic region at different scan rates in 0.1 M NaOH: 0.005 (black), 0.01 (blue), 0.025 (light blue), 0.05 (green), 0.1 (red), 0.2 (purple) and 0.4  $\text{V s}^{-1}$  (yellow); (b) Anodic (purple) and cathodic (blue) charging currents as function of the scan rate with the slope representing the double layer capacitance.

The ECSA was determined by the electrochemical double-layer capacitance, measured by voltammetry in the non-Faradaic region [117, 118]. Figure 3.2 (a) shows the recorded cyclic voltammograms with six different scan rates of the P-N<sub>3</sub> hybrid electrode. The maximum potential range of 0.1 V vs. Ag/AgCl is centered around the open circuit potential. It is assumed that the measured current originates exclusively from double layer charging and no Faradaic contributions are existent in this region. This allows to formulate the linear relation between the double layer charging current  $i_c$  and the scan rate  $\nu$  to determine the double layer capacitance  $C_{\text{DL}}$  according to equation 3.1 [117, 118, 119, 120]

$$i_c = \nu \cdot C_{\text{DL}}. \quad (3.1)$$

Applying this relation on the data points recorded in figure 3.2 (a), reveals the plot in figure 3.2 (b): The purple graph represents the anodic charging current as a function of the scan rate that were obtained at  $-0.3 \text{ V}_{\text{AgCl}}$  and the data points of the blue graph were obtained at  $-0.4 \text{ V}_{\text{AgCl}}$  representing the cathodic charging current of the double layer. The slope of both graphs

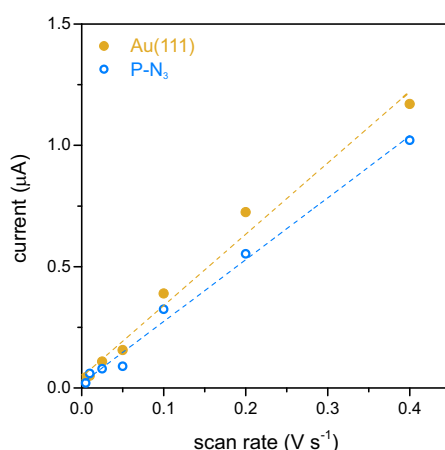


Figure 3.3 – Double layer current as a function of the scanrate with the capacitance as slope, allowing to estimate a similar ECSA of blank gold (yellow) and the P–N<sub>3</sub> decorated gold surface (blue).

gives the double layer capacitance  $C_{DL}$ , which is around  $2.6 \mu\text{F}$  for the hybrid electrode with the P–N<sub>3</sub> co-catalyst.

The double layer capacitance  $C_{DL}$  of a blank Au(111) electrode was characterized analogously and reaches a value of  $2.9 \mu\text{F}$ . The double layer capacitance of both electrodes are in the same range of magnitude and have been previously reported for gold [121, 122]. Figure 3.3 shows the double layer charging current of the P–N<sub>3</sub> hybrid catalyst (blue) and a blank Au(111) electrode (yellow). The slope of both graphs is almost identical, which implies similar capacitance values of both electrodes. This underlines the almost identical ECSA of Au(111) as well as the polymer decorated electrode surfaces and an increasing roughness factor of the organic co-catalysts can be neglected. The co-catalysts do not provide further access to reactants and the surface of the hybrid electrodes can be treated like a blank Au(111) surface as atomically flat.

Since it has been shown that the organic co-catalysts do not affect the surface roughness of Au(111), these devices are tested as electrocatalysts to improve their properties for the HER. The three different polymer-decorated electrodes exhibit characteristic signals in the cyclic voltammograms within a potential range from  $-0.70$  to  $-0.95 \text{ V}_{\text{Ag}/\text{AgCl}}$  and are illustrated in figure 3.4 (a). These peaks appear in the anodic and the cathodic scan of each voltammogram. The graph of P–N<sub>0</sub> is marked in green and appears at the highest overpotential of the investigated co-catalysts. Following the x-axis in figure 3.4 (a) towards more negative overpotentials, P–N<sub>3</sub> (blue) is the next signal that appears. The sequence in the cyclic voltammogram is finished by the peaks of P–N<sub>6</sub> (purple) that are observed at more negative overpotentials than P–N<sub>0</sub> and P–N<sub>3</sub>. Such features are not present on a bare Au(111) electrode. It has to be mentioned that the signal of P–N<sub>6</sub> is slightly stronger tilted compared to the signals of P–N<sub>0</sub> and P–N<sub>3</sub>. The reason for this minor increased slope in the cyclic voltammogram of P–N<sub>6</sub> is the IR-drop. While the current is passing through the electrolyte, the applied overpotential decreases stronger for P–N<sub>6</sub>, most likely of different mass transport conditions or a slightly larger distance between the electrodes. However, the IR-drop is insignificant in this observed

range and has no influence on the experiment and the upcoming discussion.

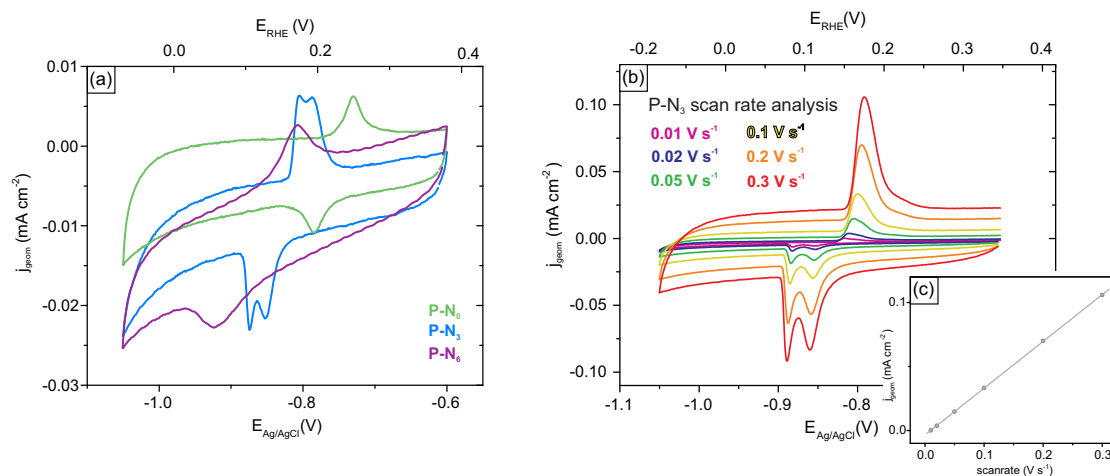


Figure 3.4 – Cyclic voltammograms for hybrid electrodes in 0.1 M Ar saturated NaOH solution prior to hydrogen evolution: (a) Cyclic voltammograms at 0.05 V s<sup>-1</sup> for P-N<sub>0</sub> (green), P-N<sub>3</sub> (blue) and P-N<sub>6</sub> (purple). (b) Scan-rate analysis of the EC signal, exemplary shown for P-N<sub>3</sub> (c) Current density vs. scan rate plot showing a linear relationship, exhibiting a faradaic process of the adsorbed polymer.

Exemplarily, P-N<sub>3</sub> on Au(111) has been investigated at six different scan rates (fig. 3.4 b): The peak current  $I_p$  and the capacitive current that is defined by the double layer increase with larger scan rates. Figure 3.4 (c) reveals a linear relation between peak current and scan rate, which suggests a redox process of the adsorbed polymer. The relation between scan rate and adsorbed redox couples on surfaces has been introduced in chapter 1 and is characterized by equation 1.8. It has to be mentioned that redox processes of ideal adsorbed species have no potential shift. Oxidation and reduction occur at the exact same potential. We also want to denote the possibility of bromine that is produced during polymerization. Bromine residues that remain on the surface can show a similar behavior according to adsorption and desorption [123]. However, this should occur at larger potentials and the peak height of the anodic adsorption signal should correlate linearly with the square root of the scan rate [124], while a linear scan rate dependence is observed in this work. These observations support the hypothesis of a redox process of the adsorbed polymer and go along with an increased HER activity.

The complete polarization curves are shown in figure 3.5 and exhibit different current densities for the polymers as a result of different HER activities. Bare Au(111) shows a current density of  $-0.16 \text{ mA cm}^{-2}$  at a potential of  $-1.3 \text{ V}_{Ag/AgCl}$ , while the presence of the P-N<sub>3</sub> increases this value more than three-fold to  $-0.55 \text{ mA cm}^{-2}$ . P-N<sub>0</sub> and P-N<sub>6</sub> reach both a current density of  $-0.27 \text{ mA cm}^{-2}$ , almost twice as large as Au(111). For comparison, the overpotentials vs. the reversible hydrogen electrode at  $-0.20 \text{ mA cm}^{-2}$  are  $-0.23 \text{ V}$  (P-N<sub>3</sub>),  $-0.29 \text{ V}$  (P-N<sub>0</sub>),  $-0.30 \text{ V}$  (P-N<sub>6</sub>), and  $-0.35 \text{ V}$  (gold).

In addition to the current density at a fixed overpotential, the onset potential can be used to evaluate electrocatalytic reactions. It is determined as the potential at which the first current

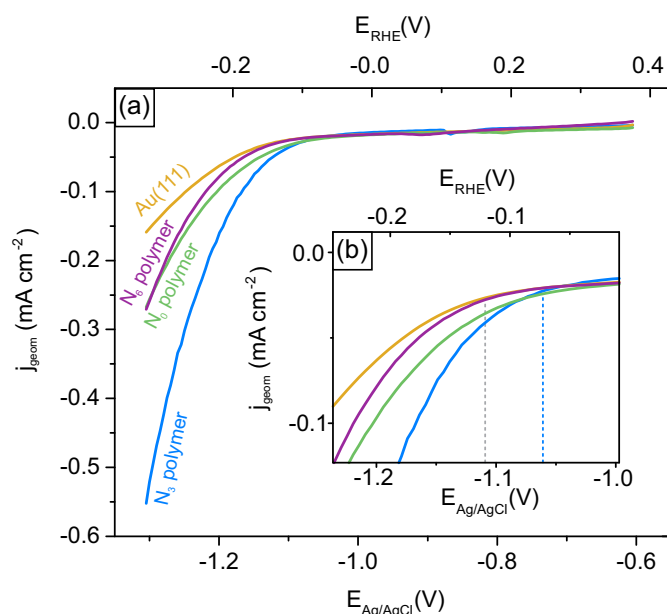


Figure 3.5 – HER on hybrid electrodes in Ar saturated 0.1 M NaOH solution at 0.05 V s<sup>-1</sup>: (a) Polarization curves of P–N<sub>0</sub> (green), P–N<sub>3</sub> (blue) and P–N<sub>6</sub> (purple); (b) Insert shows that P–N<sub>3</sub> requires a lower overpotential than Au(111), P–N<sub>0</sub> and P–N<sub>6</sub>.

flow is detected that is assigned to the investigated reaction (faradaic current). Identifying the exact point of the onset potential is not always straight forward and can imply certain imprecision. Although the concept of the onset potential is usually used for the ORR [20, 125], it emphasizes the different catalytic activities of the investigated co-catalysts. Figure 3.5 (b) is an enlargement of the polarization curves presented in figure 3.5 (a) showing the linear scans within a potential window from –1.0 to –1.25 V<sub>Ag/AgCl</sub>. The onset potentials of Au(111), P–N<sub>0</sub> and P–N<sub>6</sub> have a similar value of –1.12 V and are indicated by a grey dashed line. The onset of the P–N<sub>3</sub> co-catalyst exhibits a lower potential of –1.06 V (blue dashed line in figure 3.5 b), which underlines the importance of the P–N<sub>3</sub> co-catalyst for hydrogen evolution.

To ensure that the polymer is present during catalysis and does not decompose prior or during hydrogen evolution, X-ray photoelectron spectroscopy (XPS) was performed before and after catalysis of all three polymers. The following passage will present XPS data of the three polymers with typical STM data. The electrochemical experiment involves three polarization scans up to –1.2 V<sub>Ag/AgCl</sub> for all investigated hybrid electrodes. Figure 3.6 shows the characterization of the Au(111) electrode decorated with the P–N<sub>0</sub> network. The porous structure of the network prior to hydrogen evolution is illustrated in figure 3.6 (a). The corresponding discussion about the distribution of the pore size and ring size combinations are presented in the previous chapter. The spectrum in figure 3.6 (c) shows the XPS analysis of the C 1s core level prior to HER (orange spectrum), which is at 284.5 eV. Figure 3.6 (b) illustrates the surface after hydrogen evolution with the attendant XPS spectrum in figure 3.6 (c) (blue graph). The XPS spectrum after HER remains unaltered and exhibits the C 1s core level at 284 eV, which emphasizes the chemical integrity of the P–N<sub>0</sub> network under the

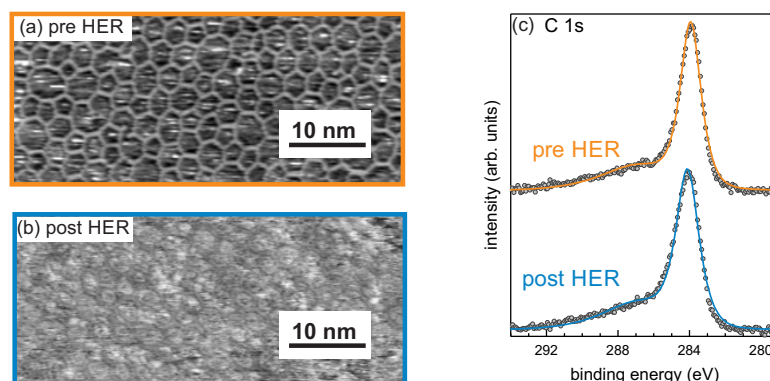


Figure 3.6 – STM and XPS on electrode, covered with P–N<sub>0</sub> before and after HER: (a) STM image recorded before HER ( $U = -1.0$  V,  $I = 74$  nA) and (b) after HER ( $U = -1.0$  V,  $I = 81$  nA) after 3 LSVs up to  $-1.2$  V<sub>Ag/AgCl</sub>. Porous polymer structure remains observable after HER. (c) XPS spectra of the C 1s core level before hydrogen evolution (orange) and after hydrogen evolution (blue). No major shifts can be observed indicating the chemical integrity of the polymer.

applied electrochemical conditions. Although the polymer-decorated electrode surface was always prepared precisely after HER and dried with argon air, residue remain on the surface, such as molecules of the electrolyte or milliQ water from the cleaning process. They act as impurities during STM and can interfere with the STM tip, resulting in the downgrade of the image resolution like it is observable in figure 3.6 (b). However, the network of the P–N<sub>0</sub> co-catalyst can be identified. The only difference to figure 3.6 (a) is the filling of the pores, which is presumably the mentioned residues of the electrolyte.

The P–N<sub>3</sub> network was investigated analogously. Figure 3.7 shows the corresponding characterization of the P–N<sub>3</sub> co-catalyst by STM and XPS before and after hydrogen evolution. The freshly prepared electrode is illustrated in figure 3.7 (a), showing the porous structure of the P–N<sub>3</sub> organic network. Isolated pores can appear to be filled up by single precursor molecules that did not polymerize during the coupling reaction. They remain as single monomers surrounded by the polymer network. After using the device as hybrid electrode for hydrogen evolution, the organic co-catalyst stays intact on the Au(111) surface, shown in figure 3.7 (b). The network shows no differences from the freshly prepared morphology, besides from filled pores, which are most likely residue from the electrolyte like in the P–N<sub>0</sub> network. The stability for the experimental conditions is also reflected by XPS. We performed three different XPS data sets of the C 1s signal shown in figure 3.7 (c) and the N 1s core levels shown in figure 3.7 (d). The first XPS data set is illustrated by the orange spectra (fig. 3.7 c and d) and reflects the XPS signals prior to HER of a freshly prepared electrode surface. The STM topograph in figure 3.7 (a) reflects a typical structure. The next step is the exposure to the electrolyte solution without any potential applied, which is represented by the grey spectra, followed by XPS experiments performed after HER (blue spectra) to discover effects of hydrogen evolution on the organic co-catalyst (fig. 3.7 c and d). Figure 3.7 (c) shows the results on the C 1s core level: It has a dominant signal around 284 eV that belongs to carbon atoms within the phenyl rings, while the small signal around 286 eV originate from carbon atoms in the triazine ring. The shift to



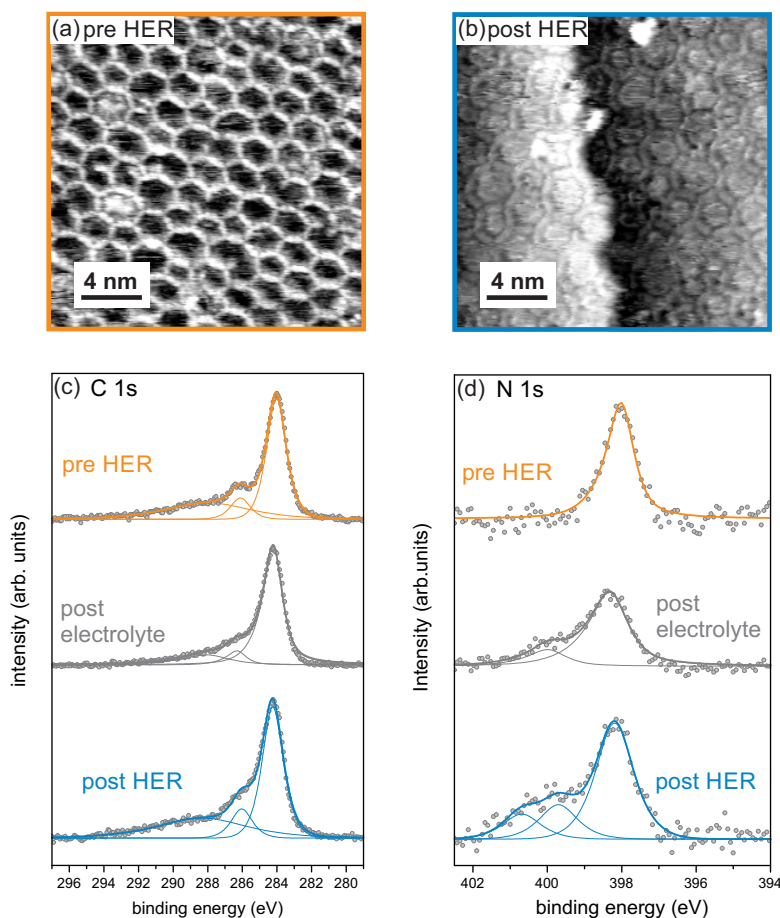


Figure 3.7 – Characterization of the P–N<sub>3</sub> co-catalyst by STM and XPS before and after HER: (a) STM topograph ( $U = -1.2$  V,  $I = 23$  nA) recorded before the HER experiment; (b) STM topograph ( $U = -1.2$  V,  $I = 19$  nA) recorded after the HER experiment: Intact polymer proves the stability of the P–N<sub>3</sub> co-catalyst under the applied electrochemical conditions; (c) XPS spectra of the C 1s core level before HER (orange), after 0.1 M NaOH electrolyte exposure (grey) and after hydrogen evolution (blue): No significant changes are observable in the signal showing the chemical integrity for the applied experimental conditions; (d) XPS spectra of the N 1s core level before HER (orange), after 0.1 M NaOH electrolyte exposure (grey) and after hydrogen evolution (blue): Additional peak at 399.3 eV indicates the interaction with water molecules, while the peak at 401.2 eV can be related with an interaction with hydrogen, which only appears after electrochemical experiments.

higher binding energies is a result of the carbon nitrogen bond. The C 1s signal does not alter during the entire electrochemical process (electrolyte exposure and HER), which reflects the stability of the hybrid electrode for the applied electrochemical conditions.

Figure 3.7 (d) presents the results of the N 1s core level: The signal of a freshly prepared P–N<sub>3</sub> co-catalyst is around 398 eV (3.7 d: orange spectrum). After electrolyte exposure, the spectrum shows an additional peak at 399.3 eV (3.7 d: grey spectrum), which originates most likely from interactions of nitrogen atoms inside the polymer network with reactants and reaction intermediates during HER. Literature reports a similar behavior in carbon nitride



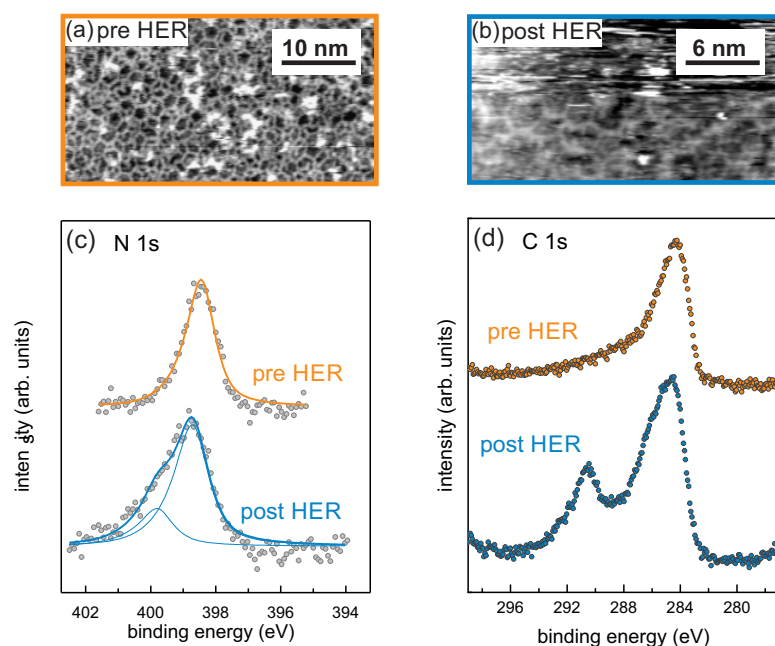


Figure 3.8 – Characterization of the P-N<sub>6</sub> co-catalyst by STM and XPS before and after HER: (a) STM topograph ( $U = -1.1$  V,  $I = 19$  nA) recorded before the HER experiment; (b) STM topograph ( $U = -1.1$  V,  $I = 73$  nA) recorded after the HER experiment: P-N<sub>6</sub> network is observed by STM after electrochemical experiments; (c) XPS spectra of the N 1s core level before (orange) and after HER (blue): Additional peak at 399.3 eV after HER indicate a possible interaction of the nitrogen sites of the p-N<sub>3</sub> co-catalyst with reactants and reaction intermediates; (d) XPS spectra of the C 1s core level before (orange) and after HER (blue): Signal around 285 eV represents the organic network, while the additional peak around 291 eV after hydrogen evolution indicates degradation, like hydrolysis.

thin films: Interactions with polar molecules, such as water and hydroxides partially polarize pyridinic nitrogen atoms and result in the delocalization of the lone pair electrons and shift the N 1s signal to higher binding energies between 399 and 400 eV [84]. However, the chemical structure differs from our organic network, an analogous mechanism is quite likely, since water and hydroxide are the major components of the used electrolyte and water adsorption is an intermediate step within hydrogen evolution in alkaline media (discussed in detail in next section). Therefore, we connect the N 1s signal around 399 eV with adsorbed water or hydroxide that are stabilized by hydrogen bonds. It has to be mentioned that interactions with the metal substrate can appear and are not included in this discussion. The XPS experiment after performing hydrogen evolution measurements reveals two additional peaks: It can be expected that the signal around 399 eV has the same origin as the additional peak described during electrolyte exposure and arises due to adsorption of reactants. However, the signal around 401 eV is of different origin, presumably of the interaction with reaction intermediates, like hydrogen. Literature reports analogous behavior of protonated amino groups [126] that shift the N 1s core level from 399.3 eV to 401.2 eV. Bonding hydrogen to the polymer at the nitrogen site changes the environment from pyridinic to quarternary, since nitrogen gains an additional third ligand and a partial positive charge by losing one valence electron to

the hydrogen bond [84]. Furthermore, free-base porphyrins show also a different signal of incorporated nitrogen atoms. The pyridinc nitrogen is observed at 398 eV and the pyrrolic nitrogen at 400.1 eV [127]. Such XPS studies show the variety of the N 1s core level, due to the structural environment. For this work the difference within the N 1s signal in P–N<sub>3</sub> can be referred to the interaction with reactants and reaction intermediates such as hydrogen and aqueous components and point towards nitrogen as an important element in HER catalysis.

The characterization of the P–N<sub>6</sub> network is analogue to P–N<sub>0</sub> and P–N<sub>3</sub>. The STM and XPS data are shown in figure 3.8. The unaltered electrode surface with the amorphous structure is illustrated in figure 3.8 (a) with the corresponding XPS spectra of the C 1s and N 1s in figure 3.8 (c) and (d) (orange graphs). The blue spectra in figure 3.8 (c) and (d) exhibit the XPS spectra after hydrogen evolution: The N 1s signal shows the additional peak at 400 eV that can be correlated to an interaction between nitrogen and reactants or reaction intermediates like hydrogen [126], analogue to the P–N<sub>3</sub> system. However, the C 1s core level shows an additional signal around 290.6 eV and may indicate degradation by hydrolysis of the polymer. Therefore, the high-binding energy peak can be related to the presence of electron-withdrawing oxygen in the polymer structure [128].

### 3.3 Long-term Stability of Hybrid Electrocatalysts

Some aspects concerning the stability have been shown in the previous section. The stability during the experiment has always been tested by comparing STM and XPS data before and after electrochemical experiments. The co-catalytic systems P–N<sub>0</sub> and P–N<sub>3</sub> were stable during hydrogen evolution, while the P–N<sub>6</sub> system showed already some degradation phenomena.

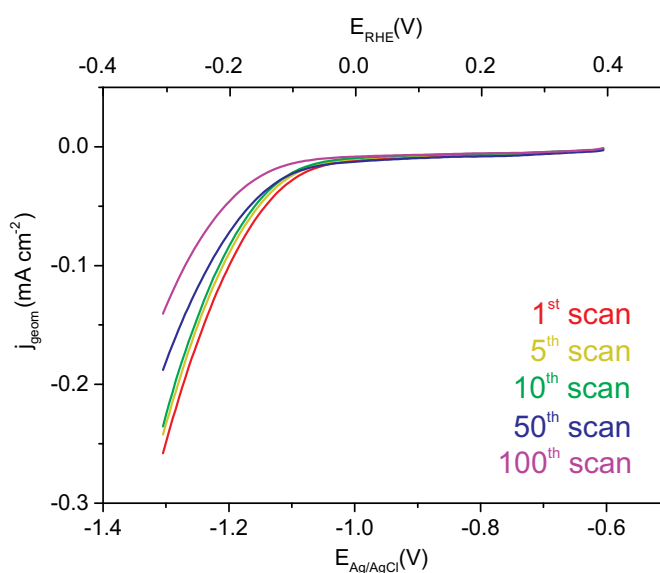


Figure 3.9 – Stability of the P–N<sub>3</sub> co-catalyst on Au(111) measured by 100 cycles in 0.1 M NaOH and 50 mV s<sup>-1</sup> showing a decrease in electrochemical activity over time.

Long-term studies are always necessary to verify the applicability of a catalyst. Therefore, we tested an Au(111) electrode covered with the P-N<sub>3</sub> co-catalyst due to its stability. We performed 100 linear sweeps from  $-0.6$  to  $-1.3$  V<sub>Ag/AgCl</sub> (fig. 3.9) with a scan rate of  $50 \text{ mV s}^{-1}$ . While the electrochemical activity reaches  $-0.26 \text{ mA cm}^{-2}$  during the 1<sup>st</sup> scan, it dropped below  $-0.20 \text{ mA cm}^{-2}$  for the 50<sup>th</sup> scan. For the 100<sup>th</sup> scan the activity reached  $-0.14 \text{ mA cm}^{-2}$ , which is similar to the current density of a bare Au(111) electrode. This leads to the conclusion that the organic co-catalyst decomposes completely during the 100 polarization scans under the applied electrochemical conditions. The decomposition effects in the XPS spectra of figure 3.8 presented in the previous section are in agreement with this conclusion. Additionally, hydrogen gas produced between the organic co-catalyst and the Au(111) electrode might also have an influence on the detachment of the organic compound. Recent studies with organic molecules on calcite showed several water layers between substrate and deposited molecules [129]. Even though the deposition method differs from our work, similar effects might appear in our systems during HER, when reactants or reaction intermediates undergo the organic co-catalyst and result in the detachment of the polymer network, especially in combination with gas production.

### 3.4 HER Mechanism on Hybrid Electrodes

To understand the observed trend in HER activity, theoretical support is required to deliver a further understanding, how water is converted into hydrogen molecules. The following section adds density functional theory (DFT) calculations to the study, which have been performed by Juan Manuel Lombardi, Paula Abufager and Heriberto Fabio Busnengo of the Instituto de Física Rosario and Universidad Nacional de Rosario, Argentina.

The experimental results show a trend in the HER activity, which is  $\text{P-N}_3 > \text{P-N}_6 \approx \text{P-N}_0 > \text{Au(111)}$ . The introduction to the Sabatier principle that depicts the catalytic activity as a function of the binding energy was introduced in chapter 1. In the case of low binding energy the residence time of reaction species is not long enough in order to provoke a sufficient turnover into reaction products. On the other hand, if the binding energy is too strong, reaction intermediates remain on the catalyst surface and block the active sites. Consequently, the optimum catalyst requires an intermediate interaction with the reacting species for an adequate turnover. Therefore, the different binding energies of reactants and reaction intermediates have been calculated by DFT to detect the favored locations of water and hydrogen on the surface of the hybrid catalysts. DFT calculations identified the vertices of each polymer as active site for water and hydrogen adsorption, since they are the regions that require the lowest adsorption energy. Table 3.1 shows the calculated values for water and hydrogen adsorption on each investigated electrode. It has to be mentioned that the hydrogen values in table 3.1 involve hydrogen adsorption after the abstraction from water molecules instead of single hydrogen adsorption.

For a consistent comparison of the investigated electrodes, additional DFT calculations have

Electrode	H <sub>2</sub> O adsorption $E_B^{H_2O}$ [eV]	H abstraction $E_B^H$ [eV]
Au(111)	-0.31	0.20
P-N <sub>0</sub>	-0.44	0.20
P-N <sub>3</sub>	-0.38	-0.36
P-N <sub>6</sub>	-0.77	-0.45

Table 3.1 – Binding energies for water and hydrogen.

been performed of a blank Au(111) substrate. Figure 3.10 (a) shows the calculated surface of a pristine gold surface. The gold atoms exhibit the typical three fold symmetry of a (111) face. Water adsorption on such Au(111) surfaces is illustrated in figure 3.10 (b): The preferred adsorption configuration of water molecules is horizontally on top of a single gold atom ( $E_B^{H_2O} = -0.31$  eV). After abstracting hydrogen from a water molecule (3.47 eV), hydrogen adsorbs in the three fold hollow site between three gold atoms (fig. 3.10 c).

The following section presents DFT calculations of water adsorption and hydrogen abstraction on each hybrid catalyst. For clarity, three different co-catalysts on Au(111) will be discussed together for each single step during HER (water adsorption and hydrogen abstraction).

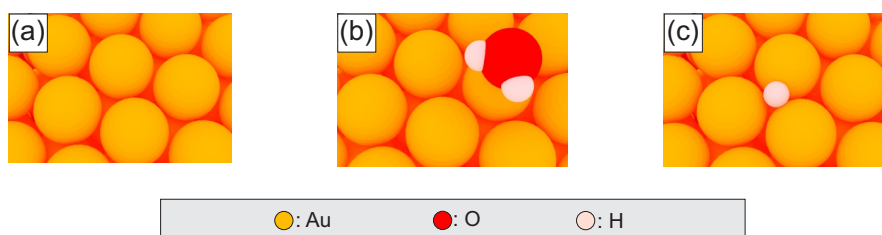


Figure 3.10 – Images calculated by DFT: (a) Pristine Au(111) surface, (b) favored adsorption site of water on Au(111), (c) favored hydrogen adsorption site on Au(111).

### 3.4.1 Water Adsorption on Hybrid Catalysts

As mentioned before DFT identified the vertices of each polymer as active site for water adsorption. They act as docking sites for water molecules and can be regarded as starting point of the water transformation into hydrogen molecules. Figure 3.11 shows schemes of the vertices with a water molecule of each organic co-catalyst. The corresponding DFT image is added in the bottom of each figure. The corresponding values of the water binding energies are listed in table 3.1 ( $E_B^{H_2O}$ ) and exhibit P-N<sub>6</sub> as the most stable configuration (-0.77 eV). Slightly higher binding energies are revealed for P-N<sub>3</sub> (-0.38 eV) and P-N<sub>0</sub> (-0.44 eV). A blank Au(111) surface provides the least stable configuration for water adsorption (-0.31 eV).

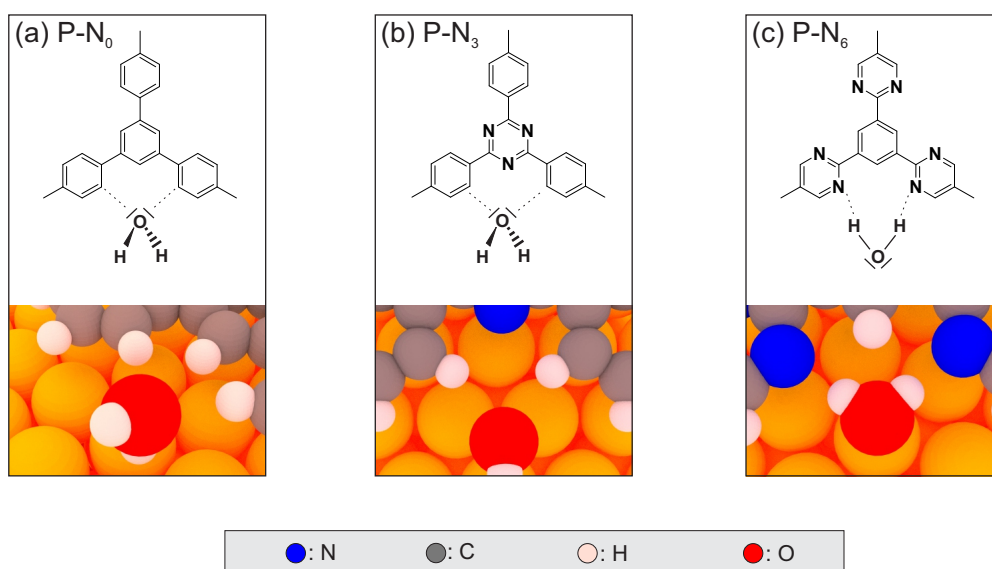


Figure 3.11 – Schematic illustration and DFT images showing the vertices as preferred water adsorption sites of each organic co-catalysts: (a) P-N<sub>0</sub>, (b) P-N<sub>3</sub>, (c) P-N<sub>6</sub>.

### 3.4.2 Hydrogen Abstraction of Water Molecules on Hybrid Catalysts

The next step is the abstraction of hydrogen from water molecules. Figure 3.12 shows schematically the adsorbed hydrogen at the active site of each co-catalyst: The P-N<sub>0</sub> co-catalyst is illustrated in figure 3.12 (a), P-N<sub>3</sub> in figure 3.12 (b) and figure 3.12 (c) shows the configuration of hydrogen and P-N<sub>6</sub>. The catalyst surfaces calculated by DFT can be found in the bottom of each figure.

Table 3.1 ( $E_B^H$ ) shows the corresponding binding energy values for subtracting hydrogen from

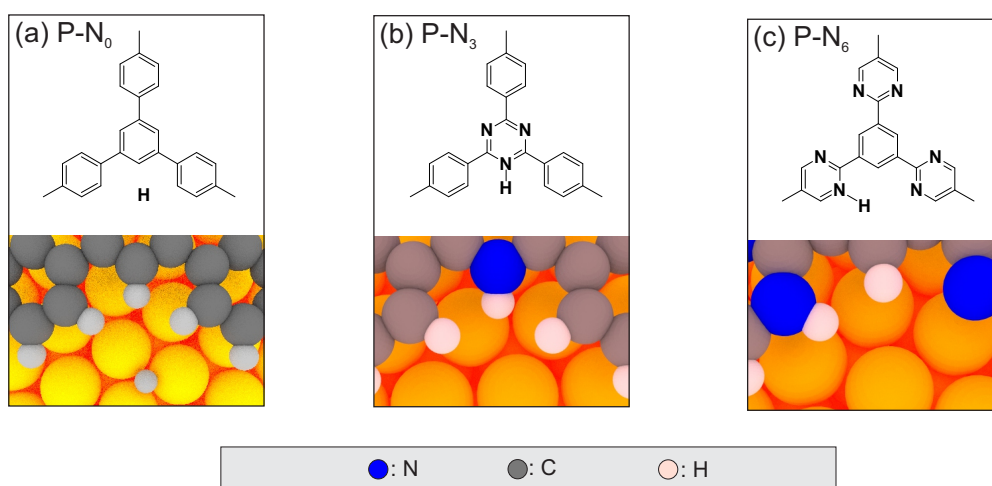


Figure 3.12 – Adsorption configuration of hydrogen and organic co-catalysts after hydrogen abstraction from water: (a) P-N<sub>0</sub>, (b) P-N<sub>3</sub> and (c) P-N<sub>6</sub>.

water and binding it to the hybrid catalyst surface. The combination of P–N<sub>6</sub> on gold is once more the most stable configuration (2.82 eV) followed by P–N<sub>3</sub> (2.91 eV). Au(111) and P–N<sub>0</sub> have the same value of 3.47 eV, since there is no further stabilization of hydrogen by the P–N<sub>0</sub> co-catalyst and hydrogen is located in the three fold hollow site between three gold atoms (fig. 3.12 a). The P–N<sub>3</sub> and P–N<sub>6</sub> co-catalysts have nitrogen heteroatoms implemented in their structure, which interact with hydrogen and stabilize it on the electrode surface. The DFT calculations support the XPS results that showed an interaction between nitrogen and hydrogen during HER. Hydrogen is bound to the polymer, which results in an additional ligand at the nitrogen site and shifts the N 1s core level to higher binding energies in the XPS spectra (XPS in figure 3.7). This highlights the importance of nitrogen heteroatoms in the polymer network of organic co-catalysts for supporting HER.

### 3.4.3 Correlation between Electrochemical Activity and Binding Energy

The adequate correlation between experiment and theory requires a comparison of the catalytic activity with the energy difference of water adsorption and hydrogen abstraction because the energy difference describes the required energy amount to separate hydrogen from water. Table 3.2 shows the energy differences between water and hydrogen binding energy ( $E_B^H - E_B^{H_2O}$ ) of the investigated electrodes. The energy values for  $E_B^H$  and  $E_B^{H_2O}$  are taken from table 3.1.

Electrode	$HBE_{app} = E_B^H - E_B^{H_2O}$ [eV]
Au(111)	0.51
P–N <sub>0</sub>	0.64
P–N <sub>3</sub>	0.02
P–N <sub>6</sub>	0.45

Table 3.2 – Investigated electrodes with the calculated apparent hydrogen binding energy.

The P–N<sub>3</sub> system requires only 0.02 eV to separate hydrogen from water, which is the lowest energy amount of the investigated co-catalytic systems, followed by P–N<sub>6</sub> (0.45 eV) and Au(111) (0.51 eV). The highest energy amount is needed within the P–N<sub>0</sub> co-catalyst, which needs 0.64 eV to separate hydrogen from water. Figure 3.13 summarizes the results from table 3.1 and 3.2 and illustrates graphically the advantage of the hybrid electrode with the P–N<sub>3</sub> co-catalyst, since the energy of water adsorption and hydrogen abstraction are almost on the same level. Considering the energy difference as a limiting factor within hydrogen evolution allows a good explanation for the different catalytic activities that are observed in this study.

A similar approach has been taken by another group, who introduced the apparent hydrogen binding energy  $HBE_{app}$  as descriptor for HOR and HER [72]. It combines the hydrogen binding energy ( $E_B^H$ ) and the water binding energy ( $E_B^{H_2O}$ ):  $HBE_{app} = E_B^H - E_B^{H_2O}$  [72]. This approach turns away from the conventional hydrogen binding energy ( $E_B$ ), since it is an intrinsic property and does not implement external effects, like pH of aqueous electrolytes. Since 0.1 M NaOH

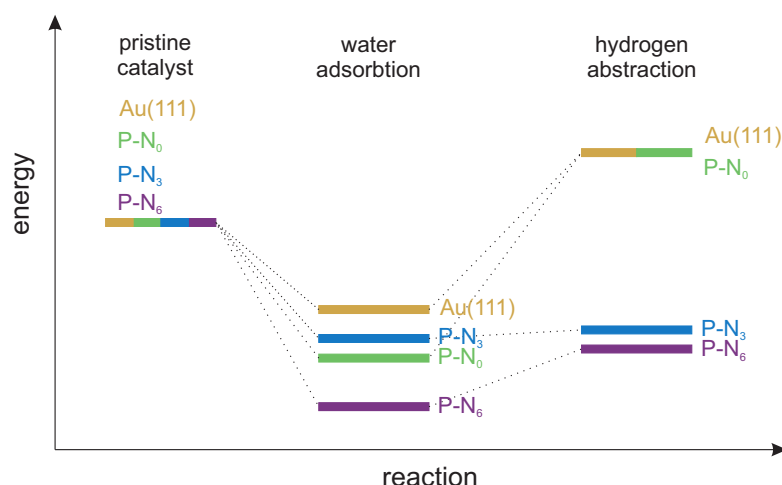


Figure 3.13 – Schematic energy diagram of water and hydrogen adsorption for Au(111) and investigated hybrid electrodes.

was used as electrolyte in this work, the electrode surface is always in contact with water and adsorption/desorption of hydrogen is accompanied by the adsorption/desorption of water [72, 130]. Therefore, the apparent hydrogen binding energy  $\text{HBE}_{\text{app}}$  is more suitable as a descriptor, because it includes pH dependencies in describing electrochemical activities with hydrogen adsorption remaining a major reaction step in acid and alkaline electrolytes. Additionally, it was shown that the adsorption of hydrogen is the critical step for all pH values [74]. Including these recent developments, the measured catalytic activities can be visualized as a function of the apparent hydrogen binding energy, which replaces the conventional hydrogen binding energy as descriptor for HER.

The results can be summarized in a volcano plot, which is shown in figure 3.14: The overall volcano plot in figure 3.14 (a) was introduced in chapter 1 to illustrate the relation between catalytic activity and hydrogen binding energy. Figure 3.14 (b) shows the segment of a volcano plot that is generated by the measured catalytic activities of the investigated electrodes in this work with the apparent hydrogen binding energy as descriptor.

It has to be mentioned that the segment in figure 3.14 (b) does not represent a precise section of the area marked in figure 3.14 (a), since the Gibbs free energy of hydrogen has been taken as descriptor in figure 3.14 (a) instead of the apparent hydrogen binding energy  $\text{HBE}_{\text{app}}$  like we used in our study (fig: 3.14 b). However, the connection in figure 3.14 illustrates how hydrogen evolution with organic polymer co-catalysts can be integrated in established volcano plots. The position of P-N<sub>3</sub> with its high activity can be connected to an optimal balance between water and hydrogen binding energies that are similar to Pt(111). In comparison to the P-N<sub>3</sub> system, the P-N<sub>6</sub> co-catalyst binds water stronger than hydrogen and active sites are already partially blocked, which diminishes the catalytic activity. Hydrogen adsorption on Au(111) becomes endothermic when considering water adsorption, inducing a further increase of  $\text{HBE}_{\text{app}}$  and a reduction of its expected catalytic activity with respect to P-N<sub>3</sub> and P-N<sub>6</sub>. Thus,

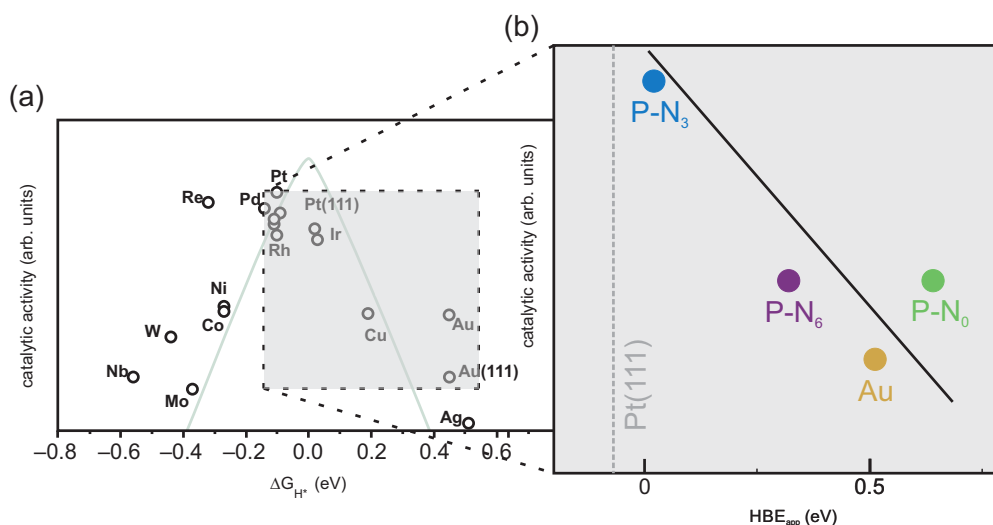


Figure 3.14 – Quasi-volcano plot of Au(111) and hybrid electrodes: (a) Overall volcano plot (modified with permission from ref. [70]); (b) Volcano segment of the experimental catalytic activities of each investigated electrode as a function of its calculated apparent hydrogen binding energy  $HBE_{app}$ ; Additionally, the position of Pt(111) with the  $HBE_{app}$  descriptor is included.

the theoretical results are in line with the experimental trend of HER activities:  $P-N_3 > P-N_6 > Au(111)$ . However, there remain discrepancies concerning the  $P-N_0$  electrode: The apparent hydrogen binding energy does not apply for the measured activity of the  $P-N_0$  hybrid system, which is higher than the calculated activity of a bare Au(111) electrode. It has a similar activity to the one obtained for the  $P-N_6$  system. This result indicates that other reaction steps might be rate limiting and further parameters are required for a full description of all the investigated systems.

Such parameters might involve a particular binding geometry: Our calculations show a different adsorption geometry of water for the investigated electrodes. On  $P-N_0$  and  $P-N_3$ , water molecules adsorb vertical to the surface with a hydrogen atom pointing downwards towards the gold substrate (vertical configuration), which is in line with previous theoretical results [131]. However, on  $P-N_6$ , water molecules adsorb parallel to the surface where hydrogen atoms of water form hydrogen bonds with nitrogen within the organic co-catalyst (horizontal configuration). Figure 3.15 shows the antibonding orbitals of water in the horizontal (fig. 3.15 a) and the vertical configuration (fig. 3.15 b) on gold. Only the vertical configuration of water (fig. 3.15 b) shows an overlap of the antibonding orbitals with the gold electronic states, which simplifies electron transfer into the antibonding  $4a_1$  and  $2b_2$  orbitals of water. In consequence, the H–O bond is destabilized and water dissociation with hydrogen generation is increased. A similar overlap of antibonding states is absent during water adsorption on Au(111) and on the  $P-N_6$  hybrid electrode and electron transfer is not further enhanced. The proposed configuration of water adsorption to facilitate the reductive charge transfer has been observed in calculations for Au(111) and Pt(111) [132]. These studies show that room temperature, water layers on gold become disordered, while on platinum it remains



partially in the vertical configuration (similar to fig. 3.15 b). If this binding geometry affects the catalytic activity of platinum, a similar mechanism can be anticipated for the P–N<sub>0</sub> and P–N<sub>3</sub> co-catalysts, which would be a possible explanation why P–N<sub>0</sub> and P–N<sub>6</sub> have similar catalytic activities.

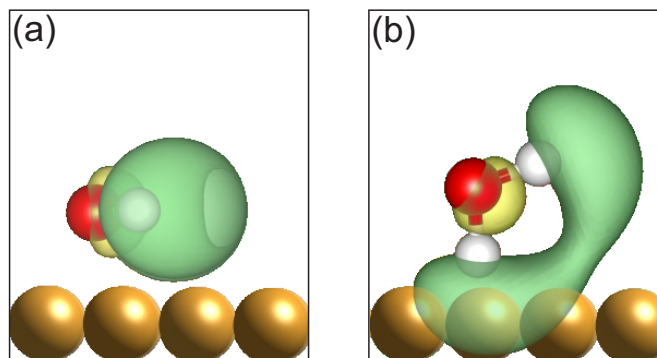


Figure 3.15 – Antibonding 4 a 1 and 2 b 2 orbitals of water adsorbed on Au(111): (a) Horizontal configuration: Water molecule is adsorbed parallel to the gold surface and the antibonding states of water do not interfere with the gold electronic states, (b) Vertical configuration: Water molecule is adsorbed vertical to the gold surface, with one hydrogen atom pointing towards the surface, resulting in an overlap of the antibonding states of water with the electronic states of the gold surface.

### 3.5 Quantifying the Catalytic Activity in Organic co-Catalysts

The support of DFT in the previous section allowed us to identify the active sites in the hybrid electrodes. They are located in the vertices of the organic co-catalyst, which is valid for all the three hybrid electrodes (fig. 3.11). This achievement allows to quantify the specific catalytic activity by the turnover frequency (TOF), which is an established method to evaluate the catalytic activity of different catalysts [117]. It calculates the amount of electrons or moles that are transferred by a catalyst per time. A precise measurement of the TOF requires a chronoamperometric analysis, which measures the current at a constant potential over a defined time period. Ideally gas chromatography is added to measure the precise amount of hydrogen that is produced during the reaction. Due to the limited stability of the organic co-catalysts, the necessary time scales for chronoamperometry result in the degradation of the organic component as it was shown in experiments on the long-term stability (fig. 3.9). Therefore we use a calculation of the TOF at a specific potential that expresses the catalytic activity as the produced amount of hydrogen molecules per monomer and per second according to equation 3.2

$$H_2 [s^{-1} monomer^{-1}] = \frac{I}{2 \cdot e \cdot N_{monomer}}. \quad (3.2)$$

The measured current of the entire electrode surface  $I$  is divided by the elementary charge

### Chapter 3. Enhancing HER through Molecular Engineering

$e$  and the total amount of monomers on the surface  $N_{monomer}$ , which were estimated from STM images. The factor 2 has to be implemented to account for two electrons that are needed to form a hydrogen molecule. With this TOF calculation at specific potentials, we estimate the catalytic turnover at  $-1.1 V_{AgCl}$ ,  $-1.2 V_{AgCl}$  and  $-1.3 V_{AgCl}$ . Calculations for a pure metallic gold electrode are included with the assumption of the same amount of active sites on Au(111) than on the hybrid electrodes. The calculated specific TOF values are summarized in table 3.3.

Electrode	TOF-1.1 V [ $s^{-1}$ ]	TOF-1.2 V [ $s^{-1}$ ]	TOF-1.3 V [ $s^{-1}$ ]
Au(111)	1.60	3.90	9.54
P-N <sub>0</sub>	2.10	6.31	15.94
P-N <sub>3</sub>	2.36	10.78	32.33
P-N <sub>6</sub>	1.65	5.17	16.10

Table 3.3 – Turnover frequency (TOF) of the investigated electrodes at given potentials.

The TOF values exhibit a similar turnover at  $-1.1 V_{AgCl}$  between the investigated electrodes. Au(111) and P-N<sub>6</sub> have similar values around  $1.60 s^{-1}$ . The highest turnover at  $-1.1 V_{AgCl}$  has the hybrid electrode with the P-N<sub>3</sub> co-catalyst ( $2.36 s^{-1}$ ), which is in line with the lower onset potential discussed in a previous section. At  $-1.2 V_{AgCl}$  the turnover of P-N<sub>3</sub> is almost twice as high as the TOFs of P-N<sub>0</sub> and P-N<sub>6</sub>, which have from their side a significant higher turnover than a pure metal Au(111) electrode (P-N<sub>0</sub>: 40 % higher and P-N<sub>6</sub>: 25 % higher than gold). The TOFs at  $-1.3 V_{AgCl}$  exhibit a similar ratio as the values at  $-1.2 V_{AgCl}$ : The P-N<sub>3</sub> co-catalyst exhibits the highest turnover ( $32.33 s^{-1}$ ), which is twice as high as the values of P-N<sub>0</sub> ( $15.94 s^{-1}$ ) and P-N<sub>6</sub> ( $16.10 s^{-1}$ ). The TOF of Au(111) reaches only  $9.54 s^{-1}$ , which is 40% less than the TOFs of P-N<sub>0</sub> and P-N<sub>6</sub>.

It has to be mentioned that the TOF values presented in table 3.3 do not represent an overall specific activity of the catalyst. They are point recordings at a defined potential, which makes the comparison with other catalysts outside this study quite challenging. Our approach of characterizing the specific catalytic activity with the TOF at defined potentials has also been used to describe the activity in Ni-Mo nano powders [133]. Since Ni-Mo powder catalysts are purely metallic, the TOF values are normalized per surface atom [10, 133], since it can be assumed that each atom at the surface acts as catalytic active site. If not every surface atom equals an active site, TOF values can be normalized per electrochemical active site instead of surface atom [119, 134, 135], which has also been done in this thesis, due to the additional use of organic components as co-catalysts. Since there are many different definitions of the TOF available in literature, one has to be careful when comparing TOF values of different studies, since benchmarking tools are very limited within this scientific field. However, some groups tried to approach this problem by introducing a method that combines the electrochemical active surface area (ECSA) with the measured current to obtain a tool to compare electrochemical activities of different studies [117, 136]. They are of particular interest when the catalytic active centers are unknown and  $N_{monomer}$  in equation 3.2 cannot be determined.

However in this study the combination of DFT and STM allowed to identify the catalytic

active sites and estimate the amount of molecules on the surface, which made it possible to determine the catalytic turnover by equation 3.2.

### 3.6 Hybrid Electrodes beyond HER

So far this chapter reported how Au(111) electrodes decorated with organic polymer co-catalysts contribute to an increased activity of hydrogen evolution. However, there are many energy conversion reactions, which require the aid of catalysts in order to be efficient, such as the evolution/reduction of oxygen or the reduction of  $\text{CO}_2$ . In the light of future experiments, the hybrid electrodes were tested as catalysts for the oxygen reduction reaction (ORR). Therefore, hybrid electrodes were prepared accordingly to the HER experiments described in this chapter. In addition to the  $\text{P-N}_3$  polymer that was used as co-catalyst, cobalt was evaporated to the surface, since it is reported that cobalt has a higher catalytic activity than gold [137].

The experimental procedure was analogue to the HER experiments. The fabrication of the catalyst was performed in an UHV chamber and catalyst characterization was performed in three steps: 1) STM prior to ORR, 2) exposure of the catalyst surface to the electrolyte solution (0.1 M NaOH) without any potential applied and 3) STM after ORR.

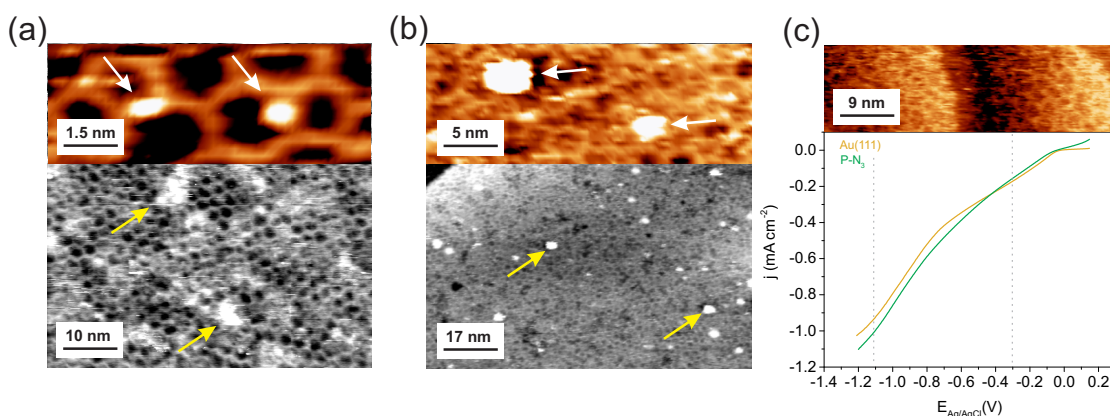


Figure 3.16 – Cobalt supported oxygen reduction with  $\text{P-N}_3$  hybrid electrode: (a) STM image ( $U = -1.1$  V,  $I = 23$  pA) of the electrode surface prior to ORR with evaporated Co clusters on top of the organic co-catalyst; (b) STM image ( $U = -1.1$  V,  $I = 45$  pA) of the electrode surface after electrolyte exposure, with clusters remaining on the surface; (c) ORR with Co supported hybrid electrode, revealing no significant impact of the catalyst on the activity of ORR; STM image ( $U = -0.9$  V,  $I = 67$  pA) in the top shows the  $\text{P-N}_3$  co-catalyst stable during ORR, while the metal clusters were not observed.

Figure 3.16 (a) shows an overall STM image of the electrode surface before oxygen reduction: The  $\text{P-N}_3$  is deposited on top of Au(111). Additionally, cobalt is evaporated on the electrode surface, which are the white clusters on the polymer network (marked by arrows) in figure 3.16 (a). The insert in the top shows a high resolution STM topograph and exhibits the nucleation sites of cobalt, which are the ligands of the polymer network instead of areas at the vertices or inside the pores. This observation is in line with previous studies that observed cobalt nucleation sites on top of organic ligands with an underlying Ag(111) substrate [138].

According to this study, the mobility of cobalt is highly sufficient, since cobalt forms large islands on clean Ag(111) at similar deposition parameters. Although substrate and precise chemistry of the organic network differs in this study, a similar mechanism can be expected for cobalt evaporated on polymers with an underlying Au(111) crystal. Figure 3.16 (b) exhibits the cobalt decorated hybrid electrode surface after the exposure to 0.1 M NaOH electrolyte solution. The organic network is still observable and clusters can be identified. However, it cannot be assured that such clusters are cobalt or residue from the electrolyte solution. Future experiments need to involve XPS to identify the chemical composition of these clusters, e.g. its oxidation number. XPS also will enable estimating exact amounts of cobalt on the surface. In the following, the electrode decorated with the P-N<sub>3</sub> polymer and cobalt was tested as electrocatalyst for oxygen reduction. The corresponding polarization curves were recorded with 50 mV s<sup>-1</sup> and are shown in figure 3.16 (c): Both curves reveal two small and broad peaks around -0.3 and -1.1 V<sub>AgCl</sub>, which represents a 2 + 2e<sup>-</sup> electron reduction pathway. The first peak at -0.3 V<sub>AgCl</sub> corresponds to the reduction of oxygen to H<sub>2</sub>O<sub>2</sub> (HO<sub>2</sub><sup>-</sup> in basic media) as an intermediate product. The second peak at -1.1 V<sub>AgCl</sub> represents the reduction of H<sub>2</sub>O<sub>2</sub> to the final product H<sub>2</sub>O, which appears as OH<sup>-</sup> in alkaline media. The corresponding mechanism of oxygen reduction in a 2 + 2e<sup>-</sup> pathway has been presented in section 1.1.4 (eqn: 1.15 and 1.16).

The combination of cobalt and organic co-catalyst on a gold electrode did not result in a significant change in the ORR activity, since both polarization curves reveal the same trend in figure 3.16 (c). The 2 + 2e<sup>-</sup> pathway, which can be observed for blank Au(111) appears also with the metal-organic decorated electrode. It is very likely that the green curve in figure 3.16 (c) simply reflects the activity of the underlying Au(111) substrate and the combination of cobalt and polymer does not contribute as a catalyst in ORR. The question why the organic co-catalyst is not active in ORR, while catalyzing HER requires further investigations. It can be speculated that the polarity of the reactant molecule plays an important role. HER in alkaline media starts of water, which interacts with the free electron pair of nitrogen inside the polymer. Since oxygen as the reactant in ORR has no dipol moment, no electrostatic interaction can occur with the polymer and the docking sites of the organic co-catalyst are of minor importance.

## 3.7 Conclusion

This chapter has shown the combination of STM and electrochemistry to fabricate and characterize hybrid catalysts by depositing organic polymers on top of Au(111) electrodes. XPS and DFT have been used to provide a deeper insight into the mechanism on the nanoscale. The porous organic co-catalysts provide well defined docking sites for water and hydrogen molecules during hydrogen evolution. Binding energy and residence time are increased at nitrogen atoms within the organic co-catalyst by hydrogen bonds, which increases the catalytic activity for the P-N<sub>3</sub> hybrid electrode. Adding higher amounts of nitrogen in the co-catalytic network decreases the catalytic activity, because binding energies are too strong and reaction intermediates start to block the active sites of the catalyst (see P-N<sub>6</sub> hybrid electrode). For

a complete understanding of the mechanism of hydrogen evolution, additional parameters need to be taken into account, such as local binding geometries of reactants. Water molecules tend to show a vertical adsorption configuration on  $P-N_0$  and  $P-N_3$  electrodes, which results in an overlap of the antibonding states of water with the electronic states of the Au(111) substrate. Thereby electron transfer into the antibonding states of water is facilitated, which simplifies breaking the H–O bond.

The identification of the catalytic active sites of the hybrid electrodes allows to evaluate the specific catalytic activity as turnover frequency (TOF), which was determined for all investigated electrode surfaces. Although, there are various definitions of the TOF in literature, the turnover is calculated as produced hydrogen per monomer and second. In addition the electrochemical active surface area (ECSA) was determined by double layer capacitance measurements within the non-Faradaic region of the HER for Au(111) and the polymer decorated surface. The capacitance values have no significant difference and therefore the organic co-catalysts do not contribute in the roughness of the overall hybrid electrode surface. Consequently, the ECSA of blank Au(111) electrode is comparable with the ECSA of polymer decorated hybrid electrodes.

The future of hybrid electrodes supported by organic co-catalysts was tested in preliminary ORR experiments. In addition cobalt was added to the organic component of the electrode surface. The nucleation site of cobalt clusters on the ligands of the organic co-catalyst was identified and a  $2 + 2e^-$  pathway was observed during electrochemical experiments. The co-catalytic components of organic polymer and metallic cobalt did not increase the ORR activity, which is probably due to the missing dipole moment within the oxygen molecule. While an electrostatic interaction occurs with water molecules in HER, oxygen can only interact by van der Waals forces with the electrode surface.

The results of this chapter highlight the importance of organic/inorganic catalysts for electrocatalysis. The binding energy between catalyst surface and reactant can be optimized by implementing suitable reaction sites into precursor molecules that build up the organic co-catalyst. They act as docking sites and change the residence time of electrochemical reactants and reaction intermediates and shift the position in the corresponding volcano plot. The structure of the organic co-catalyst has to be adapted depending on the electrochemical reaction and its reactants in order to achieve the best turnover. Additionally, it has to be fine tuned for reaching sufficient catalytic activities. This approach requires a strong cooperation of organic- and electrochemistry for fabricating the optimal co-catalyst for the studied reaction. However, this will provide a new way of enhancing electrocatalytic reactions on earth abundant transition metals catalysts, as it has been shown for the HER in this work.



## 4 Performance of Phthalocyanines as ORR-Catalysts

It has been successfully shown in chapter 3 how organic co-catalysts can improve the catalytic activity of electrochemical reactions. It was also tried to improve the catalytic activity of the oxygen reduction reaction (ORR) by the combination of a polymer network with metallic cobalt, which ultimately did not improve the ORR activity. It has been previously reported that the size from nano- to subnano size and even to single metal atoms leads to a tremendous increase of the catalytic activity [22]. To make single metal atoms applicable for electrocatalysis, organic molecules like porphyrins and phthalocyanines can be metalized [23] and deposited on surfaces. Such an approach has already been performed for the ORR [20, 139, 140, 141, 142] and metal centers in porphyrins or phthalocyanines can be used as single-atom catalysts.

In this chapter, fused cobalt phthalocyanines are used as catalysts to support the reduction of oxygen, since such molecules reveal an optimal combination between activity and durability during oxygen reduction [143]. The investigation focuses on the large conjugated  $\pi$ -system of the fused phthalocyanines and how it affects the catalytic activity of oxygen reduction. The study involves the investigation of cobalt phthalocyanines with a single macrocycle, which are compared with the fused version. The synthesis of such fused molecules requires the utilization of triisopropylsilyl (TIPS) protection groups in order to inhibit undesired reactions during the synthesis. In consequence the organic macrocycle of the fused and single cobalt phthalocyanines are equipped with TIPS ligands. Both molecules were deposited on a gold electrode respectively and test as electrocatalysts for the ORR.

### 4.1 Preparation of the Electrode Surfaces

The utilized molecules that act as catalysts during this study are schematically illustrated in figure 4.1: The fused cobalt phthalocyanine ( $\text{Co}_2\text{Pc}_2(\text{TIPS})_{12}$ ) is schematically shown in figure 4.1 (a). By fusing such phthalocyanine molecules, the amount of cobalt atoms per molecule is doubled. The synthesis requires bulky triisopropylsilyl (TIPS) groups, which are often used in organic chemistry to block reactive sites at molecules and inhibit inadvertent reaction pathways. Figure 4.1 (b) shows a scheme of a single cobalt phthalocyanine molecule

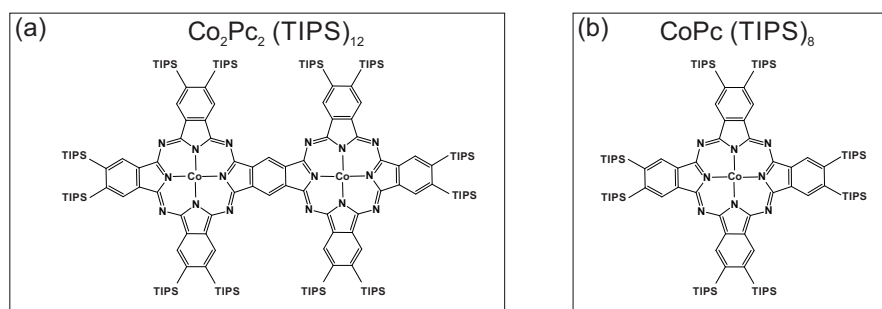


Figure 4.1 – Schematic overview of the used phthalocyanines with TIPS protection groups: (a) Fused cobalt phthalocyanine; (b) Single cobalt-phthalocyanine.

( $\text{CoPc}(\text{TIPS})_8$ ), which has only one cobalt atom in its organic cycle. Like the fused molecule, the macro cycle of the single cobalt phthalocyanine is equipped with bulky TIPS groups to ensure an equivalent environment of the cobalt center on the electrode surface. Both molecules were synthesized by the group of Prof. Mario Ruben (Karlsruhe Institute of Technology, Chair of Molecular Materials, Karlsruhe, Germany).

The TIPS groups that are attached to the phthalocyanines increase the size of both molecules significantly (especially  $\text{Co}_2\text{Pc}_2(\text{TIPS})_{12}$ ), which makes the deposition in UHV by molecular beam epitaxy very challenging. Instead of an UHV preparation, molecule deposition has been performed at ambient conditions: The used substrates for this study are crystalline gold films on a glass substrate with an intermediate chromium layer in order to attach the gold to glass. Such gold substrates are commercially available (arrandee GmbH & Co. KG). The gold substrates were annealed with an Elmaflame 300 hydrogen soldering and welding unit (Elma Schmidbauer GmbH) to produce well defined Au(111) terraces with several hundred nanometers in size.

Molecule deposition has been performed by drop casting: The phthalocyanine molecules in figure 4.1 were dissolved separately in benzene and deposited on the flame annealed Au(111) substrate by a micropipette. The surface was rinsed with a pure benzene solution to remove excess molecules until roughly a monolayer of molecules remained on the substrate.

An ambient Scanning Tunneling Microscope (Agilent Technologies) was used to image the surface of the phthalocyanine covered surface and to characterize the electrode surface prior to oxygen reduction.

### 4.2 Characterization by STM and XPS

The surface of a typical electrode covered with  $\text{Co}_2\text{Pc}_2(\text{TIPS})_{12}$  molecules is visualized in figure 4.2 (a). The molecules cover the majority of the Au(111) surface, however areas can appear that remain uncovered and where molecules have been removed during the washing process. The enlargement in figure 4.2 (b) shows the  $\text{Co}_2\text{Pc}_2(\text{TIPS})_{12}$  molecules in more detail. Besides



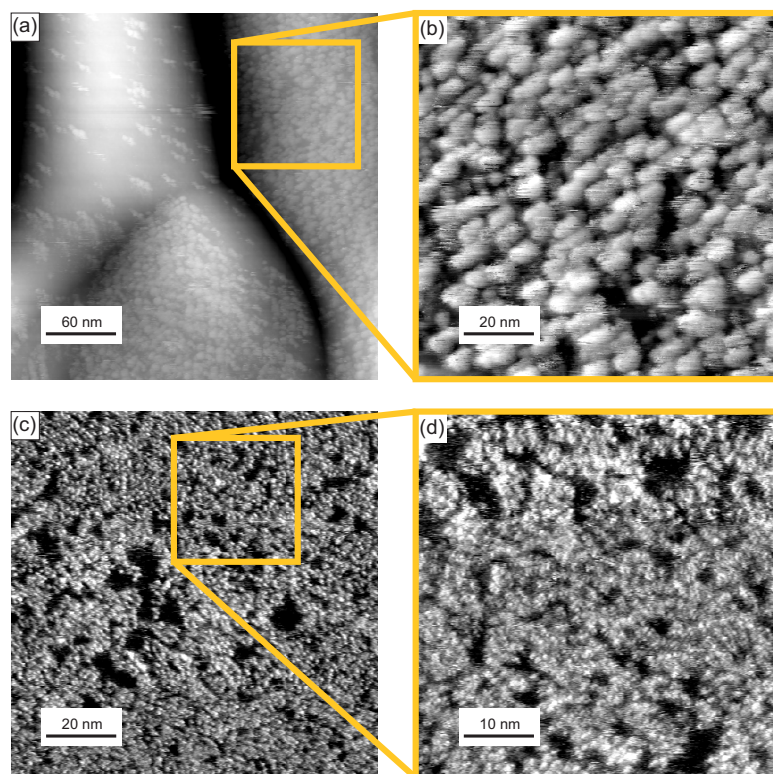


Figure 4.2 – STM image of cobalt phthalocyanines molecules on Au(111): (a) Overview of a sub monolayer of  $\text{Co}_2\text{Pc}_2(\text{TIPS})_{12}$  molecules ( $U = 0.4 \text{ V}$ ,  $I = 0.2 \text{ nA}$ ), with some areas revealing the Au(111) substrate; (b) Enlargement of the  $\text{Co}_2\text{Pc}_2(\text{TIPS})_{12}$  molecules ( $U = 0.4 \text{ V}$ ,  $I = 0.2 \text{ nA}$ ); (c) STM image of  $\text{CoPc}(\text{TIPS})_8$  molecules ( $U = 0.4 \text{ V}$ ,  $I = 0.5 \text{ V}$ ); (d) Enlargement of  $\text{CoPc}(\text{TIPS})_8$  molecules ( $U = 0.4 \text{ V}$ ,  $I = 0.5 \text{ V}$ ).

of a preferred arrangement due to the chemical structure, a dominant ordering mechanism was not observed. Figure 4.2 (c) shows the surface of a gold electrode covered with the single phthalocyanine molecules  $\text{CoPc}(\text{TIPS})_8$ . Like the fused molecules,  $\text{CoPc}(\text{TIPS})_8$  do not follow a particular assembly mechanism according to the recorded STM images (fig. 4.2 d).

In addition to the characterization by STM, the surface was investigated by XPS. The  $\text{Co } 2p_{3/2}$  core level of  $\text{Co}_2\text{Pc}_2(\text{TIPS})_{12}$  is shown in figure 4.3. The spectrum reveals two peaks: A large signal around 780 eV and a smaller signal around 784.5 eV. The spectrum obtained in this work is similar to the  $\text{Co } 2p_{3/2}$  signal in cobalt oxide materials [144, 145] and cobalt porphyrins on Au(111), which also show a dominant peak at 780 eV [146]. A different study on cobalt phthalocyanines reports the  $\text{Co } 2p_{3/2}$  of a monolayer around 778.5 eV, which is slightly lower than the binding energy that was detected in this study. However, fabricating multilayers of cobalt phthalocyanines shifts the binding energy to higher values around 780 eV, which is in the exact range that has been observed in this work [147]. Since STM of our fabricated samples revealed sub monolayers rather than multilayers (see fig. 4.2 a), the shift within the binding energy has to be of different origin. Previous studies suggested already a strong interaction between cobalt phthalocyanines and gold when the molecules are adsorbed on the surface [148, 149]. The molecule-substrate interaction quenches the magnetic moment of the cobalt

atoms completely, which is not observed in free cobalt phthalocyanine molecules. If gold and cobalt phthalocyanines are in contact, the DOS will change and reveal a cobalt contribution in the molecular orbitals, which can be explained by an interaction of Co  $3d_{z^2}$  and Au  $6s$  orbitals [150]. By creating multilayers, the majority of molecules does not have access to the surface and such interactions do not occur, which results in the shift within the XPS spectra of the Co  $2p_{3/2}$  signal. The cobalt phthalocyanines that were investigated with XPS in this work are equipped with bulky TIPS protection groups, that have a similar effect, since they move the cobalt atom further away from the Au(111) surface and inhibit interactions that might affect the Co  $2p_{3/2}$  core levels.

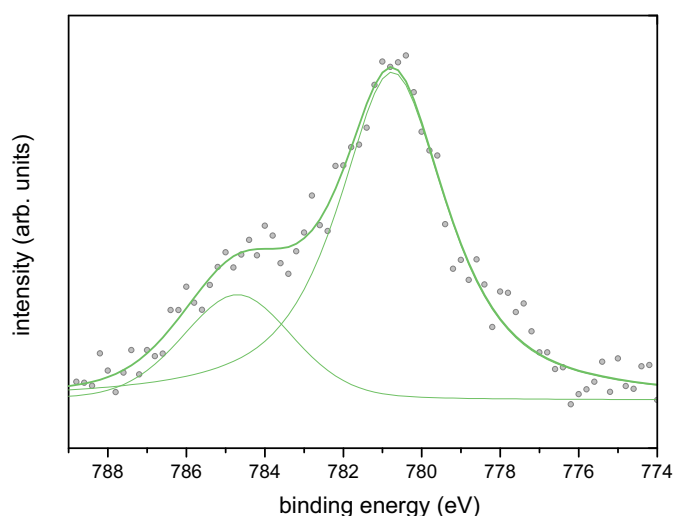


Figure 4.3 – XPS spectra of the Co  $2p_{3/2}$  core levels in  $\text{Co}_2\text{Pc}_2(\text{TIPS})_{12}$ .

### 4.3 ORR with Hybrid Electrodes

After characterizing the hybrid electrodes with STM and XPS, they were tested as electrocatalysts for oxygen reduction in 0.1 M NaOH and a scan rate of  $50 \text{ mV s}^{-1}$ . The complete polarization curve is exemplarily illustrated in figure 4.4 (a) for  $\text{CoPc}(\text{TIPS})_8$  and reveals a  $2 + 2e^-$  pathway. One peak appears around  $-0.25 \text{ V}$ , which can be related to the reduction of oxygen to  $\text{H}_2\text{O}_2$  (eqn. 1.15). The second peak is observed around  $-1.2 \text{ V}$  and represents the reaction from  $\text{H}_2\text{O}_2$  to water (eqn. 1.16). In addition, the complete cyclic voltammogram is added in figure 4.4 (b): Besides the reduction of the gold substrate around  $+0.05 \text{ V}$  no reaction peaks are present, which is a clear indication that both oxygen reduction peaks in figure 4.4 (a) originate from the cobalt phthalocyanine molecules.

Figure 4.4 (c) shows the comparison between the different phthalocyanine catalyst at the first reduction step when oxygen reacts to  $\text{H}_2\text{O}_2$ : The green curve represents the measurement of an electrode covered with  $\text{Co}_2\text{Pc}_2(\text{TIPS})_{12}$  molecules, while the blue curve corresponds to the signal of gold with  $\text{CoPc}(\text{TIPS})_8$  catalysts. Both hybrid electrodes catalyze the ORR at the same overpotential, which is around  $-0.29 \text{ V}$ . Consequently the extension of the  $\pi$ -network around

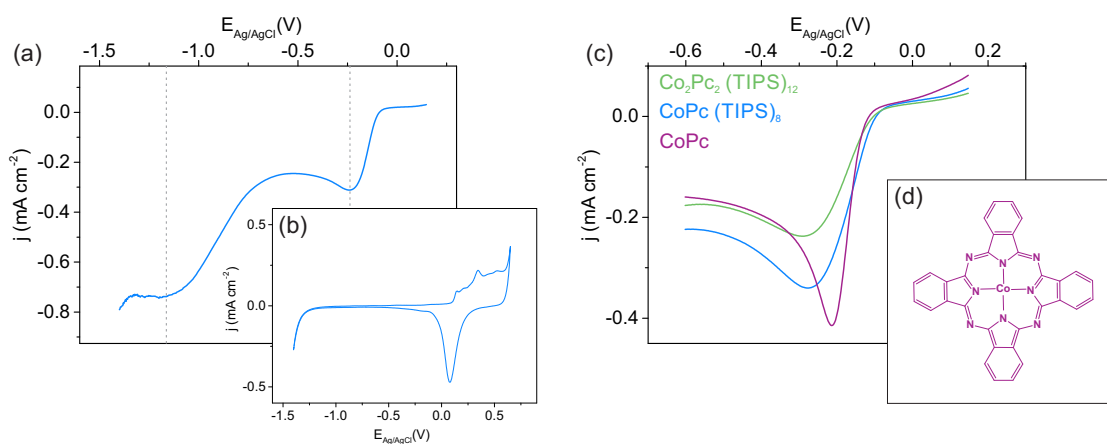


Figure 4.4 – Oxygen reduction with cobalt phthalocyanine catalysts in O<sub>2</sub> saturated 0.1 M NaOH solution with a 50 mV s<sup>-1</sup> scan rate: (a) Polarization curve of CoPc(TIPS)<sub>8</sub> on Au(111) revealing a 2 + 2e<sup>-</sup> mechanism; (b) Cyclic voltammogram of Au(111) covered with CoPc(TIPS)<sub>8</sub> in an Ar-saturated NaOH electrolyte; (c) Comparison of the activity of different cobalt phthalocyanine catalysts; (d) Chemical structure of cobalt phthalocyanine molecules without TIPS protection groups.

the cobalt centers inside the molecules has no effect on the catalytic activity of the ORR. However, the catalytic activity of ORR can be improved, if analogue phthalocyanines without TIPS protection groups are used as catalysts. Figure 4.4 (d) shows the chemical structure of cobalt phthalocyanine (CoPc) without TIPS ligands that has been tested additionally as electrocatalyst for oxygen reduction. The corresponding polarization sweep of an gold electrode covered with CoPc catalysts is added as purple curve in figure 4.4 (c) and has the reduction peak around -0.2 V.

Such electrodes require almost 0.1 V lower overpotentials in order to drive the reduction of oxygen to H<sub>2</sub>O<sub>2</sub>. As it has been mentioned before, the interaction between cobalt and the underlying gold substrate is suggested to be quite strong [148, 149, 150]. The TIPS protection groups increase the distance between cobalt atoms and gold substrate, which is schematically illustrated in figure 4.5 (a). By removing the TIPS groups from the molecules, the distance to the gold substrate is drastically decreased and it is very likely that cobalt is in contact with the underlying gold substrate. This hypothesis is also supported by the XPS measurement and by previous XPS studies that observed a shift within XPS spectra, if the distance between cobalt centers and gold substrate is increased by multilayers [147]. This scenario is schematically drawn in figure 4.5 (b). It can be assumed that the distance between cobalt and gold substrate correlates with the electron transfer rate. By increasing the distance through TIPS groups, electron transfer is energetically less favorable, which ultimately lowers the catalytic activity. Higher overpotentials are required to overcome the barrier between cobalt and gold in order to enable oxygen reduction. By removing the TIPS groups from the molecular catalyst, cobalt atoms within the organic macrocycle are adsorbed on the gold surface (fig. 4.5 b), which facilitates electron transfer from gold towards the cobalt centers. Thereby the rate of electron transfer is increased and oxygen reduction can be performed at a lower overpotential.

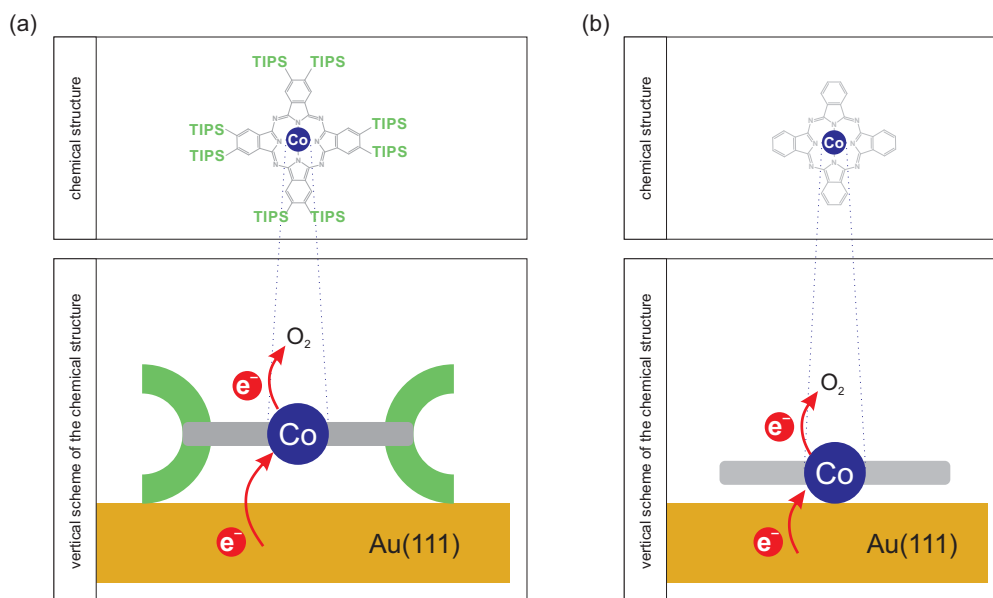


Figure 4.5 – Schematic illustration of the influence of TIPS groups attached to cobalt phthalocyanine catalysts: (a) Molecular catalysts equipped with TIPS ligand increase the distance of the cobalt atom from the surface; (b) Molecular catalysts without TIPS groups - cobalt center is most likely in contact with the underlying Au(111) substrate, which facilitates electron transfer through cobalt towards oxygen.

## 4.4 Summary

In this chapter cobalt atoms in phthalocyanines have been deposited on Au(111) electrodes and were used as single metal catalysts in order to improve the reduction of oxygen. Ambient STM and XPS confirmed molecule deposition and were used to characterize the electrode surfaces. It has been shown that the delocalized  $\pi$ -system has no significant effect on the catalytic activity, since the oxygen reduction to  $\text{H}_2\text{O}_2$  catalyzed by  $\text{Co}_2\text{Pc}_2(\text{TIPS})_{12}$  and  $\text{CoPc}(\text{TIPS})_8$  respectively, occurs at the same overpotential. However, the required overpotential can be decreased, if the distance between active sites (cobalt centers within phthalocyanines) and the underlying substrate is reduced. This has been shown by using cobalt phthalocyanines without any organic TIPS protection groups attached to the molecular catalyst. By doing so, it is very likely that electron transfer between Au(111) and cobalt atoms is facilitated and a lower overpotential is required in order to drive the ORR.

The results presented in this chapter deliver new engineering goals of molecular catalysts. A large developed  $\pi$ -system plays a minor role and shows no significant effect on the catalytic activity of oxygen reduction. It seems that minimizing the distance between organic component and underlying substrate enhances electron transport, which ultimately results in higher activities. However, such a mechanism is very likely and it would be ideal to complete this hypothesis with theoretical calculations and prove its validity.

## 5 Improving the Stability of Metal-Organic Hybrid Catalysts

The results that have been presented in this thesis so far, showed how molecular catalyst components influence the catalytic activity of different electrochemical reactions. The basic design of hybrid electrodes involves always a metallic substrate, which is Au(111) in this thesis and the deposition of molecular catalysts. They can be purely organic, like the polymers in chapter 3 or can involve metal atoms in their structure like the cobalt phthalocyanines in chapter 4. One of the key challenges by utilizing hybrid electrodes with molecular components is the stability. The molecules were always stabilized by rather weak interactions like van der Waals forces on the metal substrate and degradation phenomena were observed during catalysis. It has been previously reported that molecular components get distorted during catalytic reactions [20, 21] and long-term experiments performed in this thesis confirmed that molecules decompose and are removed from the substrate during catalysis. A major goal for future studies is to improve the stability of molecular components of the catalyst. One possibility is to replace the interaction type between metal substrate and molecular co-catalyst with a chemical covalent bond. This study is addressed by a joint project between the group of Doris Grumelli (Instituto de Investigaciones Fisicoquímicas Teóricas y Aplicadas - INIFTA) and our group at the Max Planck Institute for Solid State Research.

By using diazonium salts in a grafting process, metal or carbon electrodes can be functionalized by covalently tethered aryl groups [151, 152]. Such a procedure allows to decorate Au(111) electrodes with metalized porphyrins, which are bound in a perpendicular configuration on the electrode surface, graphically illustrated in figure 5.1 (a). The aryl groups of the porphyrin molecules are adapted by aryl diazonium salts in order to make them applicable for the grafting procedure. In addition, electrode surfaces are prepared with analogue porphyrin molecules in absence of covalent bonding between substrate and molecular catalyst. Due to their planar structure, they cover the surface in a flat configuration, which is shown in figure 5.1 (b). Both electrodes are tested for their ability to catalyze the ORR in order to investigate differences within the catalytic activity between perpendicular and flat configuration. Since the work presented in this chapter is still an ongoing project, the results should be regarded as preliminary rather than finally concluded.

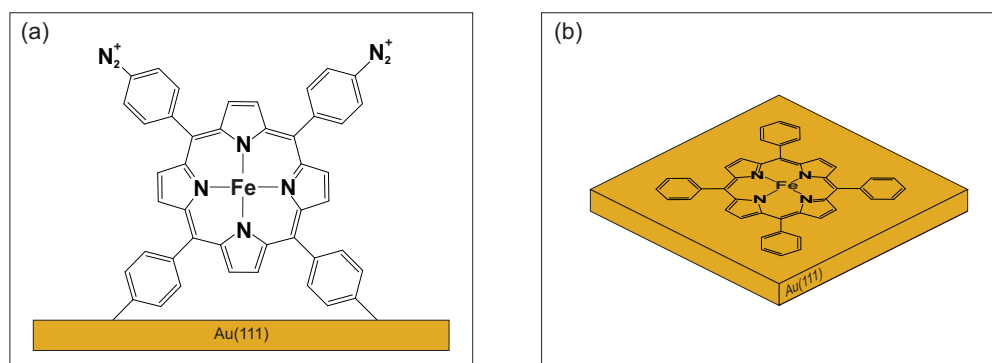


Figure 5.1 – Schematic configuration of the porphyrin molecules on the Au(111) surface: (a) Perpendicular configuration fabricated by electrografting; (b) Flat configuration, fabricated by epitaxy in UHV.

## 5.1 Fabrication of Hybrid Electrodes by Electrografting

The preparation of the perpendicular molecule configuration was carried out by Gerardo Ocampo (Instituto de Investigaciones Fisicoquímicas Teóricas y Aplicadas - INIFTA). The used molecules were 5,10,15,20-tetrakis-(4-diazophenyl)-porphyrin-rion(III) chloride (Fe-TDPP) that are equipped with four diazonium groups ( $\text{aryl}-\text{N}_2^+$ ). Electrografting is an electrochemical technique, which allows to bind organic molecules to a solid conducting surface [153]. The diazonium salts (Fe-TDPP) used in this project are reduced in a dediazonation reaction and form aryl radicals. During this reactions molecular nitrogen is released and the aryl radicals form a covalent bond with the underlying Au(111) electrode. It has to be mentioned that the release of nitrogen is not the only reaction mechanism and some molecules can be bound with the diazonium compound to the substrate [154, 155]. Molecular films were grafted according to the procedure reported in reference [156] by using a potential window between 0.5 and  $-0.35 \text{ V}_{\text{Ag}/\text{AgCl}}$  with a scan rate of  $0.1 \text{ V s}^{-1}$ . An electrolyte solution of acetonitrile - ACN ( $\text{N}\equiv\text{C}-\text{CH}_3$ ) and dimethylformamide - DMF ( $\text{H}-\text{CO}-\text{NH}_2$ ) is used (ACN:DMF = 4:1) containing 0.5 mM Fe-DTPP molecules. The corresponding reaction is schematically

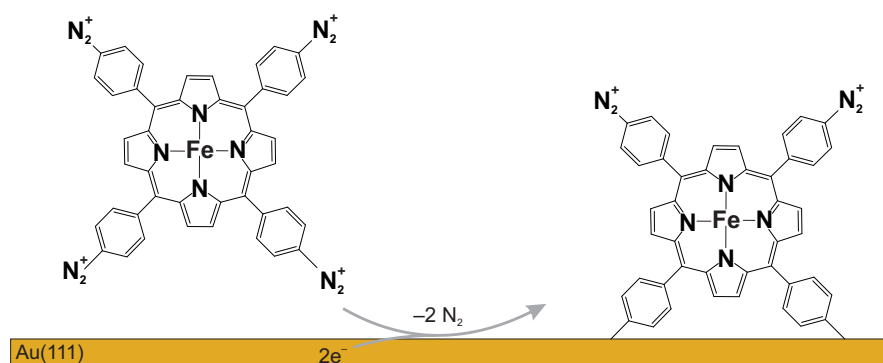


Figure 5.2 – Schematic illustration of the dediazonation reaction in order to form covalent bonds between Fe-TDPP molecules and Au(111).

## 5.1. Fabrication of Hybrid Electrodes by Electrografting

illustrated in figure 5.2. Since the dediazonation reaction creates aryl radicals, which are highly reactive chemical species, the reaction site for bond formations is rather imprecise. The radical molecules can be attached to either the gold substrate or to other molecules, which favors multilayer formation. In order to avoid the generation of multilayers, 5 mM 2,2-diphenyl-1-picrylhydrazyl (DPPH) is added during the grafting process [157]. Such radical scavengers inhibit undesired reaction products, such as the recombination of two aryl groups and facilitate the fabrication of thin films on the Au(111) electrode.

The hybrid electrodes fabricated by dediazonation were analyzed by atomic force microscopy (AFM) in order to determine the height of the molecular film. Figure 5.3 (a) shows a topographic image recorded by AFM. The central area was scratched by the AFM tip for profiling and the corresponding line scan is shown in figure 5.3 (b). By using the DPPH agent, it was possible to reduce the film thickness from 20 nm (without DPPH) down to 5 nm (with DPPH). Including size and binding geometry of the Fe-TDPP molecules, it is much likely that three molecular layers contribute to the 5 nm film thickness. However, it was possible to reach significant thinner films by including the DPPH agent during the electrografting process. The corresponding structure is illustrated in figure 5.3 (c). The aryl ligands of different molecules react with each other and form covalent bonds, which results in a 3D network that contains more than one layer. It has been reported that electrografting with nitrobenzenediazonium anions results in molecular films that can contain up to four or five layers at low DPPH concentrations [157]. By increasing the concentration of the radical scavenger, the film thickness can be lowered to a single monolayer. In order to reduce the film thickness below 5 nm, different DPPH concentrations up to 10 mM have been tested, which delivered similar results of the

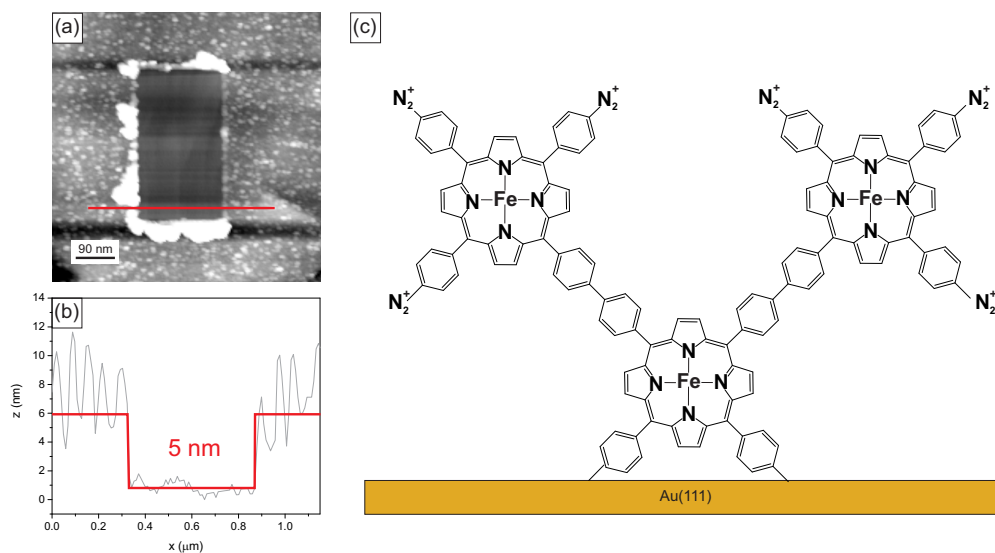


Figure 5.3 – Characterization of hybrid electrodes fabricated by electrografting: (a) Topographic image recorded by AFM with a central scratched area for profiling; (b) Line scan shows a film height of 5 nm, most likely due to the formation of multilayers; (c) Schematic model of multilayers growing during electrografting.



film thickness. However, increasing the concentration of the radical scavenger further results in the cleavage of the covalent bond between molecules and gold substrate and reveal large areas of the underlying Au(111) electrode. In addition, it has to be mentioned that molecules used in former studies contain only one diazonium ligand per molecule, while the amount of diazonium groups is four times higher in the Fe-TDPP molecules used in this project. It can be speculated that the high amount of diazonium ligands increases the reactivity significantly and makes the fabrication of single monolayers very unlikely.

### 5.2 Fabrication of Electrode Surfaces in UHV

Preparing electrodes with the flat molecule configuration (fig: 5.1 b) were prepared in an UHV chamber (base pressure:  $8 \times 10^{-10}$  mbar). The used substrate was a gold single crystal with a (111) orientation. Prior to molecule deposition, the Au(111) crystal was cleaned by repeated argon ion sputtering and annealing (825 K) cycles. The molecules that were used are 5,10,15,20-tetra(4-phenyl)21H,23H-porphyrin iron(III)chloride (FeTPP) and are commercially available (Sigma Aldrich). They were deposited by molecular beam epitaxy in an UHV chamber with a sublimation temperature of 620 K. Figure 5.4 shows a typical STM image of a gold electrode covered with self-assembled FeTPP molecules in the flat configuration as it is schematically illustrated in figure 5.1 (b). Additionally the chemical structure and the unit cell of the molecular monolayer is implemented. Like in case of the previously discussed phthalocyanines, the embedded iron centers act as catalytic active center. In the following section the decorated electrodes are tested for their ability to catalyze the ORR.

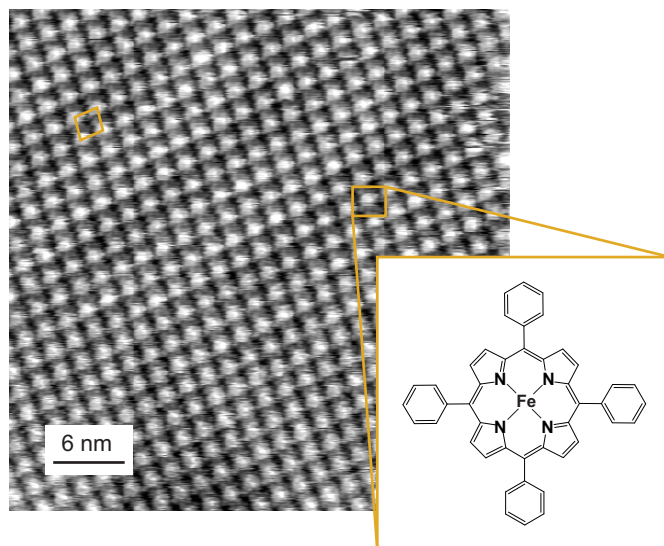


Figure 5.4 – STM image ( $U = -0.4$  V,  $I = 66$  pA) of an electrode surface covered with a monolayer of FeTPP molecules, including the unit cell and a scheme of a single molecule.



### 5.3 ORR with Hybrid Electrodes

Both electrodes presented in the previous sections are tested as electrocatalysts for oxygen reduction. By using iron atoms in a porphyrin matrix, oxygen is reduced via the direct  $4e^-$  pathway [158]. The linear scans in figure 5.5 show the reduction of oxygen to water according to equation 1.14: The purple curve in figure 5.5 (a) corresponds to an electrode covered with molecules in the orthogonal configuration (fig: 5.1 a), which are prepared by electrografting and reveals the ORR peak at an overpotential around  $-0.56\text{ V}_{\text{Ag}/\text{AgCl}}$ . The green polarization curve in figure 5.5 represents ORR catalyzed by an electrode prepared in UHV with molecules adsorbed in the flat configuration, like it is shown in the STM image of figure 5.4. The corresponding ORR peak occurs around  $-0.23\text{ V}_{\text{Ag}/\text{AgCl}}$ .

The polarization curves presented in figure 5.5 (a) and (b) are remarkably different and the electrode fabricated by electrografting reveals a lower ORR activity. However a direct comparison at the current point has no value, since electrode fabrication by electrografting needs to be further optimized. The AFM results point towards molecular trilayers deposited on Au(111) rather than a monolayer. In addition it can be assumed that the DPPH agent removed parts of the molecular film and certain areas of the underlying gold substrate is revealed during oxygen reduction.

At this point it can be speculated that grafted electrodes with perpendicular coordinated molecules will reach lower activities compared to electrodes with the flat molecule configuration prepared in UHV. Underlying reason are large distances between iron centers and gold substrate, which lower the catalytic activity and shift oxygen reduction to higher overpotentials (as it was explained in chapter 4). In the flat configuration, the iron centers are most likely in contact with the underlying gold substrate, which facilitates electron transfer from the gold substrate through the iron center towards oxygen molecules (similar mechanism according to fig. 4.5). Additionally the iron atoms in grafted hybrid electrodes are entirely surrounded by

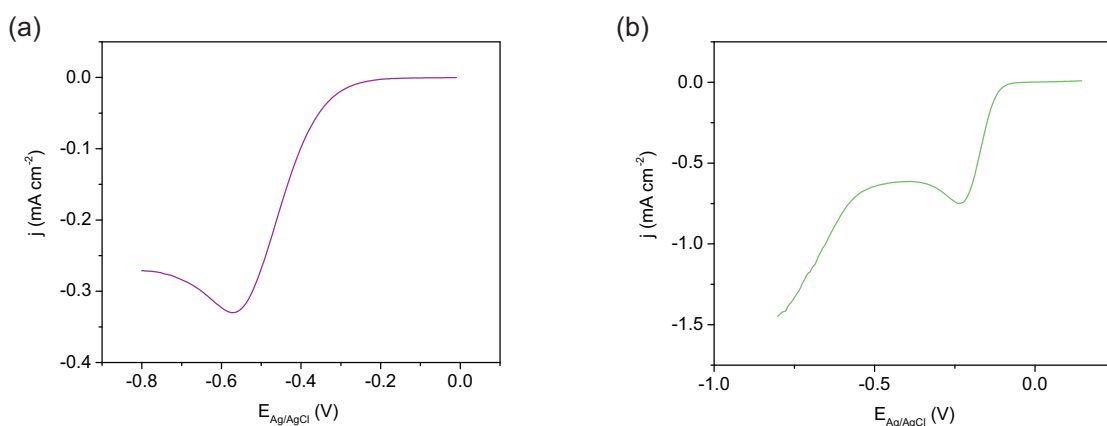


Figure 5.5 – ORR on hybrid electrodes in 0.1 M NaOH solution (O<sub>2</sub> saturated) at 50 mV s<sup>-1</sup>: (a) ORR with electrografted electrode - perpendicular configuration of molecular components; (b) ORR with UHV fabricated electrode - flat configuration of molecular components.

organic material and have no direct access to reactants, which can affect the catalytic activity of the reaction. However, it can be expected that the stability of such electrodes is significantly increased by the covalent bond and the metal-organic film on the Au(111) electrode is stable for several cycles. The trade-off between activity and stability has to be encountered in order to fabricate new improved types of electrocatalysts. This compromise can be optimized by maximizing the coverage during the electrografting procedure and fabricate hybrid catalysts that are entirely covered by an organic film.

### 5.4 Future Perspective

It has been shown that preparing gold electrodes by electrografting results in the formation of multilayers, most likely due to the large number of diazonium ligands present in the Fe-TDPP molecules. In order to minimize the reactivity during the electrografting process, a different precursor molecule will be tested, which has only one diazonium group implemented in its organic structure. First experiments with such molecules resulted in the denaturation of the precursor molecules during the grafting procedure, presumably induced by the iron center. In order to minimize undesired interactions, an unmetallized porphyrin molecule with a single diazonium ligand will be used. The corresponding chemical structure is shown on the right side in figure 5.6. Once these molecules cover the Au(111) surface, they will be metallized in a second reaction step. The entire fabrication procedure is graphically illustrated in figure 5.6: It involves electrografting with an empty porphyrin molecule and metallation will be performed, once the molecule is grafted onto the Au(111) substrate.

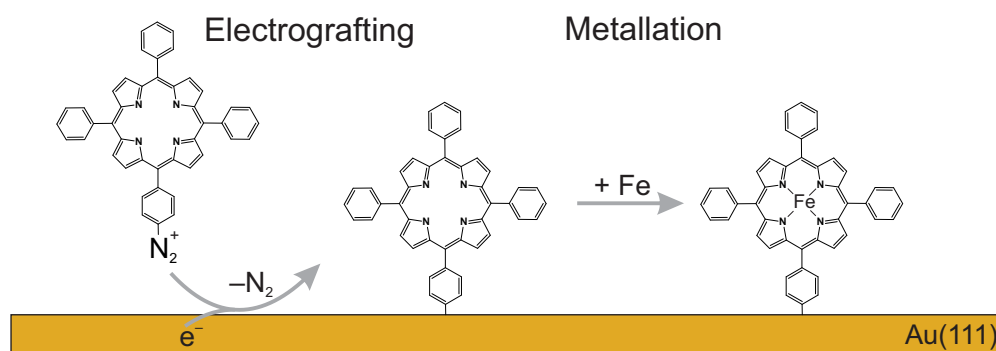


Figure 5.6 – Future plan for fabricating monolayers by electrografting: Metal free precursor molecules with one diazonium ligand are grafted to the electrode surface and metallized in a second step, while the molecules are attached to the substrate by covalent bonds.

### 5.5 Summary

This chapter addressed the stability of metal electrodes, which are decorated with metal-organic components by strengthening the interaction between molecules and underlying substrate. Electrografting allows to build covalent chemical bonds between the metal-organic catalysts and the Au(111) substrate. Fabricating such electrodes was successful, however

the fabrication of single monolayers remains challenging. By including a radical scavenger during the grafting process, the thickness of the organic film was reduced from 20 nm down to 5 nm, which presumably corresponds to trilayers on the Au(111) surface. Since the increase of the DPPH concentration delivered similar results, a different precursor molecule with a single diazonium ligand will be tested. In order to avoid undesired interactions with the metal center, an empty porphyrin will be grafted to the electrode surface and metallized in a second step. In addition, electrodes have been fabricated in UHV with metallized FeTPP molecules, which are deposited in a flat configuration, in order to investigate how the configuration of the molecular components affects the catalytic activity of the ORR. The results so far point towards lower activities of the electrodes fabricated by electrografting, however the final results remain unanswered until a single monolayer is fabricated. The trade-off between activity and stability can be optimized by maximizing the film coverage during the electrografting process. Once the procedure is successful, we can introduce a powerful way of fabricating stable metal-organic hybrid catalysts that can be adapted to different catalytic reactions by the metallation with various transition metals.



## 6 Conclusion

The scientific contribution of this thesis focuses on nanoscale engineering and design principles for fabricating novel electrode surfaces for electrocatalysis. The design of suitable catalyst surfaces remains a challenging task even today. Although much is known about the detailed mechanism of important technological reactions like HER or ORR on a catalyst surface, there still remains much work to find all reaction steps as a function of catalyst, electrolyte, pH, etc. Relevant reaction steps have to be investigated on the molecular level in order to fabricate optimal catalyst surfaces for specific electrochemical reactions. This work sheds light on the catalyst's structure at the atomic level, without which such detailed studies of reaction steps are not possible.

The material-by-design approach, which has been used throughout this thesis includes also the characterization of novel catalyst surfaces. Statistical analysis and MD simulations were used to characterize organic components that can be included in electrocatalysts. The analysis is focused on ring size distribution and short range correlations that are described by neighboring ring size combinations. The nitrogen free polymer ( $P-N_0$ ) reveals a good agreement of the experimental ring size distribution and the corresponding MD simulation. Additionally, the distribution of neighboring rings shows an overall resemblance and highlights the successful mimicry of the  $P-N_0$  polymer by the simulation. The structure reveals spatial correlations on short length scales, due to energy penalties in certain neighboring ring size combinations in order to guarantee a planar network. Similar short range correlations are absent in the system that contains nitrogen hetero atom ( $P-N_3$ ) and defects can be implemented at lower energy penalties. The structural exchange of C–H by nitrogen makes the network less susceptible for steric conflicts, which arise by hydrogen interactions and provide a higher defect tolerance in the network. The resulting polymer is more likely to form mosaic structures that tessellate in a random order on the surface. A detailed comprehension of metal surfaces decorated with organic components is crucial, if such devices are used as electrocatalysts. Since electrode surfaces reveal often a complex structure in order to enhance catalytic reactions, the combination of MD simulations and experimental data provides an adequate method to characterize spatial correlations and optimize the design of novel electrode surfaces for electrocatalysis.

Nanoscale engineering in UHV was used to fabricate specific electrodes with organic co-catalysts in order to enhance the HER. Au(111) electrodes were decorated via polymer fabrication using three different types of organic components: Precursor molecules without nitrogen  $P-N_0$ , with three nitrogen atoms  $P-N_3$  and with six nitrogen atoms  $P-N_6$ . The characterization of the electrochemical active surface area (ECSA) of the hybrid electrodes showed no significant increase of the surface roughness compared to the ECSA of a blank Au(111) electrode and proved the flatness of the fabricated hybrid electrodes. The molecular networks of the co-catalysts provide well defined docking sites for reactants and reaction intermediates during hydrogen evolution. Nitrogen atoms in co-catalysts increase the binding energy and the residence time by forming hydrogen bonds. However, it was shown that the amount and location of nitrogen atoms in the network is crucial. Two nitrogen atoms at active sites ( $P-N_6$ ) increase the binding energy above an optimal value and reaction intermediates block the active sites of the catalyst. In addition, the local structural environment of the catalytic active sites affects the binding geometry of reactants to the co-catalyst. Hybrid electrodes with  $P-N_0$  and  $P-N_3$  facilitate the cleavage of the H–OH bond by overlapping the antibonding states of water with the electronic states of the Au(111) substrate, which is absent in electrodes that are combined with the  $P-N_6$  co-catalyst. In addition, the fabricated hybrid electrodes were tested as electrocatalysts for the ORR. The molecular network did not improve the ORR activity, likely because oxygen has no dipole momentum like water molecules and stabilization by hydrogen bridges does not occur. The enhancement of oxygen reduction requires different precursor molecules for the fabrication of organic co-catalysts. The results highlight the importance of metal electrodes combined with organic components for electrocatalysis. The binding energy between reactants and electrode surface can be perfected by adding suitable sites into precursor molecules that build up the organic co-catalyst. They act as docking sites and optimize the residence time of reactants and intermediates on the electrode surface. The structure as well as the chemistry of organic co-catalysts depends strongly on the electrochemical reaction and has to be adapted in order to obtain the best turnover. These results provide a new method of improving electrocatalytic reactions by combining earth abundant transition metals with specific engineered organic co-catalysts.

In order to gain further insight into the requirements of organic catalyst components different cobalt phthalocyanines on Au(111) were used as electrocatalysts for the ORR. The delocalized  $\pi$ -system has no significant impact on the catalytic activity. Single cobalt phthalocyanine molecules reach similar catalytic activities compared to fused phthalocyanines that are roughly doubled in size. However, both molecules were equipped with TIPS protection groups, which are used during organic synthesis in order to inhibit undesired side reactions. Such molecular ligands reveal a 3D non-planar structure and slightly lift the catalytic active cobalt atoms from the underlying Au(111) substrate. A corresponding phthalocyanine version without such TIPS groups can catalyze the reduction of oxygen at slightly lower overpotentials, most likely since the cobalt atoms are directly in contact with the gold electrode, which facilitates electron transport from gold through cobalt towards oxygen. These results show that a minimized distance between cobalt atoms and the electron donor is highly important, while the size of

---

the organic  $\pi$ -system can be neglected. These two aspects should be considered, if future catalysts with organic components are fabricated.

The final aspect in molecular engineering is the stability of organic catalyst components, which usually limits the application of organic/inorganic catalysts on a larger time scale. In order to address the problem of stability, hybrid electrodes are fabricated by electrografting, an electrochemical procedure that enables covalent bonding between molecules and metal electrodes. For this purpose, iron porphyrin molecules with diazonium ligands are used. During a dediazonation reaction, molecular nitrogen is released and aryl radicals are formed, which create a covalent bond with atoms from a gold electrode. At the current point, the film thickness could be reduced to 5 nm by the aid of a radical scavenger (DPPH), which inhibits undesired reaction like the formation of aryl–aryl bonds that results in the formation of multilayers. Including structure and binding geometry of the molecules that build up the film on the electrode, 5 nm corresponds most likely to a molecular trilayer. In order to fabricate hybrid electrodes with a monolayer, different precursor molecules with a single diazonium ligand will be tested in future experiments. It can be assumed that lower amounts of diazonium ligands decrease the reactivity of aryl–aryl bond formation significantly. Empty porphyrin molecules will act as precursor molecules, in order to avoid interactions with the metal center during the grafting process. Once the molecules are bound to the gold electrode, metallation will be performed in a second step. The grafting of porphyrins results in an orthogonal configuration of the molecular components with respect to Au(111) and the iron centers of the porphyrins are separated from the gold substrate. In addition electrodes were fabricated in UHV and molecules are adsorbed in a flat geometry on the gold surface, which results in a direct contact between iron atoms inside the porphyrins and the underlying Au(111) substrate. The results so far point towards lower catalytic activities of the electrografted hybrid electrodes, however a final conclusion has to be postponed until monolayers can be fabricated. It has to be mentioned that higher concentrations of the radical scavenger, which is used during electrografting, can cleave the bonds between gold electrode and molecular components. Consequently, hybrid electrodes fabricated by electrografting will reveal blank gold areas, which are not covered by molecules. This aspect will be addressed by a quartz crystal micro balance in order to determine the amount of molecules that are deposited on the gold electrode. Succeeding in this procedure will provide a powerful technique of fabricating stable organic/inorganic electrodes for electrocatalysis. The empty porphyrin molecules can be adapted to various electrochemical reactions by metallation with the required metal center.





## 7 Outlook

The electrochemical reactions that were investigated throughout this thesis are the HER and ORR, which have a key function for the technological water cycle. Another important reaction in order to move towards environmental friendly energy is the reduction of  $\text{CO}_2$  and the generation of carbon based fuels. Compared to fuels for the conventional water based fuel cell, carbon-based fuels can appear as liquids at standard condition. This facilitates transportation and is the reason why they are preferred over gaseous fuels, which require additional energy for compression [159].

Since various products can appear during  $\text{CO}_2$  reduction [160], catalysts need to be selective in order to generate the desired product, which is one of the major challenges in the investigation of this reaction. Future studies should address this challenge by utilizing molecular components and design principles that were introduced in this thesis to fabricate suitable catalyst surfaces for  $\text{CO}_2$  reduction. Since it was shown that molecular components can be specifically designed in order to increase the catalytic activity, similar results can be achieved by synthesizing precursor molecules, which promote specific product formation during the reduction of  $\text{CO}_2$ .

Various metals have been tested as catalysts and were able to reduce  $\text{CO}_2$  to formate ( $\text{HCOO}^-$ ) or CO. Catalysts with a high turnover towards formate are not capable to break the C–O bond and are therefore poor catalysts for reducing  $\text{CO}_2$ . The reaction to CO is preferred, since CO can be further reduced and form various hydrocarbons that can be used as fuels. However, the production of sufficient CO amounts is diminished by low binding energies between CO and metal substrate, which results in the desorption of CO [161, 162]. Increasing the overpotential was not able to solve the problem and revealed hydrogen as dominant product, since  $\text{CO}_2$  reduction competes with hydrogen evolution [161]. Whereas most catalysts have the final reaction step in the production of CO, copper is able to reduce CO further and produces various hydrocarbons, such as methane, methanol or ethylene [160, 163]. Combining copper with materials that show a high current efficiency in the  $\text{CO}_2$  to CO reduction is a promising approach in order to fabricate novel electrode surfaces that support the reduction of  $\text{CO}_2$  towards carbon based fuels.

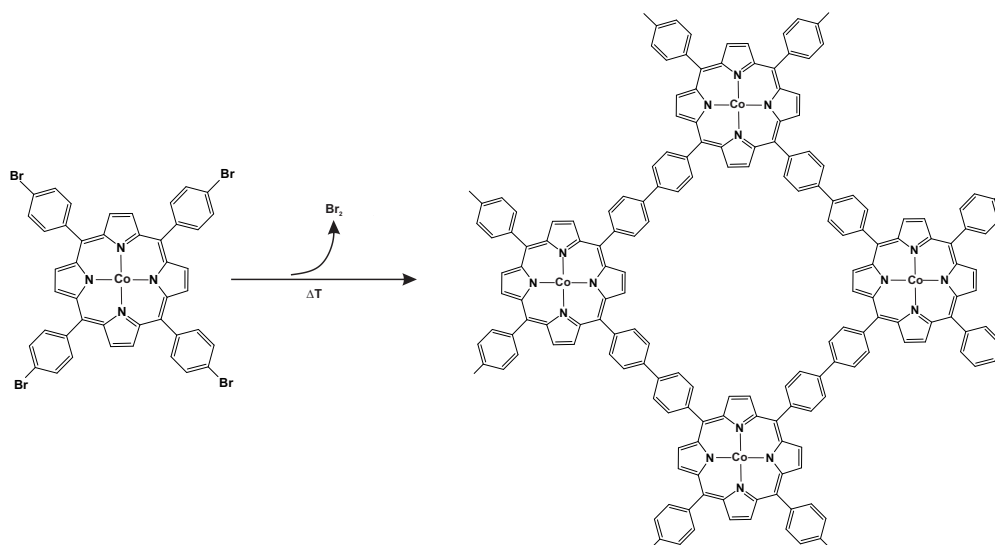


Figure 7.1 – Schematic reaction for fabricating 2D polymers from brominated cobalt porphyrins, which can act as catalysts for  $\text{CO}_2$  reduction.

Studies that include molecular components in the reduction of  $\text{CO}_2$  revealed cobalt porphyrins as active catalysts for  $\text{CO}_2$  to CO reduction [139, 164]. In the light of the results achieved in this thesis, brominated cobalt porphyrins can be used in order to fabricate 2D metal organic polymers on copper substrates (similar to **chapter 3**). The schematic reaction is illustrated in figure 7.1. The cobalt centers within the polymer are capable to create high concentrations of CO close to the copper electrode surface, while the cavities that expose the underlying copper substrate act as active site for the reduction of CO to hydrocarbons. The advantage of such electrode surfaces is their planarity, which enables the characterization by surface techniques like STM and XPS. The electrode surface can be analyzed before and after  $\text{CO}_2$  reduction experiments and helps to identify the active sites of the fabricated electrode surface.

A different approach for designing electrode surfaces for  $\text{CO}_2$  reduction provides the electrografting method, which was presented in **chapter 5**. Cobalt porphyrin molecules with a single diazonium group can be attached to a copper surface. Full coverage monolayers are not required for  $\text{CO}_2$  reduction and the revealed areas of the underlying metal substrate due to the inclusion of a radical scavenger (DPPH) are beneficial. In analogy of the hybrid electrode described above, the cobalt centers within the porphyrins are used to reduce  $\text{CO}_2$  to CO and create concentrations of CO close to the electrode surface. In a second step the underlying copper substrate is capable to reduce CO further and produce different types of hydrocarbons. The optimal mechanism is schematically shown in figure 7.2.

It has to be mentioned that the experimental set-up requires gas chromatography, in order to investigate the different products of the  $\text{CO}_2$  reduction reaction. They can be extracted from the electrochemical cell with a syringe and injected into the gas chromatograph. This procedure requires an electrochemical cell with a very small volume, otherwise the concentration

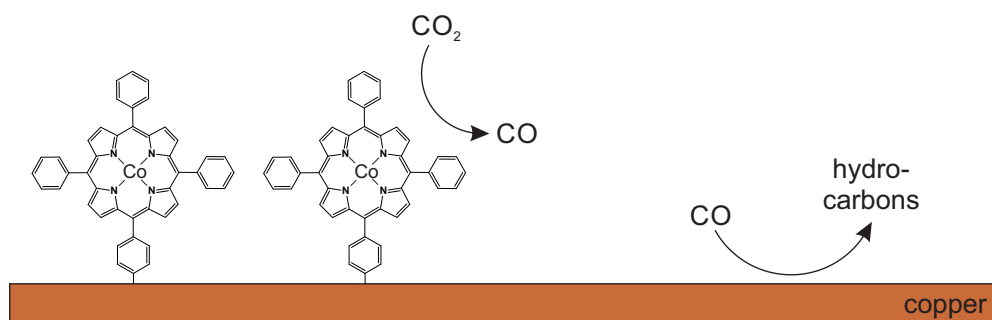


Figure 7.2 – Schematic illustration of CO<sub>2</sub> reduction on electrografted hybrid electrodes: CO formation at cobalt porphyrins ensures a high CO concentration at the surface, which can be further reduced to hydrocarbons by the copper substrate.

of gas products might be too low for detection by the gas chromatograph. Moving entirely to the investigation of electrode surfaces that act as electrocatalysts for CO<sub>2</sub> reduction demands modifications on the experimental set up. The electrochemical cell requires two compartments, which separates working- and counter electrode by an anion exchange membrane [160, 165]. This design avoids that hydrocarbons produced at the working electrode react at the counter electrode and falsify the quantification of the products. Preliminary experiments can be performed with a conventional electrochemical cell and a syringe (fig. 7.3 a), however future investigations should involve a flow cell system (fig. 7.3 b). In such set-ups, the electrolyte solution flows continuously over the sample surface. The flow cell system can be directly connected with the gas chromatograph and avoids sample losses during the extraction and injection with the syringe.

Modifying the UHV-transfer system that has been used in this thesis with a gas chromatograph and a flow cell system, enables various new sophisticated experiments that can deliver new insight into electrochemical reactions on the molecular and the atomic scale.

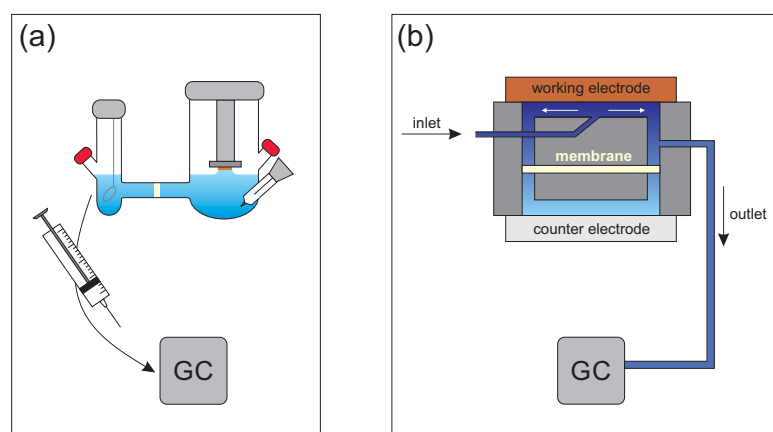


Figure 7.3 – Set up comparison of the electrochemical cell and the gas chromatograph (GC): (a) Conventional cell, transfer to gas chromatograph by syringe; (b) Flow cell with direct connection to the gas chromatograph.



# Acknowledgements

It has been a long journey through the past years until this final version of the thesis has been finished. The time of a Ph.D. is dominated by frustration, failure until success kicks in and my time was no different. However, it is important to mention that the final stage of success could never been achieved without the help and support of many people.

I have to mention Prof. Klaus Kern for being my thesis director. I would like to thank Prof. Anna Fontcuberta i Morral for being my jury president and Prof. Aleksandra Radenovic, Prof. Kristina Tschulik and Prof. Sebastian Stepanow for reviewing my scientific work and being part of my jury. Additionally, I want to thank Prof. Christian Schön. Prof. Christina Oligschleger, Prof. Heriberto F. Busnengo, Dr. Paula Abufager and Juan M. Lombardi for providing theoretical calculations. Without their support the scientific work presented in this thesis would never reached a significant impact.

Special thanks go to my supervisor Dr. Rico Gutzler for his daily support. Without him my two publications would have never been published and without his help this thesis would never reached this level. I also greatly benefited from his knowledge and understanding about STM and XPS, which were essential for our work. I can confidently say that the two of us make now a pretty good team. The successful maintenance of the laboratory on the campus in Stuttgart could never been performed so smoothly without the support of Wolfgang Stiepany, Peter Andler and Marko Memmler. Thank you for all your immediate support at any time. But no results in this thesis could be achieved without Dr. Doris Grumelli. There are no words to describe how thankful I am to you for the time you spend to teach me electrochemistry, for your scientific input, the countless moments you kept me motivated and your emotional support in-and outside the institute. I was grateful to have a colleague like and now I am thankful from the bottom of my heart to have a friend like you.

My office mates Katharina Polyudov, Piotr Kot and Dr. Andreas Topp deserve also a special recognition: Special thanks to Andy, because without him this thesis would not be existent, because I would NEVER be able to write anything in Latex. Also your commitment to support me, by proofreading parts of my thesis in the bathtub deserves to be mentioned. All the three of you together with Ina and Pete helped me through many "kurwa" moments. I truly admire your combination very much, since everyone of us has a different personality and we complement each other very well. I hope we will continue to spend time together, whether

## Acknowledgements

---

during playing Sing Star or just enjoying some cookies.

There are many people outside the institute who supported me in many ways, like Ludovic Dumas, who help me with the French translation of the abstract or Dr. Martina Greiner, who kept me positive during the last months. Finally I want to thank my parents Erika and Michael Alexa, who supported me through my entire life and gave me all the love and freedom to evolve in my own particular way. Thank you for being the best parents in the world.

*Stuttgart, September 25, 2020*

P. A.

## Bibliography

- [1] D. Hötger, P. Abufager, C. Morchutt, P. Alexa, D. Grumelli, J. Dreiser, S. Stepanow, P. Gambardella, H. F. Busnengo, M. Etzkorn, R. Gutzler, and K. Klaus, “On-surface transmetalation of metalloporphyrins,” *Nanoscale*, vol. 10, no. 45, pp. 21116–21122, 2018.
- [2] P. Alexa, C. Oligschleger, P. Gröger, C. Morchutt, V. Vyas, B. V. Lotsch, J. C. Schön, R. Gutzler, and K. Kern, “Short-range structural correlations in amorphous 2D polymers,” *ChemPhysChem*, vol. 20, no. 18, pp. 2340–2347, 2019.
- [3] P. Alexa, J. M. Lombardi, P. Abufager, H. F. Busnengo, D. Grumelli, V. S. Vyas, F. Haase, B. V. Lotsch, R. Gutzler, and K. Kern, “Enhancing hydrogen evolution activity of Au (111) in alkaline media through molecular engineering of a 2D polymer,” *Angewandte Chemie International Edition*, vol. 59, no. 22, pp. 8411–8415, 2020.
- [4] Z. W. Seh, J. Kibsgaard, C. F. Dickens, I. Chorkendorff, J. K. Nørskov, and T. F. Jaramillo, “Combining theory and experiment in electrocatalysis: Insights into materials design,” *Science*, vol. 355, no. 6321, pp. 1–12, 2017.
- [5] J. Emmert, M. Stevens, P. Bernath, D. Drob, and C. Boone, “Observations of increasing carbon dioxide concentration in Earth’s thermosphere,” *Nature Geoscience*, vol. 5, no. 12, pp. 868–871, 2012.
- [6] C. Baes, H. Goeller, J. Olson, and R. Rotty, “Carbon Dioxide and Climate: The Uncontrolled Experiment: Possibly severe consequences of growing CO<sub>2</sub> release from fossil fuels require a much better understanding of the carbon cycle, climate change, and the resulting impacts on the atmosphere,” *American Scientist*, vol. 65, no. 3, pp. 310–320, 1977.
- [7] G. S. Callendar, “The artificial production of carbon dioxide and its influence on temperature,” *Quarterly Journal of the Royal Meteorological Society*, vol. 64, no. 275, pp. 223–240, 1938.
- [8] C. D. Keeling, “The concentration and isotopic abundances of carbon dioxide in the atmosphere,” *Tellus*, vol. 12, no. 2, pp. 200–203, 1960.
- [9] G. M. Whitesides and G. W. Crabtree, “Don’t forget long-term fundamental research in energy,” *Science*, vol. 315, no. 5813, pp. 796–798, 2007.

## Bibliography

---

- [10] H. A. Gasteiger, S. S. Kocha, B. Sompalli, and F. T. Wagner, "Activity benchmarks and requirements for Pt, Pt-alloy, and non-Pt oxygen reduction catalysts for PEMFCs," *Applied Catalysis B: Environmental*, vol. 56, no. 1-2, pp. 9–35, 2005.
- [11] S. B. Adler, "Factors governing oxygen reduction in solid oxide fuel cell cathodes," *Chemical Reviews*, vol. 104, no. 10, pp. 4791–4844, 2004.
- [12] Y. P. Zhu, C. Guo, Y. Zheng, and S.-Z. Qiao, "Surface and interface engineering of noble-metal-free electrocatalysts for efficient energy conversion processes," *Accounts of Chemical Research*, vol. 50, no. 4, pp. 915–923, 2017.
- [13] N. M. Markovic, H. A. Gasteiger, and P. N. Ross, "Oxygen reduction on platinum low-index single-crystal surfaces in alkaline solution: Rotating ring disk Pt (hkl) studies," *The Journal of Physical Chemistry*, vol. 100, no. 16, pp. 6715–6721, 1996.
- [14] N. M. Marković, S. T. Sarraf, H. A. Gasteiger, and P. N. Ross, "Hydrogen electrochemistry on platinum low-index single-crystal surfaces in alkaline solution," *Journal of the Chemical Society, Faraday Transactions*, vol. 92, no. 20, pp. 3719–3725, 1996.
- [15] N. Markovic, H. Gasteiger, and P. N. Ross, "Kinetics of oxygen reduction on Pt (hkl) electrodes: Implications for the crystallite size effect with supported Pt electrocatalysts," *Journal of the Electrochemical Society*, vol. 144, no. 5, pp. 1591–1597, 1997.
- [16] A. Chen and P. Holt-Hindle, "Platinum-based nanostructured materials: Synthesis, properties, and applications," *Chemical Reviews*, vol. 110, no. 6, pp. 3767–3804, 2010.
- [17] H. A. Gasteiger and N. M. Marković, "Just a dream – or future reality?," *Science*, vol. 324, no. 5923, pp. 48–49, 2009.
- [18] Y. Gorlin and T. F. Jaramillo, "A bifunctional nonprecious metal catalyst for oxygen reduction and water oxidation," *Journal of the American Chemical Society*, vol. 132, no. 39, pp. 13612–13614, 2010.
- [19] U. Paulus, A. Wokaun, G. Scherer, T. Schmidt, V. Stamenkovic, V. Radmilovic, N. Markovic, and P. Ross, "Oxygen reduction on carbon-supported Pt-Ni and Pt-Co alloy catalysts," *The Journal of Physical Chemistry B*, vol. 106, no. 16, pp. 4181–4191, 2002.
- [20] B. Wurster, D. Grumelli, D. Hötger, R. Gutzler, and K. Kern, "Driving the oxygen evolution reaction by nonlinear cooperativity in bimetallic coordination catalysts," *Journal of the American Chemical Society*, vol. 138, no. 11, pp. 3623–3626, 2016.
- [21] D. Grumelli, B. Wurster, S. Stepanow, and K. Kern, "Bio-inspired nanocatalysts for the oxygen reduction reaction," *Nature Communications*, vol. 4, no. 1, pp. 1–6, 2013.
- [22] X.-F. Yang, A. Wang, B. Qiao, J. Li, J. Liu, and T. Zhang, "Single-atom catalysts: A new frontier in heterogeneous catalysis," *Accounts of Chemical Research*, vol. 46, no. 8, pp. 1740–1748, 2013.



- [23] J. M. Gottfried, "Surface chemistry of porphyrins and phthalocyanines," *Surface Science Reports*, vol. 70, no. 3, pp. 259–379, 2015.
- [24] W. Auwärter, D. Écija, F. Klappenberger, and J. V. Barth, "Porphyrins at interfaces," *Nature Chemistry*, vol. 7, no. 2, pp. 105–120, 2015.
- [25] N. Cheng, C. Kemna, S. Goubert-Renaudin, and A. Wieckowski, "Reduction reaction by porphyrin-based catalysts for fuel cells," *Electrocatalysis*, vol. 3, no. 3-4, pp. 238–251, 2012.
- [26] G. F. Manbeck and E. Fujita, "A review of iron and cobalt porphyrins, phthalocyanines and related complexes for electrochemical and photochemical reduction of carbon dioxide," *Journal of Porphyrins and Phthalocyanines*, vol. 19, no. 1–3, pp. 45–64, 2015.
- [27] B. J. Holliday and C. A. Mirkin, "Strategies for the construction of supramolecular compounds through coordination chemistry," *Angewandte Chemie International Edition*, vol. 40, no. 11, pp. 2022–2043, 2001.
- [28] J. V. Barth, G. Costantini, and K. Kern, "Engineering atomic and molecular nanostructures at surfaces," *Nature*, vol. 437, pp. 671–679, 2005.
- [29] L. Bartels, "Tailoring molecular layers at metal surfaces," *Nature Chemistry*, vol. 2, no. 2, pp. 87–95, 2010.
- [30] C. Hu and L. Dai, "Carbon-based metal-free catalysts for electrocatalysis beyond the ORR," *Angewandte Chemie International Edition*, vol. 55, no. 39, pp. 11736–11758, 2016.
- [31] L. Dai, Y. Xue, L. Qu, H.-J. Choi, and J.-B. Baek, "Metal-free catalysts for oxygen reduction reaction," *Chemical Reviews*, vol. 115, no. 11, pp. 4823–4892, 2015.
- [32] L. Yang, S. Jiang, Y. Zhao, L. Zhu, S. Chen, X. Wang, Q. Wu, J. Ma, Y. Ma, and Z. Hu, "Boron-doped carbon nanotubes as metal-free electrocatalysts for the oxygen reduction reaction," *Angewandte Chemie International Edition*, vol. 50, no. 31, pp. 7132–7135, 2011.
- [33] H. Fei, R. Ye, G. Ye, Y. Gong, Z. Peng, X. Fan, E. L. Samuel, P. M. Ajayan, and J. M. Tour, "Boron-and nitrogen-doped graphene quantum dots/graphene hybrid nanoplatelets as efficient electrocatalysts for oxygen reduction," *ACS nano*, vol. 8, no. 10, pp. 10837–10843, 2014.
- [34] F. Razmjooei, K. P. Singh, M. Y. Song, and J.-S. Yu, "Enhanced electrocatalytic activity due to additional phosphorous doping in nitrogen and sulfur-doped graphene: A comprehensive study," *Carbon*, vol. 78, pp. 257–267, 2014.
- [35] V. Perazzolo, C. Durante, R. Pilot, A. Paduano, J. Zheng, G. A. Rizzi, A. Martucci, G. Granozzi, and A. Gennaro, "Nitrogen and sulfur doped mesoporous carbon as metal-free electrocatalysts for the in situ production of hydrogen peroxide," *Carbon*, vol. 95, pp. 949–963, 2015.

- [36] X. Yu, P. Han, Z. Wei, L. Huang, Z. Gu, S. Peng, J. Ma, and G. Zheng, "Boron-doped graphene for electrocatalytic  $N_2$  reduction," *Joule*, vol. 2, no. 8, pp. 1610–1622, 2018.
- [37] V. S. Vyas, F. Haase, L. Stegbauer, G. Savasci, F. Podjaski, C. Ochsenfeld, and B. V. Lotsch, "A tunable azine covalent organic framework platform for visible light-induced hydrogen generation," *Nature Communications*, vol. 6, no. 1, pp. 1–9, 2015.
- [38] Y. Yang, Z. Lun, G. Xia, F. Zheng, M. He, and Q. Chen, "Non-precious alloy encapsulated in nitrogen-doped graphene layers derived from MOFs as an active and durable hydrogen evolution reaction catalyst," *Energy & Environmental Science*, vol. 8, no. 12, pp. 3563–3571, 2015.
- [39] Y. Ito, W. Cong, T. Fujita, Z. Tang, and M. Chen, "High catalytic activity of nitrogen and sulfur Co-doped nanoporous graphene in the hydrogen evolution reaction," *Angewandte Chemie*, vol. 127, no. 7, pp. 2159–2164, 2015.
- [40] L. Scudiero, D. E. Barlow, U. Mazur, and K. Hipps, "Scanning tunneling microscopy, orbital-mediated tunneling spectroscopy, and ultraviolet photoelectron spectroscopy of metal (II) tetraphenylporphyrins deposited from vapor," *Journal of the American Chemical Society*, vol. 123, no. 17, pp. 4073–4080, 2001.
- [41] L. Scudiero, D. E. Barlow, and K. Hipps, "Scanning tunneling microscopy, orbital-mediated tunneling spectroscopy, and ultraviolet photoelectron spectroscopy of nickel (II) octaethylporphyrin deposited from vapor," *The Journal of Physical Chemistry B*, vol. 106, no. 5, pp. 996–1003, 2002.
- [42] D. E. Barlow, L. Scudiero, and K. Hipps, "Scanning tunneling microscopy study of the structure and orbital-mediated tunneling spectra of cobalt (II) phthalocyanine and cobalt (II) tetraphenylporphyrin on Au (111): Mixed composition films," *Langmuir*, vol. 20, no. 11, pp. 4413–4421, 2004.
- [43] A. Weber-Bargioni, J. Reichert, A. Seitsonen, W. Auwärter, A. Schiffrin, and J. Barth, "Interaction of cerium atoms with surface-anchored porphyrin molecules," *The Journal of Physical Chemistry C*, vol. 112, no. 10, pp. 3453–3455, 2008.
- [44] F. Buchner, K. Flechtner, Y. Bai, E. Zillner, I. Kellner, H.-P. Steinrück, H. Marbach, and J. M. Gottfried, "Coordination of iron atoms by tetraphenylporphyrin monolayers and multilayers on Ag (111) and formation of iron-tetraphenylporphyrin," *The Journal of Physical Chemistry C*, vol. 112, no. 39, pp. 15458–15465, 2008.
- [45] K. Comanici, F. Buchner, K. Flechtner, T. Lukasczyk, J. M. Gottfried, H.-P. Steinrück, and H. Marbach, "Understanding the contrast mechanism in scanning tunneling microscopy (STM) images of an intermixed tetraphenylporphyrin layer on Ag (111)," *Langmuir*, vol. 24, no. 5, pp. 1897–1901, 2008.
- [46] F. Buchner, K.-G. Warnick, T. Wölflé, A. Görling, H.-P. Steinrück, W. Hieringer, and H. Marbach, "Chemical fingerprints of large organic molecules in scanning tunneling

- microscopy: Imaging adsorbate- substrate coupling of metalloporphyrins," *The Journal of Physical Chemistry C*, vol. 113, no. 37, pp. 16450–16457, 2009.
- [47] A. Dmitriev, H. Spillmann, N. Lin, J. V. Barth, and K. Kern, "Modular Assembly of Two-Dimensional Metal–Organic Coordination Networks at a Metal Surface," *Angewandte Chemie International Edition*, vol. 115, no. 23, pp. 2774–2777, 2003.
- [48] A. Gourdon, "On-surface covalent coupling in ultrahigh vacuum," *Angewandte Chemie International Edition*, vol. 47, no. 37, pp. 6950–6953, 2008.
- [49] G. Franc and A. Gourdon, "Covalent networks through on-surface chemistry in ultrahigh vacuum: State-of-the-art and recent developments," *Physical Chemistry Chemical Physics*, vol. 13, no. 32, pp. 14283–14292, 2011.
- [50] L. Grill, M. Dyer, L. Lafferentz, M. Persson, M. V. Peters, and S. Hecht, "Nano-architectures by covalent assembly of molecular building blocks," *Nature Nanotechnology*, vol. 2, no. 11, pp. 687–691, 2007.
- [51] M. Lackinger, "On-surface polymerization – A versatile synthetic route to two-dimensional polymers," *Polymer International*, vol. 64, no. 9, pp. 1073–1078, 2015.
- [52] L. Galvani, "De viribus electricitatis in motu musculari: Commentarius," *De Bononienst Scientiarum et Artium Instituto atque Academia Commentarii*, vol. 7, pp. 363–419, 1791.
- [53] A. Volta and J. Banks, "On the electricity excited by the mere contact of conducting substances of different kinds," *The Philosophical Magazine*, vol. 7, no. 28, pp. 289–311, 1800.
- [54] M. Faraday, "Experimental Researches in Electricity. Richard and John Edward Taylor," 1849.
- [55] W. Ostwald, *Elektrochemie, ihre Geschichte und Lehre*. Veit & comp., 1896.
- [56] K. Kabra, R. Chaudhary, and R. L. Sawhney, "Treatment of hazardous organic and inorganic compounds through aqueous-phase photocatalysis: A review," *Industrial & Engineering Chemistry Research*, vol. 43, no. 24, pp. 7683–7696, 2004.
- [57] N. Kobozev and V. Monblanova, "Über den mechanismus der elektrodifusion des wasserstoffes durch palladium," *Acta Physiochimica URSS*, vol. 1, pp. 611–650, 1934.
- [58] D. Pletcher, *A first course in electrode processes*. Royal Society of Chemistry, 2019.
- [59] C. H. Hamann and W. Vielstich, *Elektrochemie*. Wiley-Vch, 2005.
- [60] A. J. Bard and L. R. Faulkner, *Electrochemical Methods: Fundamentals and Applications*, vol. 2. Wiley New York, 2001.
- [61] A. Wieckowski and J. K. Nørskov, *Fuel cell science*. Wiley, 2010.

- [62] T. Erdey-Grúz and M. Volmer, "Zur Theorie der Wasserstoff Überspannung," *Zeitschrift für Physikalische Chemie*, vol. 150, no. 1, pp. 203–213, 1930.
- [63] J. Wei, M. Zhou, A. Long, Y. Xue, H. Liao, C. Wei, and Z. J. Xu, "Heterostructured electrocatalysts for hydrogen evolution reaction under alkaline conditions," *Nano-Micro Letters*, vol. 10, no. 4, p. 75, 2018.
- [64] J. Tafel, "Über die Polarisation bei kathodischer Wasserstoffentwicklung," *Zeitschrift für physikalische Chemie*, vol. 50, no. 1, pp. 641–712, 1905.
- [65] J. Heyrovsky, "A theory of overpotential," *Recueil des Travaux Chimiques des Pays-Bas*, vol. 46, no. 8, pp. 582–585, 1927.
- [66] X. Ge, A. Sumboja, D. Wu, T. An, B. Li, F. T. Goh, T. A. Hor, Y. Zong, and Z. Liu, "Oxygen reduction in alkaline media: From mechanisms to recent advances of catalysts," *ACS Catalysis*, vol. 5, no. 8, pp. 4643–4667, 2015.
- [67] B. Conway and J. O. Bockris, "Electrolytic hydrogen evolution kinetics and its relation to the electronic and adsorptive properties of the metal," *The Journal of Chemical Physics*, vol. 26, no. 3, pp. 532–541, 1957.
- [68] R. Parsons, "The kinetics of electrode reactions and the electrode material," *Surface Science*, vol. 2, pp. 418–435, 1964.
- [69] A. J. Medford, A. Vojvodic, J. S. Hummelshøj, J. Voss, F. Abild-Pedersen, F. Studt, T. Bligaard, A. Nilsson, and J. K. Nørskov, "From the Sabatier principle to a predictive theory of transition-metal heterogeneous catalysis," *Journal of Catalysis*, vol. 328, pp. 36–42, 2015.
- [70] C. G. Morales-Guio, L.-A. Stern, and X. Hu, "Nanostructured hydrotreating catalysts for electrochemical hydrogen evolution," *Chemical Society Reviews*, vol. 43, no. 18, pp. 6555–6569, 2014.
- [71] J. K. Nørskov, T. Bligaard, A. Logadottir, J. Kitchin, J. G. Chen, S. Pandalov, and U. Stimming, "Trends in the exchange current for hydrogen evolution," *Journal of The Electrochemical Society*, vol. 152, no. 3, pp. 23–26, 2005.
- [72] J. Zheng, J. Nash, B. Xu, and Y. Yan, "Perspective – Towards establishing apparent hydrogen binding energy as the descriptor for hydrogen oxidation/evolution reactions," *Journal of The Electrochemical Society*, vol. 165, no. 2, pp. 27–29, 2018.
- [73] W. Sheng, H. A. Gasteiger, and Y. Shao-Horn, "Hydrogen oxidation and evolution reaction kinetics on platinum: Acid vs alkaline electrolytes," *Journal of The Electrochemical Society*, vol. 157, no. 11, pp. 1529–1536, 2010.
- [74] J. Durst, A. Siebel, C. Simon, F. Hasche, J. Herranz, and H. Gasteiger, "New insights into the electrochemical hydrogen oxidation and evolution reaction mechanism," *Energy & Environmental Science*, vol. 7, no. 7, pp. 2255–2260, 2014.

- 
- [75] W. Sheng, Z. Zhuang, M. Gao, J. Zheng, J. G. Chen, and Y. Yan, "Correlating hydrogen oxidation and evolution activity on platinum at different pH with measured hydrogen binding energy," *Nature Communications*, vol. 6, no. 1, pp. 1–6, 2015.
- [76] J. Zheng, W. Sheng, Z. Zhuang, B. Xu, and Y. Yan, "Universal dependence of hydrogen oxidation and evolution reaction activity of platinum-group metals on pH and hydrogen binding energy," *Science Advances*, vol. 2, no. 3, pp. 1–8, 2016.
- [77] G. Binnig, H. Rohrer, C. Gerber, and E. Weibel, "Tunneling through a controllable vacuum gap," *Applied Physics Letters*, vol. 40, no. 2, pp. 178–180, 1982.
- [78] G. Binnig, H. Rohrer, C. Gerber, and E. Weibel, "Surface studies by scanning tunneling microscopy," *Physical Review Letters*, vol. 49, no. 1, p. 57, 1982.
- [79] C. J. Chen, *Introduction to scanning tunneling microscopy*, vol. 4. Oxford University Press on Demand, 1993.
- [80] G. Lippmann, "Principe de la conservation de l'électricité, ou second principe de la théorie des phénomènes électriques," *Journal de Physique Théorique et Appliquée*, vol. 10, no. 1, pp. 381–394, 1881.
- [81] H. Hertz, "Ueber einen Einfluss des ultravioletten Lichtes auf die electrische Entladung," *Annalen der Physik*, vol. 267, no. 8, pp. 983–1000, 1887.
- [82] A. Einstein, "Über einen die Erzeugung und Verwandlung des Lichtes betreffenden heuristischen Gesichtspunkt," *Annalen der Physik*, vol. 322, no. 6, pp. 132–148, 1905.
- [83] K. Stańczyk, R. Dziembaj, Z. Piwowarska, and S. Witkowski, "Transformation of nitrogen structures in carbonization of model compounds determined by XPS," *Carbon*, vol. 33, no. 10, pp. 1383–1392, 1995.
- [84] N. Hellgren, R. T. Haasch, S. Schmidt, L. Hultman, and I. Petrov, "Interpretation of X-ray photoelectron spectra of carbon-nitride thin films: New insights from in situ XPS," *Carbon*, vol. 108, pp. 242–252, 2016.
- [85] M. A. Herman and H. Sitter, *Molecular beam epitaxy: Fundamentals and current status*, vol. 7. Springer Science & Business Media, 2012.
- [86] H. Hoster and H. Gasteiger, "Ex-situ surface preparation and analysis: Transfer between UHV and electrochemical Cell," *Handbook of Fuel Cells*, 2010.
- [87] F. Reniers, "The development of a transfer mechanism between UHV and electrochemistry environments," *Journal of Physics D: Applied Physics*, vol. 35, no. 21, pp. 169–188, 2002.
- [88] F. Ullmann, "On a new formation of diphenylamine derivatives," *Berichte der Deutschen Chemischen Gesellschaft*, vol. 36, pp. 2382–2384, 1903.

## Bibliography

---

- [89] I. Goldberg, "Phenylation with presence of copper as catalyst," *Berichte der Deutschen Chemischen Gesellschaft*, vol. 39, pp. 1691–1692, 1906.
- [90] I. Goldberg, "Über Phenylierung von primären aromatischen Aminen," *Berichte der Deutschen Chemischen Gesellschaft*, vol. 40, no. 4, pp. 4541–4546, 1907.
- [91] F. Ullmann and E. Illgen, "Über Carbazole der Anthrachinon-Reihe," *Berichte der Deutschen Chemischen Gesellschaft*, vol. 47, no. 1, pp. 380–383, 1914.
- [92] F. Monnier and M. Taillefer, "Catalytic C–C, C–N, and C–O Ullmann-Type Coupling Reactions," *Angewandte Chemie International Edition*, vol. 48, no. 38, pp. 6954–6971, 2009.
- [93] Y. Okawa and M. Aono, "Nanoscale control of chain polymerization," *Nature*, vol. 409, no. 6821, pp. 683–684, 2001.
- [94] O. Endo, H. Ootsubo, N. Toda, M. Suhara, H. Ozaki, and Y. Mazaki, "Phase transition of a single sheet of sashlike polydiacetylene atomic sash on a solid surface," *Journal of the American Chemical Society*, vol. 126, no. 32, pp. 9894–9895, 2004.
- [95] S. Weigelt, C. Busse, C. Bombis, M. M. Knudsen, K. V. Gothelf, E. Lægsgaard, F. Besenbacher, and T. R. Linderoth, "Surface synthesis of 2D branched polymer nanostructures," *Angewandte Chemie International Edition*, vol. 47, no. 23, pp. 4406–4410, 2008.
- [96] M. Marschall, J. Reichert, A. Weber-Bargioni, K. Seufert, W. Auwärter, S. Klyatskaya, G. Zoppellaro, M. Ruben, and J. V. Barth, "Random two-dimensional string networks based on divergent coordination assembly," *Nature Chemistry*, vol. 2, no. 2, p. 131, 2010.
- [97] C. Steiner, J. Gebhardt, M. Ammon, Z. Yang, A. Heidenreich, N. Hammer, A. Görling, M. Kivala, and S. Maier, "Hierarchical on-surface synthesis and electronic structure of carbonyl-functionalized one- and two-dimensional covalent nanoarchitectures," *Nature Communications*, vol. 8, p. 14765, 2017.
- [98] S. Krotzky, C. Morchutt, V. S. Vyas, B. V. Lotsch, R. Gutzler, and K. Kern, "Thermodynamics of the segregation of a kinetically trapped two-dimensional amorphous metal–organic network," *The Journal of Physical Chemistry C*, vol. 120, no. 8, pp. 4403–4409, 2016.
- [99] D. P. Goronzy, M. Ebrahimi, F. Rosei, Arramel, Y. Fang, S. De Feyter, S. L. Tait, C. Wang, P. H. Beton, A. T. Wee, P. S. Weiss, and D. F. Perepichka, "Supramolecular assemblies on surfaces: nanopatterning, functionality, and reactivity," *ACS nano*, vol. 12, no. 8, pp. 7445–7481, 2018.
- [100] M. D. Ediger, J. de Pablo, and L. Yu, "Anisotropic vapor-deposited glasses: hybrid organic solids," *Accounts of Chemical Research*, vol. 52, no. 2, pp. 407–414, 2019.
- [101] P. Kot, J. Parnell, S. Habibian, C. Straßer, P. M. Ostrovsky, and C. R. Ast, "Band dispersion of graphene with structural defects," *Physical Review B*, vol. 101, no. 23, p. 235116, 2020.

- [102] C. Büchner, L. Liu, S. Stuckenholz, K. M. Burson, L. Lichtenstein, M. Heyde, H.-J. Gao, and H.-J. Freund, "Building block analysis of 2D amorphous networks reveals medium range correlation," *Journal of Non-Crystalline Solids*, vol. 435, pp. 40–47, 2016.
- [103] M. O. Blunt, J. C. Russell, N. R. Champness, and P. H. Beton, "Templating molecular adsorption using a covalent organic framework," *Chemical Communications*, vol. 46, no. 38, pp. 7157–7159, 2010.
- [104] R. Gutzler, H. Walch, G. Eder, S. Kloft, W. M. Heckl, and M. Lackinger, "Surface mediated synthesis of 2D covalent organic frameworks: 1,3,5-tris-(4-bromophenyl)-benzene on graphite (001), Cu (111), and Ag (110)," *Chemical Communications*, no. 29, pp. 4456–4458, 2009.
- [105] J. Eichhorn, D. Nieckarz, O. Ochs, D. Samanta, M. Schmittl, P. J. Szabelski, and M. Lackinger, "On-surface Ullmann coupling: The influence of kinetic reaction parameters on the morphology and quality of covalent networks," *ACS nano*, vol. 8, no. 8, pp. 7880–7889, 2014.
- [106] O. Ourdjini, R. Pawlak, M. Abel, S. Clair, L. Chen, N. Bergeon, M. Sassi, V. Oison, J.-M. Debierre, R. Coratger, and L. Porte, "Substrate-mediated ordering and defect analysis of a surface covalent organic framework," *Physical Review B*, vol. 84, no. 12, p. 125421, 2011.
- [107] A. Hannemann, J. Schön, M. Jansen, and P. Sibani, "Nonequilibrium dynamics in amorphous  $\text{Si}_3\text{B}_3\text{N}_7$ ," *The Journal of Physical Chemistry B*, vol. 109, no. 23, pp. 11770–11776, 2005.
- [108] S. Neelamraju, C. Oligschleger, and J. C. Schön, "The threshold algorithm: Description of the methodology and new developments," *The Journal of Chemical Physics*, vol. 147, no. 15, p. 152713, 2017.
- [109] J. Schön and M. Jansen, "Prediction, determination and validation of phase diagrams via the global study of energy landscapes," *International Journal of Materials Research*, vol. 100, no. 2, pp. 135–152, 2009.
- [110] L. C. E. Struik, "Physical aging in amorphous polymers and other materials," 1977.
- [111] R. Subbaraman, D. Tripkovic, D. Strmcnik, K.-C. Chang, M. Uchimura, A. P. Paulikas, V. Stamenkovic, and N. M. Markovic, "Enhancing hydrogen evolution activity in water splitting by tailoring  $\text{Li}^+$ - $\text{Ni}(\text{OH})_2$ -Pt interfaces," *Science*, vol. 334, no. 6060, pp. 1256–1260, 2011.
- [112] X. Yu, J. Zhao, L.-R. Zheng, Y. Tong, M. Zhang, G. Xu, C. Li, J. Ma, and G. Shi, "Hydrogen evolution reaction in alkaline media: alpha-or beta-nickel hydroxide on the surface of platinum?," *ACS Energy Letters*, vol. 3, no. 1, pp. 237–244, 2017.

## Bibliography

---

- [113] L. Stegbauer, K. Schwinghammer, and B. V. Lotsch, "A hydrazone-based covalent organic framework for photocatalytic hydrogen production," *Chemical Science*, vol. 5, no. 7, pp. 2789–2793, 2014.
- [114] T. Banerjee, K. Gottschling, G. Savasci, C. Ochsenfeld, and B. V. Lotsch, "H<sub>2</sub> evolution with covalent organic framework photocatalysts," *ACS Energy Letters*, vol. 3, no. 2, pp. 400–409, 2018.
- [115] J. W. Colson and W. R. Dichtel, "Rationally synthesized two-dimensional polymers," *Nature Chemistry*, vol. 5, no. 6, pp. 453–465, 2013.
- [116] Q. Shen, H.-Y. Gao, and H. Fuchs, "Frontiers of on-surface synthesis: From principles to applications," *Nano Today*, vol. 13, pp. 77–96, 2017.
- [117] C. C. McCrory, S. Jung, J. C. Peters, and T. F. Jaramillo, "Benchmarking heterogeneous electrocatalysts for the oxygen evolution reaction," *Journal of the American Chemical Society*, vol. 135, no. 45, pp. 16977–16987, 2013.
- [118] S. Trasatti and O. Petrii, "Real surface area measurements in electrochemistry," *Pure and Applied Chemistry*, vol. 63, no. 5, pp. 711–734, 1991.
- [119] J. D. Benck, Z. Chen, L. Y. Kuritzky, A. J. Forman, and T. F. Jaramillo, "Amorphous molybdenum sulfide catalysts for electrochemical hydrogen production: Insights into the origin of their catalytic activity," *ACS Catalysis*, vol. 2, no. 9, pp. 1916–1923, 2012.
- [120] R. Boggio, A. Carugati, and S. Trasatti, "Electrochemical surface properties of Co<sub>3</sub>O<sub>4</sub> electrodes," *Journal of Applied Electrochemistry*, vol. 17, no. 4, pp. 828–840, 1987.
- [121] A. Toyota, N. Nakashima, and T. Sagara, "UV-visible transmission – Absorption spectral study of Au nanoparticles on a modified ITO electrode at constant potentials and under potential modulation," *Journal of Electroanalytical Chemistry*, vol. 565, no. 2, pp. 335–342, 2004.
- [122] M. B. Cortie, A. Maaroo, and G. Smith, "Electrochemical capacitance of mesoporous gold," *Gold Bulletin*, vol. 38, no. 1, pp. 14–22, 2005.
- [123] N. Tao and S. Lindsay, "In situ scanning tunneling microscopy study of iodine and bromine adsorption on Au (111) under potential control," *The Journal of Physical Chemistry*, vol. 96, no. 13, pp. 5213–5217, 1992.
- [124] M. R. Miah and T. Ohsaka, "Electrochemical oxidation of hydrogen peroxide at a bromine adatom-modified gold electrode in alkaline media," *Electrochimica Acta*, vol. 54, no. 5, pp. 1570–1577, 2009.
- [125] R. Wang, K. Wang, Z. Wang, H. Song, H. Wang, and S. Ji, "Pig bones derived N-doped carbon with multi-level pores as electrocatalyst for oxygen reduction," *Journal of Power Sources*, vol. 297, pp. 295–301, 2015.



- [126] N. Graf, E. Yegen, T. Gross, A. Lippitz, W. Weigel, S. Krakert, A. Terfort, and W. E. Unger, "XPS and NEXAFS studies of aliphatic and aromatic amine species on functionalized surfaces," *Surface Science*, vol. 603, no. 18, pp. 2849–2860, 2009.
- [127] M. Chen, X. Feng, L. Zhang, H. Ju, Q. Xu, J. Zhu, J. M. Gottfried, K. Ibrahim, H. Qian, and J. Wang, "Direct synthesis of nickel (II) tetraphenylporphyrin and its interaction with a Au (111) surface: A comprehensive study," *The Journal of Physical Chemistry C*, vol. 114, no. 21, pp. 9908–9916, 2010.
- [128] J.-B. Lhoest, P. Bertrand, L. Weng, and J.-L. Dewez, "Combined time-of-flight secondary ion mass spectrometry and X-ray photoelectron spectroscopy study of the surface segregation of poly (methyl methacrylate) (PMMA) in bisphenol A polycarbonate/PMMA blends," *Macromolecules*, vol. 28, no. 13, pp. 4631–4637, 1995.
- [129] M. Nalbach, P. Raiteri, S. Klassen, S. Schäfer, J. D. Gale, R. Bechstein, and A. Kühnle, "Where Is the Most Hydrophobic Region? Benzopurpurine Self-Assembly at the Calcite–Water Interface," *The Journal of Physical Chemistry C*, vol. 121, no. 43, pp. 24144–24151, 2017.
- [130] T. Cheng, L. Wang, B. V. Merinov, and W. A. Goddard III, "Explanation of dramatic pH-dependence of hydrogen binding on noble metal electrode: Greatly weakened water adsorption at high pH," *Journal of the American Chemical Society*, vol. 140, no. 25, pp. 7787–7790, 2018.
- [131] P. Tereshchuk and J. L. Da Silva, "Ethanol and water adsorption on close-packed 3d, 4d, and 5d transition-metal surfaces: a density functional theory investigation with van der Waals correction," *The Journal of Physical Chemistry C*, vol. 116, no. 46, pp. 24695–24705, 2012.
- [132] S. Schnur and A. Groß, "Properties of metal–water interfaces studied from first principles," *New Journal of Physics*, vol. 11, no. 12, pp. 1–25, 2009.
- [133] J. R. McKone, B. F. Sadtler, C. A. Werlang, N. S. Lewis, and H. B. Gray, "Ni–Mo nanopowders for efficient electrochemical hydrogen evolution," *ACS Catalysis*, vol. 3, no. 2, pp. 166–169, 2013.
- [134] T. Nakagawa, C. A. Beasley, and R. W. Murray, "Efficient electro-oxidation of water near its reversible potential by a mesoporous IrO<sub>x</sub> nanoparticle film," *The Journal of Physical Chemistry C*, vol. 113, no. 30, pp. 12958–12961, 2009.
- [135] M. Yagi, E. Tomita, and T. Kuwabara, "Remarkably high activity of electrodeposited IrO<sub>2</sub> film for electrocatalytic water oxidation," *Journal of Electroanalytical Chemistry*, vol. 579, no. 1, pp. 83–88, 2005.
- [136] C. C. McCrory, S. Jung, I. M. Ferrer, S. M. Chatman, J. C. Peters, and T. F. Jaramillo, "Benchmarking hydrogen evolving reaction and oxygen evolving reaction electrocatalysts for

## Bibliography

---

- solar water splitting devices,” *Journal of the American Chemical Society*, vol. 137, no. 13, pp. 4347–4357, 2015.
- [137] C. Song and J. Zhang, *Electrocatalytic Oxygen Reduction Reaction*, pp. 89–134. London: Springer London, 2008.
- [138] R. Decker, U. Schlickum, F. Klappenberger, G. Zoppellaro, S. Klyatskaya, M. Ruben, J. Barth, and H. Brune, “Using metal-organic templates to steer the growth of Fe and Co nanoclusters,” *Applied Physics Letters*, vol. 93, no. 24, p. 243102, 2008.
- [139] S. Lin, C. S. Diercks, Y.-B. Zhang, N. Kornienko, E. M. Nichols, Y. Zhao, A. R. Paris, D. Kim, P. Yang, O. M. Yaghi, and C. J. Chang, “Covalent organic frameworks comprising cobalt porphyrins for catalytic CO<sub>2</sub> reduction in water,” *Science*, vol. 349, no. 6253, pp. 1208–1213, 2015.
- [140] L. K. Blusch, O. Mitevski, V. Martin-Diaconescu, K. Pröpper, S. DeBeer, S. Dechert, and F. Meyer, “Selective synthesis and redox sequence of a heterobimetallic nickel/copper complex of the noninnocent siamese-twin porphyrin,” *Inorganic Chemistry*, vol. 53, no. 15, pp. 7876–7885, 2014.
- [141] A. Fuerte, A. Corma, M. Iglesias, E. Morales, and F. Sánchez, “A cooperative effect between support and the heterogenised metalloporphyrins on electrocatalytic oxygen reduction,” *Catalysis Letters*, vol. 101, no. 1-2, pp. 99–103, 2005.
- [142] D. Hötger, M. Etzkorn, C. Morchutt, B. Wurster, J. Dreiser, S. Stepanow, D. Grumelli, R. Gutzler, and K. Kern, “Stability of metallo-porphyrin networks under oxygen reduction and evolution conditions in alkaline media,” *Physical Chemistry Chemical Physics*, vol. 21, no. 5, pp. 2587–2594, 2019.
- [143] Z. Zhang, S. Yang, M. Dou, H. Liu, L. Gu, and F. Wang, “Systematic study of transition-metal (Fe, Co, Ni, Cu) phthalocyanines as electrocatalysts for oxygen reduction and their evaluation by DFT,” *RSC Advances*, vol. 6, no. 71, pp. 67049–67056, 2016.
- [144] S. Petitto and M. Langell, “Surface composition and structure of Co<sub>3</sub>O<sub>4</sub> (110) and the effect of impurity segregation,” *Journal of Vacuum Science & Technology A: Vacuum, Surfaces, and Films*, vol. 22, no. 4, pp. 1690–1696, 2004.
- [145] F. Parmigiani and L. Sangaletti, “Fine structures in the X-ray photoemission spectra of MnO, FeO, CoO, and NiO single crystals,” *Journal of Electron Spectroscopy and Related Phenomena*, vol. 98, pp. 287–302, 1999.
- [146] Y. Bai, M. Sekita, M. Schmid, T. Bischof, H.-P. Steinrück, and J. M. Gottfried, “Interfacial coordination interactions studied on cobalt octaethylporphyrin and cobalt tetraphenylporphyrin monolayers on Au (111),” *Physical Chemistry Chemical Physics*, vol. 12, no. 17, pp. 4336–4344, 2010.

- [147] F. Petraki, H. Peisert, I. Biswas, and T. Chassé, "Electronic structure of Co-phthalocyanine on gold investigated by photoexcited electron spectroscopies: Indication of Co ion-metal interaction," *The Journal of Physical Chemistry C*, vol. 114, no. 41, pp. 17638–17643, 2010.
- [148] J. Xiao and P. A. Dowben, "Changes in the adsorbate dipole layer with changing d-filling of the metal (II)(Co, Ni, Cu) phthalocyanines on Au (111)," *Journal of Physics: Condensed Matter*, vol. 21, no. 5, pp. 1–5, 2008.
- [149] A. Zhao, Q. Li, L. Chen, H. Xiang, W. Wang, S. Pan, B. Wang, X. Xiao, J. Yang, J. Hou, and Q. Zhu, "Controlling the Kondo effect of an adsorbed magnetic ion through its chemical bonding," *Science*, vol. 309, no. 5740, pp. 1542–1544, 2005.
- [150] A. Zhao, Z. Hu, B. Wang, X. Xiao, J. Yang, and J. Hou, "Kondo effect in single cobalt phthalocyanine molecules adsorbed on Au (111) monoatomic steps," *The Journal of Chemical Physics*, vol. 128, no. 23, p. 234705, 2008.
- [151] N. D. Yates, M. R. Dowsett, P. Bentley, J. A. Dickenson-Fogg, A. Pratt, C. F. Blanford, M. A. Fascione, and A. Parkin, "Aldehyde-mediated protein-to-surface tethering via controlled diazonium electrode functionalization using protected hydroxylamines," *Langmuir*, vol. 36, no. 20, pp. 5654–5664, 2019.
- [152] M. Gabaji, J. Médard, A. Hemmerle, J. Pinson, and J.-P. Michel, "From Langmuir–Blodgett to grafted films," *Langmuir*, vol. 36, no. 10, pp. 2534–2542, 2020.
- [153] D. Belanger and J. Pinson, "Electrografting: A powerful method for surface modification," *Chemical Society Reviews*, vol. 40, no. 7, pp. 3995–4048, 2011.
- [154] A. Mesnage, X. Lefèvre, P. Jégou, G. Deniau, and S. Palacin, "Spontaneous grafting of diazonium salts: Chemical mechanism on metallic surfaces," *Langmuir*, vol. 28, no. 32, pp. 11767–11778, 2012.
- [155] C. Jiang, S. M. Silva, S. Fan, Y. Wu, M. T. Alam, G. Liu, and J. J. Gooding, "Aryldiazonium salt derived mixed organic layers: From surface chemistry to their applications," *Journal of Electroanalytical Chemistry*, vol. 785, pp. 265–278, 2017.
- [156] A. J. Gross, C. Bucher, L. Coche-Guerente, P. Labbé, A. J. Downard, and J.-C. Moutet, "Nickel (II) tetraphenylporphyrin modified surfaces via electrografting of an aryldiazonium salt," *Electrochemistry Communications*, vol. 13, no. 11, pp. 1236–1239, 2011.
- [157] T. Menanteau, E. Levillain, A. Downard, and T. Breton, "Evidence of monolayer formation via diazonium grafting with a radical scavenger: Electrochemical, AFM and XPS monitoring," *Physical Chemistry Chemical Physics*, vol. 17, no. 19, pp. 13137–13142, 2015.
- [158] S. Sun, N. Jiang, and D. Xia, "Density functional theory study of the oxygen reduction reaction on metalloporphyrins and metallophthalocyanines," *The Journal of Physical Chemistry C*, vol. 115, no. 19, pp. 9511–9517, 2011.

## Bibliography

---

- [159] M. Gattrell, N. Gupta, and A. Co, "Electrochemical reduction of CO<sub>2</sub> to hydrocarbons to store renewable electrical energy and upgrade biogas," *Energy Conversion and Management*, vol. 48, no. 4, pp. 1255–1265, 2007.
- [160] K. P. Kuhl, E. R. Cave, D. N. Abram, and T. F. Jaramillo, "New insights into the electrochemical reduction of carbon dioxide on metallic copper surfaces," *Energy & Environmental Science*, vol. 5, no. 5, pp. 7050–7059, 2012.
- [161] M. Gattrell, N. Gupta, and A. Co, "A review of the aqueous electrochemical reduction of CO<sub>2</sub> to hydrocarbons at copper," *Journal of Electroanalytical Chemistry*, vol. 594, no. 1, pp. 1–19, 2006.
- [162] L. Zhang, Z.-J. Zhao, and J. Gong, "Nanostructured materials for heterogeneous electrocatalytic CO<sub>2</sub> reduction and their related reaction mechanisms," *Angewandte Chemie International Edition*, vol. 56, no. 38, pp. 11326–11353, 2017.
- [163] D. W. DeWulf, T. Jin, and A. J. Bard, "Electrochemical and surface studies of carbon dioxide reduction to methane and ethylene at copper electrodes in aqueous solutions," *Journal of the Electrochemical Society*, vol. 136, no. 6, p. 1686, 1989.
- [164] D. Behar, T. Dhanasekaran, P. Neta, C. Hosten, D. Ejeh, P. Hambright, and E. Fujita, "Cobalt porphyrin catalyzed reduction of CO<sub>2</sub>. Radiation chemical, photochemical, and electrochemical studies," *The Journal of Physical Chemistry A*, vol. 102, no. 17, pp. 2870–2877, 1998.
- [165] T. Hatsukade, K. P. Kuhl, E. R. Cave, D. N. Abram, and T. F. Jaramillo, "Insights into the electrocatalytic reduction of CO<sub>2</sub> on metallic silver surfaces," *Physical Chemistry Chemical Physics*, vol. 16, no. 27, pp. 13814–13819, 2014.

# Curriculum Vitae

## Name

Name	Patrick Eduard Alexa
Address	Rötestrasse 56, 70197 Stuttgart
Date of Birth	January 02, 1989
Place of Birth	Munich, Germany
Nationality	German
eMail	p.alex@fkf.mpg.de

## Professional Experience

2016 - 2020	Doctoral Studies (Ph.D.): École Polytechnique Fédérale de Lausanne, Switzerland Research Assistant: Max Planck Institute for Solid State Research, Stuttgart Germany
2010 - 2014	Graduate Research Assistant: Ludwig Maximilians University, Munich, Germany

## University Education

2012 - 2015	Master of Science: Geomaterials and Geochemistry at Ludwig Maximilians University, Munich, Germany
2008 - 2009	Bachelor of Science: Technical University of Munich, Germany

## School Education

1999 - 2008	Gymnasium Kirchheim
-------------	---------------------